MEASUREMENT AND MODELING OF FLUID PRESSURES IN CHEMICAL MECHANICAL POLISHING

A Dissertation
Presented to
The Academic Faculty

By

Sum Huan Ng

In Partial Fulfillment
of the Requirements for the Degree
Doctor of Philosophy in the
School of Mechanical Engineering

Georgia Institute of Technology
May 2005

MEASUREMENT AND MODELING OF FLUID PRESSURES IN CHEMICAL MECHANICAL POLISHING

Approved by:

Dr. Steven Danyluk, Chair
School of Mechanical Engineering
Georgia Institute of Technology

Dr. Michael Sacks
School of Material Science & Engineering
Georgia Institute of Technology

Dr. Richard Salant
School of Mechanical Engineering
Georgia Institute of Technology

Dr. Dennis Hess
School of Biomolecular & Chemical Engineering
Georgia Institute of Technology

Dr. Jeffrey Streator
School of Mechanical Engineering
Georgia Institute of Technology

Dr. Leonard Borucki
Intelligent Planar

Date Approved: 23rd February 2005

God does not care about our mathematical difficulties.
He integrates empirically.

Albert Einstein, (1879-1955)
in L. Infeld Quest, 1942.

ACKNOWLEDGEMENTS

The list is long and it seems impossible to include everyone; but I will try my best. First, I would like to thank my advisor, Professor Steven Danyluk, for his patience, guidance and support. Through him, I've learned the importance of understanding things at the fundamental level and to have an open mind. I would like to thank him for his patience in improving my presentation and written skills, and for giving me the chances to hone my delivery in the many conferences I had attended.

I would like to thank Professor Richard Salant, Professor Jeffrey Streator, Professor Michael Sacks, Professor Dennis Hess and Dr Leonard Borucki for agreeing to be on my thesis committee, and for the suggestions they had given me. I would like to thank Dr C. Fred Higgs III for our numerous discussions on CMP and Dr Leonard Borucki for showing me the power of physics-based modeling. Their expertise has proven invaluable to the progress of this research.

Many thanks go to all my labmates throughout the years for the assistance they had given me, especially members of the CMP subgroup: Inho Yoon, Robert Hight, Dr Chunhong Zhou, Lip Kong Yap and Andres Osorno. I appreciate the help by Nancy Moody, Gail Payne, Donna Rogers and Lisa Teasly in processing my purchases, claims, itineraries and other administrative tasks swiftly. I would like to thank Steven Sheffield and John Graham for teaching me how to operate their equipments and for their assistance in the machining of parts. My gratitude goes to other people at Georgia Tech who had in one way or another helped me, but are not listed here. I would like to thank the numerous friends I had made here, many of whom had come and go, for making my life here more enriching.

I would like to show my appreciation to the Agency for Science, Technology and Research (A*STAR) and the Singapore Institute of Manufacturing Technology (SIMTech) for giving me the opportunity and the financial support to pursue a doctoral degree. For funding the CMP research, I would like to acknowledge the support from Motorola Inc., CPC Corporation, EKC Technology, Rohm and Haas, and the NSF Center for Surface Engineering and Tribology (CSET) here at Georgia Tech. CPC Corporation and EKC Technology had also provided us with a wide range of slurries we can work with, and Rohm and Haas had always responded to our unending requests for polishing pads and carrier films.

All these would not have been possible without the approval, love and support from my family in Singapore during my extended stay here in the United States. I would like to thank them, especially my parents, for their concern all the time. Last but not least, I would like to thank my wife, Brenda, for her love, patience, care and concern. She has been more than the best wife I could hope for. I would also like to thank her for bringing in our first born son, Dylan, who has given us much joy and happiness, and for being an excellent mother to him.

TABLE OF CONTENTS

LIST OF TABLES

LIST OF FIGURES

NOMENCLATURE

ν	Poisson's ratio of the half-space
A	cross-sectional area of abrasive-wafer interference
a	half length or radius of a rigid flat
A_n	wafer-pad nominal area of contact
A_r	wafer-pad real area of contact
a_{aw}	abrasive-wafer contact radius
a_{wp}	wafer-pad contact radius
c_m	mass fraction of abrasive in slurry
c_v	volume fraction of abrasive in slurry
D	abrasive diameter
d	separation distance between disk/wafer and pad
D_m	mean abrasive diameter
d_z	vertical displacement of the center of the bottom of the disk with respect to the static position
d_{pivot}	height of the pivot point above the bottom surface of the disk
E^*	contact modulus
E_p	elastic modulus of pad
E_w	elastic modulus of disk/wafer
E_{bp}	bulk pad modulus
E'_{wp}	wafer-pad effective modulus of elasticity
f	friction coefficient between rigid flat and half-space

F_c summation of solid contact pressure

F_f summation of fluid pressure

F_L applied load

F_z force in z direction

f_δ probability density function of combined roughness

$F_{c,ij}$ solid contact pressure at node (i,j)

f_D probability density function of abrasive diameter

$F_{f,ij}$ fluid pressure at node (i,j)

f_r probability density function of the location of an abrasive

$F_{s,ij}$ solid shear force at node (i,j)

$F_{sx,ij}$ x component of solid shear force at node (i,j)

$F_{sy,ij}$ y component of solid shear force at node (i,j)

g_r acceleration in the radial direction

g_x acceleration in the x direction

g_y acceleration in the y direction

g_z acceleration in the z direction

g_θ acceleration in the tangential direction

h nominal film thickness

H_c dimensionless central film thickness

h_c central film thickness

H_w hardness of wafer

$h_{T,avg}$ average gap

h_T local film thickness

k_a	dimensionless wear coefficient
k_e	ellipticity parameter
k_p	Preston constant
k_{mr}	probability of material removal
l	length
m	mass of the disk
m_a	mass of abrasive in slurry
m_s	mass of liquid in slurry
M_x	moment about x
$M_{x,c}$	moment about x due to solid contact pressure
$M_{x,f}$	moment about x due to fluid pressure
$M_{y,c}$	moment about y due to solid contact pressure
$M_{y,f}$	moment about y due to fluid pressure
n	number of abrasives
N_a	number of abrading particles
n_a	number of abrading particles per unit area
n_w	normal vector of the tilted disk
P	applied load per unit length
p	pressure
p_c	contact stress
r	radial coordinate
R_s	pad asperity tip radius
s	root-mean-square roughness of the pad; standard deviation of combined surface roughness

s_1	standard deviation of surface 1 height
s_2	standard deviation of surface 2 height
S_{p0}	undeformed thickness of the bulk pad
S_{pn}	deformed thickness of the bulk pad
t	time
t_{mr}	thickness removed per unit time
U	dimensionless speed parameter
u	velocity in the x direction
V	velocity
v	velocity in the y direction
v_a	average volume of an abrasive
v_r	velocity in the radial direction
v_z	velocity in the z direction
v_θ	velocity in the tangential direction
V_{r1}	variance ratio for shear flow factor
v_{wp}	wafer-pad relative velocity
W	dimensionless load parameter
w	velocity in the z direction
W_1	force acting on the abrasive due to the wafer
W_2	force acting on the abrasive due to the pad
w_z	normal load component
x	x-coordinate
x_c	offset distance between the centers of wafer and pad

y	y-coordinate
z	pad asperity height; z-coordinate
z_{off}	vertical distance between the center of the bottom face of the disk and the surface of the platen
${E_{ap}}^*$	abrasive-pad contact modulus
${E_{wp}}^*$	wafer-pad contact modulus
δ_{ap}	abrasive-pad interference
δ_{aw}	abrasive-wafer interference
δ_{wp}	wafer-pad interference
ω_p	rotational speed of pad (in radians per second)
ω_w	rotational speed of wafer (in radians per second)
ρ_a	density of abrasive
ρ_s	density of liquid in slurry
σ_D	standard deviation of abrasive diameter
δ	combined roughness
δ_1	random roughness amplitude of surface 1
δ_2	random roughness amplitude of surface 2
η	pad asperity density
μ	fluid viscosity
ν_p	Poisson's ratio of pad
ν_w	Poisson's ratio of disk/wafer
ω	rotational speed (in radians per second)
ϕ	tilt angle
ϕ_r	pressure flow factor in the radial direction

ϕ_s shear flow factor

ϕ_θ pressure flow factor in the tangential direction

ϕ_z pad asperity height distribution function

ρ fluid density

θ tangential coordinate

θ_a azimuth angle

SUMMARY

A theory of the sub-ambient fluid pressure phenomenon observed during the wet sliding of a disk on a polymeric pad is presented. Two-dimensional fluid pressure mapping using membrane pressure sensors reveals a large, asymmetrical sub-ambient pressure region occupying about 70 percent of the disk-pad contact area. At the same time, a small positive pressure region exists near the trailing edge of the disk. This phenomenon is believed to be present during chemical mechanical polishing (CMP) and can contribute to the contact pressure, affecting the material removal rate and removal uniformity. Depending on the load and pad speed, the real contact pressure can be more than 2 times the nominal contact pressure due to the applied load. Tilt measurements of the disk carried out by a capacitive sensing technique indicate that the disk is tilted towards the leading edge and pad center when the pad is rotating. In addition, wafer bow is found to be less than 2 μm and wafer tilt with respect to the wafer carrier is 5 to 7 μm in the CMP configuration. A two-dimensional mixed-lubrication model based on the Reynolds equation is developed and solved using a finite differencing scheme. The pad is modeled as two layers: a top asperity layer described by the Greenwood and Williamson equation, and the bulk pad as linearly elastic. The orientation of the disk is determined by balancing the fluid and solid forces acting on it and solving using a modified Newton's method. It is found that the tilt of the disk and the pad topography play important roles in the distribution of fluid pressure through affecting the film thickness distribution. For a pad with severe topography, minimum and maximum fluid pressures of -90 kPa and +51 kPa respectively are detected. The model is able to recreate the

experimental pressure maps. A material removal rate model based on mechanical abrasion and statistics has also been developed. The model assumes that only abrasives trapped between the tips of the pad asperities and the wafer are responsible for material removal. Abrasives that are too large to get between the pad asperity tips and wafer are filtered out. Taking into account the relative velocity distribution and contact pressure distribution across the wafer, the model is able to create the material removal rate distribution. Comparisons of model predictions and silicon oxide polishing results show agreement.

CHAPTER 1

INTRODUCTION

Chemical mechanical polishing (CMP) refers to an integrated-circuit (IC) fabrication process first developed by IBM in the 1980s. This process is used to produce flat (planar) surfaces on silicon substrates or partially-processed wafers during the manufacturing of IC's. Polishing is related to the surface roughness while planarization is related to the flatness of the material surface. It is the planarization capability of the process that has contributed to its success and its being an indispensable step in IC manufacturing. Polishing is well known in the field of glass polishing and metallographic finishing. A lot of knowledge and experience are gained from studies of glass polishing since one of the first materials to be CMP is silicon oxide. Glass polishing is capable of creating well-finished and even optically flat surfaces. The silicon oxide used in the IC industry is a form of silicate glass making silicon oxide CMP a specialized form of glass polishing.

1.1 The CMP Process

The polishing process is closely related to lapping: both rely on free abrasives under similar geometric conditions. In polishing, a soft pad is used, while in lapping a metal or glass is used. Figure 1.1 shows the classifications of both processes based on the tool and abrasives. Fundamentally, in CMP or in glass polishing, the material surface to be worked on is pressed against a soft material (the polishing pad) such as felt, leather or a porous polymer; and there is relative motion between

the two surfaces. This combination of contact pressure and relative motion alone does not cause material removal since the polishing pad is usually much softer than the workpiece material. So, a slurry composed of fine abrasive particles suspended in chemicals is introduced into the interface between the workpiece and the pad. This is achieved by spraying or depositing slurry on the pad before polishing, or a continuous supply of slurry is introduced to the surface of the pad "upstream" of the workpiece. Material removal is a synergistic combination of the chemical activity with the workpiece material and the mechanical action of the abrasive particles (see Figure 1.2) but the exact nature of this process has not been completely understood.

Figure 1.3 shows a rotational format configuration for a typical CMP process. The wafer is held by a wafer carrier and pressed against the rotating pad. The wafer carrier also rotates, normally in the same direction as the pad. In some machines, a sweeping motion is implemented which causes the wafer carrier to oscillate horizontally between the inner and outer regions of the much larger polishing pad. Key process parameters are the normal load applied to the wafer carrier, wafer carrier speed and pad speed. Other input variables include: abrasive type, chemicals, pad type, etc, which will be discussed in the next chapter. In fact, there are over 50 input and output variables in the CMP process. Some of the output variables are material removal rate, surface roughness, surface planarity, defectivity (can be further broken down to a number of defect classifications), dishing, erosion, and so on.

1.2 Applications of CMP

Chemical mechanical polishing was developed initially for interlevel-dielectric (ILD) and tungsten plug processing [3]. Deposited silicon oxide is used as the ILD

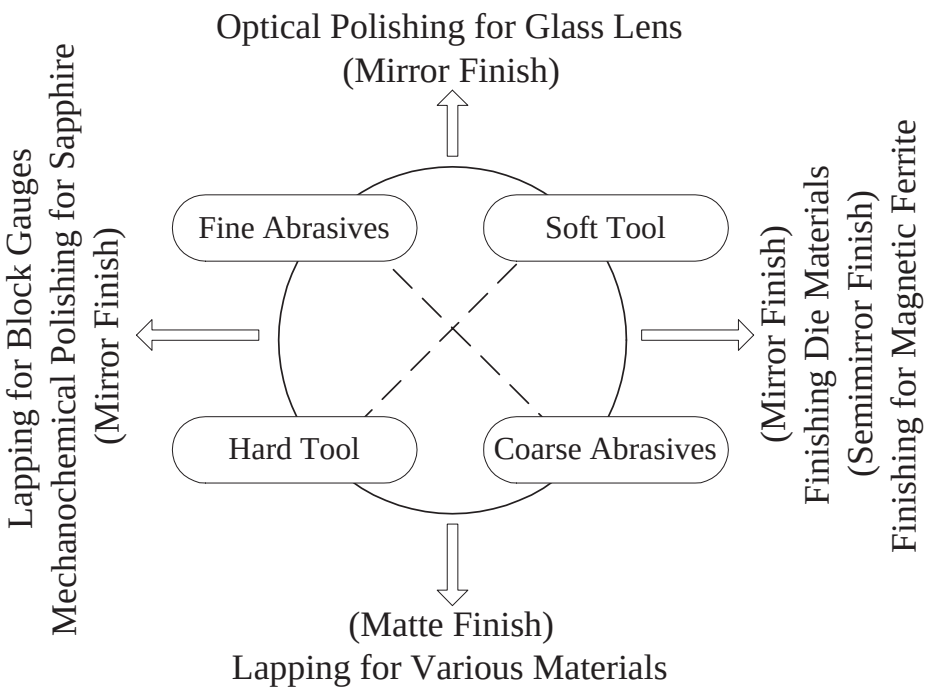

Figure 1.1: Classification of lapping and polishing on the basis of combinations of tools and abrasives [1]

and chemical vapor deposited (CVD) tungsten filled vias are used for interconnection between layers of sputtered aluminum which is the planar interconnect metal. In this process, CMP is used to remove the overburden of tungsten that is deposited, at the same time planarizing the silicon oxide. Figure 1.4 shows the concepts of silicon oxide polishing and tungsten plug polishing. Since these applications, CMP has been expanded for use on other materials such as copper, aluminum, titanium, silicon, tantalum, titanium nitride, and so on.

One of the most important applications of CMP currently is the creation of damascene structures. The damascene process is used in making copper interconnects due to the difficulty in etching copper. Aluminum has been used as the metallization scheme for a long time and reactive ion etching (RIE) has been used to create the metal patterns. However, as dimensions are scaled down in IC, the interconnect

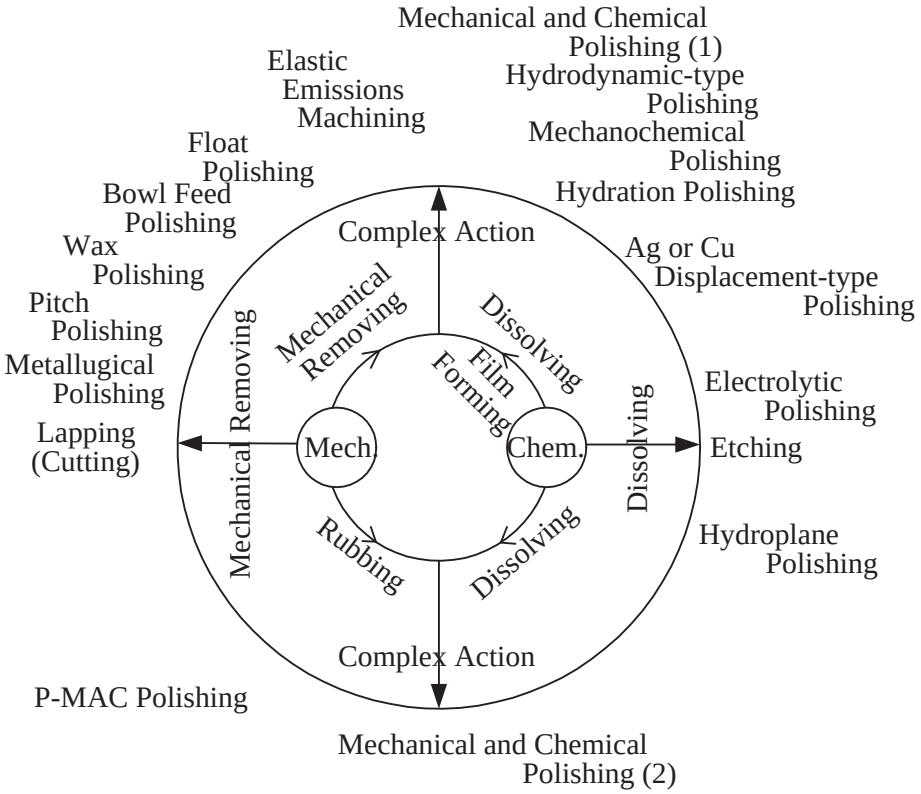

Figure 1.2: Classification of polishing methods based on stock removing mechanism [2]

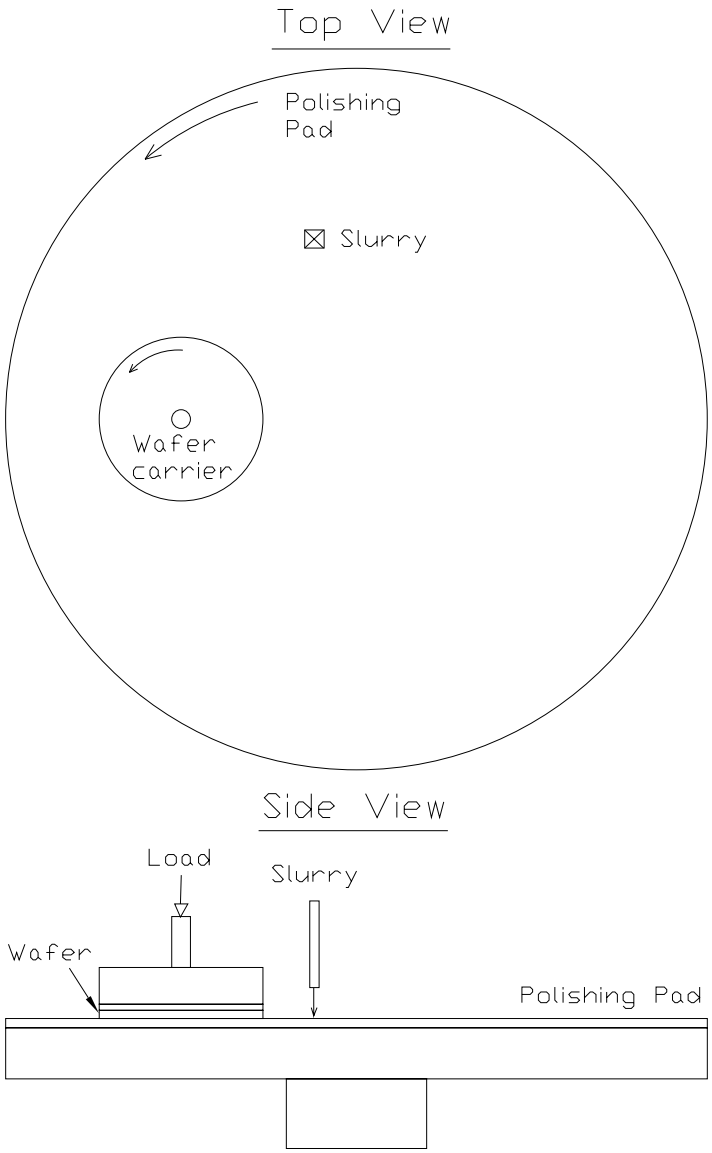

Figure 1.3: Typical CMP layout

delay associated with the performance of the IC increases. In order to decrease the interconnect delay, one of the ways is to reduce the resistivity of the metal. As a result, copper is introduced as the next interconnect metal due to its lower resistivity and good electromigration resistance. However, current etching techniques could not be used to create patterns in copper. In the damascene process to be used on copper, copper is deposited either by sputtering or electroplating or both, onto a layer of patterned dielectric like silicon oxide. The copper material is supposed to fill up the vias or trenches on the etched dielectric. Chemical mechanical polishing is then used to remove the excess overburden of copper creating inlaid copper structures similar to that of tungsten plug polishing shown in Figure 1.4(b). This procedure is repeated layer after layer of metallization as seen in Figure 1.5. With the copper dual damascene process, the alumnium lines and tungsten vias can be replaced by copper in one process step. Although aluminum is still in use today, copper is fast replacing it as the preferred interconnect.

Borst et al. [4] pointed out 4 major technology advances of the 1990s decade with significant impact on back-end-of-the-line (BEOL) manufacturing processes and IC performance capabilities. Back-end-of-the-line operations are performed on the semiconductor wafer in the course of device manufacturing following first metallization. Front-end-of-the-line (FEOL) operations are performed on the semiconductor wafer in the course of device manufacturing up to first metallization. These 4 technology advances were:

1) CMP which enables 6-8 levels of on-chip metallization

2) copper metallization for lines and vias to replace aluminum lines and tungsten vias

3) dual damascene to replace RIE and dielectric gap fill

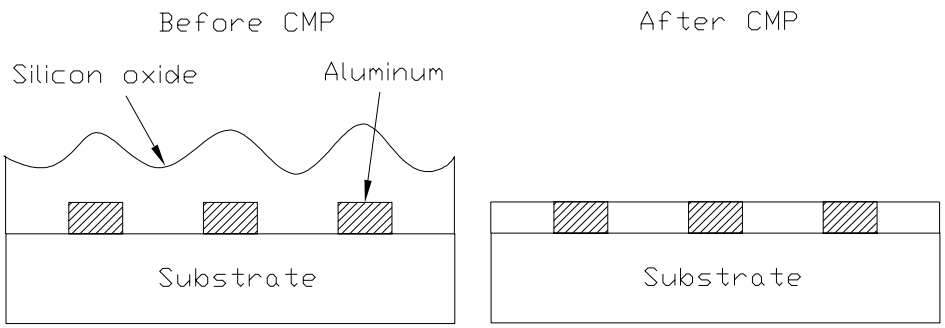

(a) Silicon oxide

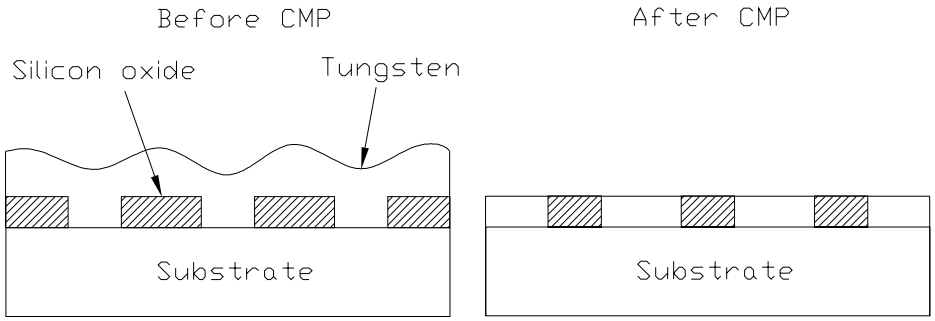

(b) Tungsten

Figure 1.4: Silicon oxide and tungsten plug CMP

4) low dielectric constant (low-k) ILDs to replace SiO_2

The current state-of-the-art in IC manufacturing is 90 nm technology (with 65 nm technology expected to be put into production in 2005) on 300 mm wafers. Its latest static random access memory (SRAM) process features 7 layers of copper interconnects. Traditionally developed for removing metal and ceramic materials, CMP will face new challenges as the need for reducing interconnect delay drives the usage of polymers and porous materials for low-k and ultra low-k ILDs.

1.3 Problem Definition

The tribological aspects of CMP will be presented in this thesis. This involved looking at the fluid mechanics and contact mechanics of the process. The focus will

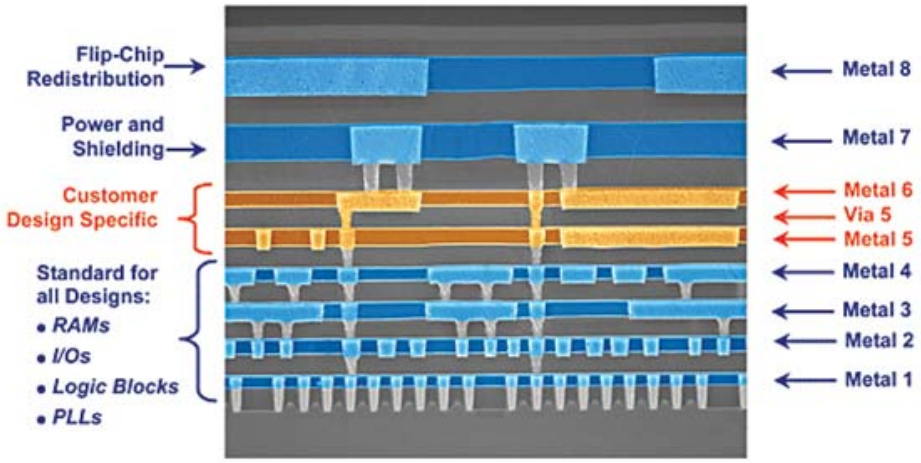

Figure 1.5: Cross-sectional view of an IC chip showing multiple metal layers

be on extending the modeling of the fluid pressures as observed by Levert and Shan. The existing model predicting the one-dimensional fluid pressure profile is reviewed here.

1.3.1 Prior work.

The contact stress was determined by considering the line loading of an elastic half-space (i.e., the pad) by a flat, rigid, sliding punch (i.e., the disk or wafer) according to Johnson's equation [5]

$$\sigma(x) = \frac{P cos\pi\gamma}{\pi(a^2 - x^2)^{1/2}}(\frac{a+x}{a-x})^{\gamma} \tag{1.1}$$

where γ can be computed from

$$cos\pi\gamma = -\frac{2(1-\nu)}{f(1-2\nu)} \tag{1.2}$$

The symbol P represents the applied normal load per unit length and a is the half length or radius of a rigid flat. The friction coefficient between the rigid flat

and the half-space is f and ν is the Poisson's ratio of the half-space.

This contact stress distribution can then be used with the Greenwood and Williamson equation [6] to determine the separation between the rigid flat and the mean plane of pad asperities. The Greenwood and Williamson equation is given by

$$p_c(x) = \frac{4E_p}{3(1-{\nu_p}^2)}\eta {R_s}^{1/2} \int_d^\infty (z-d)^{3/2}\phi_z(z)\,dz \tag{1.3}$$

where p_c is the contact stress, E_p is the elastic modulus of the pad, ν_p is the Poisson's ratio of the pad, η is the pad asperity density, R_s is the pad asperity tip radius, z is the pad asperity height, d is the separation distance between the disk and the pad, and ϕ_z is the pad asperity height distribution function.

By equating Eqn. 1.1 and Eqn. 1.3, the distance between mean plane of asperities and the target surface, d, can be solved. This distance would then be taken as the mean fluid film thickness, h. The one-dimensional Reynold's equation (with long bearing assumption) is used to calculate the interfacial fluid pressure based on the mean fluid film thickness, h, and other factors

$$\frac{d}{dx}(h^3\frac{dp}{dx}) = 6\mu V\frac{dh}{dx} \tag{1.4}$$

where p is the fluid pressure, μ is the fluid viscosity, and V is the velocity.

The resulting fluid pressure is asymmetrical and mostly sub-ambient; and predicts the experimental trend well. However, result from FEM analysis shows that the assumption of the pad as an elastic half-space is inadequate since the pad is in fact, thin. The size of the wafer/pad contact region is more than a hundred times the thickness of the pad. The contact pressure distribution at the interface between a rigid punch and a thin elastic pad is essentially uniform except near the edges of

the punch where there is a localized peak stress due to the sudden change in geometry. But this increase in stress exists only a couple of millimeters at most, from the wafer edge. A comparison between the FEM and Johnson's solution is shown in Figure 1.6. Johnson's solution is the pressure that would arise on the face of a flat-ended, frictionless cylindrical punch pressed squarely against an elastic half-space. The contact pressure is theoretically infinite at the edge of the punch. The FEM solution, on the other hand, is flat in profile until the very edge where a sharp jump in contact pressure occurs. Details of the FEM analysis will be presented in Chapter 3. With a uniform contact pressure distribution, there would not be any change in film thickness on the wafer scale that could cause hydrodynamic pressures. Hence, there exists a need to find out the reason for the sub-ambient pressure phenomenon.

The experiments and models are all based on a stainless steel disk but in the most basic CMP configuration there is a wafer, a carrier film (or sometimes called backing film) and a retaining ring. The carrier film is a thin (≈ 0.7 mm) piece of porous polymer attached to the bottom of the disk by pressure-sensitive adhesive (PSA). It serves to cushion the wafer and prevents localized peak contact stresses. The retaining ring is usually a piece of ceramic consumable that surrounds the periphery of the wafer to prevent the wafer from sliding out from under the disk during polishing. The shape and orientation of the wafer is important as it will affect the film thickness distribution [7, 8]. Hence, an understanding in this aspect is essential to relate the sub-ambient pressure phenomenon to the actual CMP process.

Finally, a material removal rate model will help relate the fluid and contact pressure results to material removal.

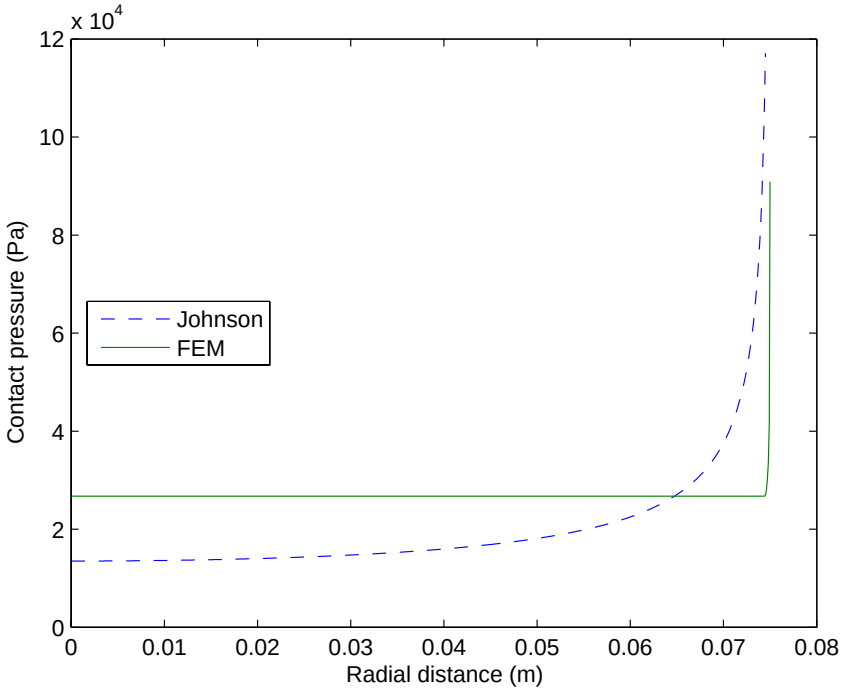

Figure 1.6: Johnson and FEM contact pressure profiles

1.4 Approach and Methodology

The objective of this research is to develop a two-dimensional mathematical model for the fluid pressures in CMP by including contact mechanics, fluid mechanics, kinematics and orientation of the wafer carrier, and to verify it by experiments. The research plan is shown in Figure 1.7. Improvements to the present model include moving from a one-dimensional to a two-dimensional analysis, taking into account the orientation of the disk, considering pad topography and incorporating an interative loop to achieve force and moment balance of the disk. To better understand the sub-ambient pressure phenomenon, it will be necessary to map out the two-dimensional pressure under the disk. Since the disk is mounted on a gimbal joint, it is expected that the orientation of the disk with respect to the pad can be affected by the normal and shear forces acting on it by the pad. A slight tilt

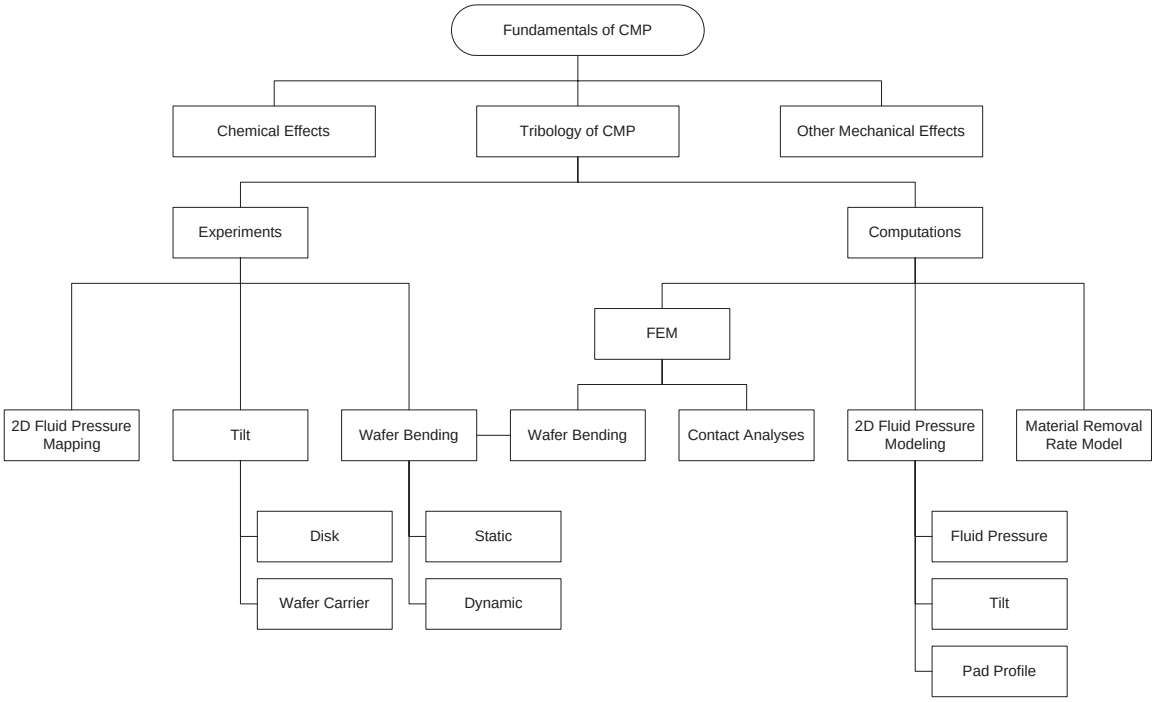

Figure 1.7: Research plan

in the disk can result in a large change to the film thickness distribution. Thus, measurements of the tilt of the disk have to be carried out. In addition, the shape and orientation of the wafer have to be determined. A material removal rate model will also be developed to link the fluid pressure results to removal rate across the wafer.

1.5 Thesis Layout

Chapter 2 will include a literature review on the various aspects of CMP. Finite element analyses on the static loading of the wafer will be presented in Chapter 3. Chapter 4 will describe and discuss the experiments including fluid pressure mapping, wafer bending measurements and wafer tilt measurements. Chapter 5 will present the model and comparisons of the predicted results with the experimental results. A material removal rate model based on mechanical abrasion will be pre-

sented in Chapter 6. Model results will be compared to silicon oxide polishing data. Chapter 7 will conclude the findings.

CHAPTER 2

LITERATURE REVIEW

Polishing is a complicated process with a large number of interdependent variables involved. This chapter categorizes the research in the literature into six areas: chemical effects of the slurry, wafer film stress, wafer pattern dependencies, abrasive particles, pad and the fluid mechanics.

2.1 Chemical Effects

Much of the current understanding of CMP is derived from experiences of glass polishing in the preparation of optical lenses. Since the silicon oxide used in the IC industries is a form of silicate glass, oxide CMP is a specialized form of glass polishing. Cook [9] provided a good summary of the chemical processes in glass polishing. He postulated that water entry into the oxide surface weakens the glass network by breaking the Si-O bonds. Once all of the Si-O bonds of a Si atom are hydrated, $Si(OH)_4$ is formed which is highly soluble in water. He further suggested that increases in hydrostatic pressure will promote water diffusion into the glass network. The role of the abrasive particle is to build up hydrostatic pressure at the leading edge of the particle, pumping water into the glass network. At the trailing edge of the particle, due to the relief in hydrostatic pressure and tensile film stress, $Si(OH)_4$ is precipitated out of the network and gets dissolved into the solution.

Tomozawa [10] proposed similar mechanisms happening during the polishing of silicon oxide used in the semiconductor industry. In addition, he showed that the

decrease in hardness of silica glass with loading time during hardness testing is the result of water diffusion into the glass [11]. He conducted Knoop hardness tests on silica glass in water, benzene, acetone, acetonitrile, formamide and hydrazine. The hardness is independent of loading time in all liquids except water. Infrared absorbance spectra on the indentation showed water absorbed into the glass. Nogami et al. [12] conducted water diffusion experiments into silica glass slides stressed by a four-point-bending rig. They found that the diffusion coefficient of water increased exponentially with increasing tensile stress and decreased with increasing compressive stress. Another test on silica glass slide under hydrostatic pressure showed that the solubility of water in glass increased with increasing hydrostatic pressure.

Kaufman et al. [13] proposed that during the CMP of tungsten, a tungsten oxide film formed on the tungsten surface to prevent further chemical etching of the tungsten. This oxide film was softer than the tungsten metal itself. The role of the abrasive particles in the slurry was to remove this oxide layer and expose the bare tungsten underneath. The chemicals then attacked the bare tungsten to form a new layer of oxide film and the process repeated itself over and over again. Planarization occurred when only the high areas of the wafer were abraded by the abrasives, while the low areas were not abraded and were protected from further chemical etching by the passive oxide layer. As time progressed, the different in height between the high and low areas would decrease until they were at the same level. A similar model had been proposed for the copper CMP process [14].

Liu et al. [15] conducted polishing experiments on 150 mm wafers coated with phosphosilicate glass (PSG) and wafers coated with borophosphosilicate glass (BPSG) using PECVD. An IC1000/Suba IV pad and a fumed silica slurry were used. Fourier

transform infrared (FTIR) measurement was used to characterize the film structures. Nanoindentation experiments showed no significant effects of boron and phosphorus doping on the hardness of the films. But there was a difference in hardness between PECVD oxide and thermal oxide. Thermal oxide has a higher hardness than PECVD oxide. Polishing results indicated that for the PSG wafers, an increase in phosphorus concentration caused an increase in the polishing rate. For the BPSG wafers, an increase in the boron concentration caused an increase in the polishing rate also. They mentioned that in a previous work, they had proposed that there was a linear relationship between hardness and polishing rate for undoped dielectric film. In this research, no distinct relationship can be drawn for doped films. Hence, they proposed that chemical reaction played an important role in the CMP of doped wafers. The phosphorus incorporated in the PSG films may act as bridging atoms or interposed atoms. They may exist in the forms of P_2O_3 and PH_3 molecules loosening the structure of the host SiO_2 network. In the case of the BPSG films, B_2O_3 and P_2O_5 work as impurities in the SiO_2 network, affecting its properties.

There is a substantial amount of literature on electrochemical studies on the role of oxidants, complexing agents and inhibitors in controlling etch rates during CMP [16] that will not be covered here. A wealth of knowledge and experience is also in the hands of slurry manufacturers in the form of trade secrets and propriety information.

2.2 Film Stress

Baker [17] tried to explain the origin of the edge effects by modeling the wafer as a rigid flat, pressing against a structured pad consisting of a harder top pad and a softer base pad. The composite pad was modeled as an elastic plate on a

Winkler elastic foundation. The top pad deformed only by bending and the base pad is significantly softer than the top pad it supported. The bending of the top pad under a uniformly distributed downward pressure gave rise to nonuniformity in contact pressure close to the edge of the wafer. This contact pressure, in turn, gave rise to the nonuniform polishing rates at the edge of the wafer.

Zhang et al. [18] found that CMP removal rate and nonuniformity were affected by pre-polished thin film stress. A non-contact capacitive gauge system was used to measure the wafer shape before polishing to elucidate the film stress. Their results indicated that a tensile film stress resulted in higher CMP removal rate while a compressive film stress gave better removal uniformity. Tseng et al. [19] obtained similar results. They found that decreasing the magnitudes of tensile pre-polished silicon oxide film stresses resulted in lower material removal rates, whereas decreasing the magnitudes of compressive film stresses resulted in higher material removal rates. This could be explained by observations of Haque et al. [20] who found out that film stress has an effect on the diffusion of moisture into the structure of plasma-enhanced chemical vapor deposited silicon dioxide films. Strained Si-O bonds in the silicon dioxide network are more susceptible to attack by water molecules forming Si-OH. As discussed in the previous section, this will lead to the formation of $Si(OH)_4$ which is soluble in water.

McGrath et al. [21] investigated the dependence of the removal rate of PETEOS film on film stress. Six inch silicon wafers deposited with PETEOS film at 10 different deposition powers were polished with a standard commerical set of consumables: IC1000/Suba IV pad, Cabot SS12 slurry and Applied Materials Mirra CMP tool. Pre- and post-CMP film stresses and film thicknesses were measured. Results indicated that films with tensile stresses gave higher removal rate than films with

compressive stresses. They proposed a model for the removal rate in the form of $R = K_p PSe^{b\sigma}$ where K_p is the Preston constant, P is the applied pressure, S is the speed, σ is the thin film stress, and b is some constant possibly a polishing index for a material.

Wang et al. [22] and Murthy et al. [23] attributed within-wafer-nonuniformity (WIWNU) including edge effect to the distribution of von Mises stress across the wafer. They modeled the static contact between the wafer and the pad with the inclusion of a carrier film and the wafer carrier. Using finite element software, they showed that the von Mises stress distribution on the surface of the wafer correlated well with the location of edge effects in typical oxide polishing experiments. They proposed that the removal rate is directly linked to the von Mises stress instead of the individual stress components. Mejia et al. [24] utilized a two-dimensional finite element model with plane strain assumptions to predict the von Mises stress distribution on the wafer. They introduced a shear stress at the wafer and pad interface without slipping to simulate the conditions of CMP. They found that when the wafer/retaining ring gap separation is zero and the wafer and ring pressures were the same, the stress nonuniformity at the wafer edge could be eliminated. As the retaining ring pressure is increased to magnitudes higher than the wafer pressure, one of the peaks in the von Mises stress profile increased. Their model also agreed with experimental observations that increasing the relative wafer and pad velocities will lead to improved WIWNU.

2.3 Pattern Dependencies

Park et al. [25] carried out the polishing of 200 mm patterned wafers containing arrays of copper lines embedded in TEOS silicon oxide. Three characterization

masks were used to create the patterns on the wafers: an area mask that contained block structures with sizes ranging from 20 x 20 μm to 3 x 3 mm, a pitch mask that contained vertical lines with pitch values from 2 μm to 1000 μm at a constant pattern density of 50 percent, and a density mask that contained vertical lines with pattern densities from 4-100 percent at a fixed pitch of 250 μm. Optical and stylus profilometry measurements were made after the polishing to obtain the dishing and erosion values. Results obtained from the area mask pattern showed that the dishing of copper blocks increased as the size of the blocks were increased. Similar results were obtained from the pitch mask pattern where dishing increased with pitch. Since pattern density was fixed at 50 percent for the pitch mask, increasing pitch would also mean increasing linewidth. The erosion on the other hand, decreased with increasing pitch indicating dependence on the oxide line space. For the density mask pattern which is at a fixed pitch, increasing pattern density showed increase in the erosion of the oxide. This is again due to the decrease in the oxide line space.

Warnock [26] modeled the polish rate as a function of three empirical factors: 1) the kinetic factor or horizontal component in the polish removal rate associated with the pad speed, 2) the accelerating factor associated with points which protrude above their neighbours, and 3) the shading factor describing how the polish rate is decreased by the effect of neighboring protruding points. The polish rate is proportional to both the kinetic and accelerating factor, and inversely proportional to the shading factor. He used an iterative procedure to compute the removal rate on patterned silicon oxide features. Silicon oxide film wafers with arrays of different combinations of linewidth and pattern density were polished and analysed for removal rate profiles. His predicted results were able to match well with the experimental data.

Boning et al. [27, 28] developed empirical layout pattern dependent models based on key parameters such as "planarization length" and "planarization response function" that characterize a given CMP consumable set and process. Once extracted through experiments using carefully designed characterization mask sets, these parameters can be used to predict polish performance in CMP for arbitrary product layouts. They have applied their model to both oxide and copper pattern layouts. Their mask set designs are widely used to study pattern dependent effects.

Yang [29] developed a model for the CMP of copper dual damascene based on the multistep, multislurry process platform. His model predicted copper dishing and ILD erosion for three steps copper CMP. The first step involved a fast copper removal slurry, the second low pressure step for copper clearing, and a final step for diffusion barrier removal. He assumed elastic pad material and computed differences in contact pressure between high and low areas based on step height difference. Preston equation [30] was used to calculate removal rates but the model relied heavily on empirical data of Preston's constants for copper, tantalum and silicon oxide.

Sawyer [31] used a two parameter elastic foundation model for the pad and predicted dishing and erosion for copper CMP. The model was similar to a beam on elastic foundation where the first foundation parameter described the gross pad deflection and the second foundation parameter described the coupling between neighboring elements of the pad. Archard wear law was used to model differential wear between materials of different hardnesses. His computations were able to predict dishing and erosion trends for a variety of copper linewidths and pattern densities. His results indicated that the recession of the copper array (erosion) was more sensitive to the surface area fraction of the copper than the line width of the

copper.

Based on the work by Greenwood et al. and using the Preston model, Vlassak [32] modeled the contact mechanics of pattern wafer polishing. He modeled the heights of the asperities as following an exponential distribution. Dishing and erosion resulted due to difference in selectivities between the metal and dielectric. His model predicted that dishing increased with the linewidth of the metal while erosion increased with the pattern density.

2.4 Abrasive Particles

Luo et al. [33–35] postulated that abrasives caught in the tips of the asperities of the pad and the wafer were responsible for material removal from the wafer. They modeled the abrasive-wafer and abrasive-pad solid-solid contacts as plastic contacts. The model is dependent on the number of particles present at the tips of the asperities of the pad. They explained the experimental phenomenon called material removal saturation. As observed, the material removal rate increased linearly with abrasive weight concentration but leveled off at a certain critical concentration. They postulated that material removal saturation is caused by the saturation of the wafer-pad contact area by the abrasives. Zhao and Chang [36] also have a similar model on the basis of elastic contact between pad and abrasives, and plastic contact between wafer and abrasives.

Zettner et al. [37] visualized the interactions between the wafer, pad and particles using total internal reflection fluorescence (TIRF). The setup consisted of a smooth glass disk representing the pad rotating a distance above a stationary glass plate representing the wafer. The pad was held parallel to the wafer. The gap between the wafer and the pad was flooded with an aqueous suspension of fluorescence particles.

A laser beam shining at the bottom surface of the glass wafer underwent total internal reflection and generated an evanescent wave. The image of the fluorescence particles were then captured by a CCD camera. Results showed that the average particle velocity increased with shear rate, and the average velocity normalized by pad speed decreased with Reynolds number.

Choi et al. [38] performed friction force measurements during the polishing of a sapphire wafer using slurries consisting of silica particles. He found that friction force increased with down force and solid loading of silica in the slurry. In addition, he discovered that 1.0 μm silica particles resulted in higher friction force than 0.2 μm particles under the same down force and solid loading situations.

2.5 Pad

Achuthan et al. [39] looked at the effect of conditioning during the CMP of silicon oxide films. Polishing results on 150 mm thermal oxide wafer over a variety of combinations of load, speed and polishing time indicated that *in situ* conditioning gave higher material removal and better removal uniformities across the wafer than *ex situ* conditioning. They also studied pad deformation by sweeping a 4 inch conditioning disc across the pad during conditioning for different loads, pad speeds and abrasive grit sizes. Diametric profiles of the pad after conditioning showed two prominent grooves corresponding to the track of the disc. Low pad removal was seen at the edges and central region of the pad. Larger loads were observed to cause deeper grooves. Very small increase in pad removal was seen when the pad speed was increased. Two discs consisting of different size diamond particles were also used: an 80 grit (mean particle size of 175 um) and a 100 grit (mean particle size of 147 um). Result showed that the wear caused by the 80 grit was slightly higher

than the 100 grit.

Li et al. [40] observed that the dynamic shear modulus of an IC1000 pad decreased to two thirds of its dry value during 5 hrs of water soaking, while its oxide removal did not change significantly. The dynamic shear modulus of the pad also decreased with increasing temperature. They suggested that it was the surface, rather than the bulk, characteristic of a polishing pad that had the most significant impact on the oxide removal rate. Their experimental results indicated that a non-conditioned polishing pad provided a lower oxide removal rate but a higher planarization efficiency than a well-conditioned pad. The oxide removal rate and planarization efficiency also increased with increase in slurry temperature.

Xie and Bhushan [41] conducted polishing of Ni-Zn ferrite and pure copper block specimens on a bench top polisher. They suggested from experimental results and theoretical predictions that the wear rate increased with an increase in particle size, hardness of polishing pad, nominal contact pressure, and with a decrease in elastic modulus of the polishing pad. Surface roughness increased with an increase in particle size and hardness of polishing pad, and nominal contact pressure had little effect on the roughness. Evans and Oliver [42] performed fixed wafer polishing of unpatterned PECVD TEOS silicon dioxide coated wafers. They observed a "leading edge effect" characterized by high material removal rates at the leading edge of the wafer. At the trailing edge, material removal rates decreased rapidly.

Moon et al. [43, 44] conducted polishing of bare silicon wafers using a slurry consisting of 70-90 nm colloidal silica particles. A load cell was used to monitor the friction force during the polishing. Material removal was determined by weighing the wafers before and after polishing. Three commercially available pads were tested: Suba500, IC60 and UR100. The Suba500 was an impregnated felt

substrated-coagulated urethane in a fiber matrix. The IC60 was a microporous polyurethane polishing material. The UR100 was a napped poromerics-porous urethane layers on supporting substrates. Their results indicated that polishing rate was inversely proportional to the pad density, but polishing rate was proportional to both pad compressibility and friction force. They proposed that pad density and compressibility were strongly related by the number of pores and pore size in the pad microstructure. A more compressible pad will result in larger real contact area between the pad and the wafer. This will cause more abrasives to be trapped in these areas, resulting in higher material removal and friction force.

Yu et al. [45] proposed the first statistical polishing pad model for chemical-mechanical polishing. They modeled the pad using the Greenwood and Williamson model and assumed the pad surface heights as Gaussian distributed. They used Preston's equation to model the material removal and proposed that the Preston constant be split into two components: one of surface chemistry and one for abrasion effects. They proposed that the size of the pad asperities relative to the width of the trench in patterned wafer played an important role in dishing. If the tip of the asperity, which is assumed to be spherical in shape, is larger than the width of the trench, material removal from the bottom of the trench is limited. Another aspect they proposed was the viscoelastic nature of the pad. The asperity does not deform instantaneously as it entered the trench, resulting in limited material removal from the bottom of the trench.

Zhao and Shi [46] attempted to explain the inconsistencies seen between the Preston's equation and experimental observations concerning pressure dependence of the polishing rate. Preston's equation was derived from glass polishing involving hard pads whereas CMP used soft pads. There was a fundamental difference as to

how load was transmitted from the pad to the particles and then to the wafer. For a hard pad, a change in the applied force caused a change in the indentation depth of the particles into the wafer. With a soft pad, an increase in the applied force caused the particles to embed deeper into the asperities of the pad. The contact area between the wafer and the pad also increase. More particles got into the contact area but the force per particle did not increase as much. Consequently, indentation depth of the particles into the wafer was decreased. They proposed a $P^{2/3}$ dependence of the removal rate on applied pressure and were able to show agreement with silicon oxide polishing data.

2.6 Fluid Film

Runnels [7] et al. developed a flow model of the CMP process using the Navier-Stokes equations for incompressible Newtonian flow with constant viscosity. He modeled the pad as a rigid flat and the wafer as having some curvature. His results showed the existence of a fluid layer and sensitivity of the minimum film thickness to the pad rotational speed, wafer curvature and viscosity of the fluid. This led him to suggest that the wafer-pad interface was a very delicate balance between hydrodynamic lubrication, mixed solid-liquid contact, and possibly even some direct solid-solid contact.

Coppeta et al. [47] developed an optical technique using dual emission laser induced fluorescence to measure the slurry film thickness between a glass wafer and the pad. They discovered that there existed a maxima in fluorescene intensity when the slurry was injected at 33 percent of the pad radius. They also found that increasing pad conditioning will increase the fluorescene intensity and explained it in terms of pad topography. Deeper trenches and grooves cut by the conditioner

will increase the film thickness causing larger fluorescence intensity. They did not find a big effect of platen speed on the fluorescence intensity. Using the same technique, Coppeta et al. [48] measured the residence time of slurry under the wafer and introduced a slurry transport efficiency, defined as the percentage of new slurry beneath the wafer. They found out that average fluid residence times decreased linearly with platen speed. Increasing slurry flow rate caused a decrease in the fluid residence time. They found out that pad topography had a big effect on the slurry gradients across the wafer. *In situ* conditioning increased the slurry mean residence times and promoted slurry mixing. *In situ* conditioning also reduced slurry gradients across the wafer.

Levert [49, 50] measured the vertical differential wafer displacements of 75 mm and 100 mm diameter non-rotating wafers. He ran the experiments with the IC1000 pad (with and without perforations), and water and slurry for the fluid. He observed a negative vertical differential wafer displacment of up to 10 μm and an increase in frictional drag. Both the magnitudes of the vertical differential wafer displacement and the frictional drag increased with pad speed. This indicated a suction force at the wafer-pad interface. Levert also measured the fluid pressure at the interface of a 100 mm stainless steel disk and the pad. The disk was prevented from rotating and a diametric row of holes from leading to trailing edge were drilled through the disk so that the fluid pressures at those locations could be sampled with a manometer or pressure transducer. His results revealed a negative fluid pressure profile for about three-quarters way from the leading edge followed by a smaller positive pressure region at the trailing edge. He measured the greatest negative pressure of -62.3 kPa at a pad linear speed of 0.7 m/s. Neither wafer displacement nor coefficient of friction changed with variations of the normal load (from 34.5 to 62.1 kPa). The

magnitude of this sub-ambient pressure was on the order of the applied load and this could change the distribution of contact stresses at the interface. Since the polishing process was strongly dependent on the contact pressure [30], it would cause non-uniformity in material removal across the wafer. He developed a one-dimensional "suction cup" model [51] whereby the voids in the pad underwent compression and decompression because of contact pressure variations between the disk and pad. The contact pressure variation was based on the one-dimensional result for a rigid punch sliding on an elastic half-space. The "suction" cup model was executed by using the equation for Poiseuille flow between two parallel plates. The model could predict negative pressures but the more dominant Couette flow driven by the shear of the fluid between the disk and the pad was not incorporated. Based on Levert's results, Tichy [52] et al. modeled the contact between the disk and pad as a distributed line loading on a semi-infinite medium to elucidate the deflection of the pad substrate. The asperity deflections were modeled with the Winkler or "mattress" model. The fluid pressure was computed using one-dimensional Reynolds equation [53] with "long bearing" approximation. His model was able to predict the negative fluid pressures.

Mess [54] measured the vertical displacements of a polishing pad sliding on a sapphire disk. He detected a 7 μm maximum negative differential displacement suggesting the existence of a suction force. He postulated that the voids on the surface of the pad were only partially filled with water or slurry. This resulted in the capillary forces pulling the pad towards the disk. Based on his computations, he reported that the capillary forces associated with the voids in the pad could account for 4 μm of this negative displacement. However, capillary forces alone could not result in the negative and positive fluid pressures at the disk-pad interface. The

speed effect on the fluid pressure magnitude could not be accounted for also. Pads that are soaked for weeks or even months still result in negative pressures even though water would have penetrated the voids completely.

Shan [55–57] measured the fluid pressure with the same apparatus as Levert as a function of pad surface roughness, pad elastic modulus and fluid viscosity. He compared the results for an IC1000 pad with an average surface roughness of 5.0 μm, with an IC1000 pad topped with a mylar tape having an average surface roughness of 0.5 μm. The latter showed a smaller magnitude of negative fluid pressure. Using two pads with different elastic modulus, he found out that the stiffer pad gave a lower magnitude of negative fluid pressure. Using water and a higher viscosity glycerin-water solution, he was able to show that higher viscosity gave a higher magnitude of negative fluid pressure. He also observed the effects of disk curvature using a 100 mm steel disk whose surface was deflectable with a set screw. Positive fluid pressure was detected at the disk-pad interface when the disk had a 50 μm center-to-edge difference in surface height. He modeled the CMP configuration as a punch (the wafer) sliding on an elastic half-space (the pad) [5]. The pad was modeled as a rough surface containing asperities with a certain height distribution, using the Greenwood and Williamson equation [6]. The final one-dimensional pressure profile was generated using the one-dimensional Reynolds equation [53] with "long bearing" approximation. The model was able to predict the trend in the one-dimensional pressure measurements. He suggested that a "nano-film" existed between the load supporting asperities on the polishing pad and the wafer. Mechanical polishing could only occur when the mean abrasive size was larger (2-3 times for the softer metal and polymer films, and 1-2 times for the harder ceramic films) than the average "nano-film" thickness. Abrasive size larger or smaller than this would lead

to reduced material removal rate. Following his work, Zhou et al.[58, 59] performed oxide polishing with slurries of different abrasive sizes and discovered that there existed an optimal removal rate with a certain abrasive size. She computed the average thickness of the nano-film by the soft-EHD empirical equation and found the value to be between 42-66 nm [60] for the range of load and speed, which is 0.5-0.8 times the optimal abrasive size of 80 nm from the polishing experiments.

Several approaches were taken to predict the two-dimensional fluid pressure profiles. These models employed the finite-element method (FEM) to determine the contact stress that produced the resulting film thickness. That film thickness was then used to determine the hydrodynamic fluid pressure. Shan [61] used a FEM analysis of the pad being indented by a rigid punch to compute the fluid film thickness. He modeled the elastic pad with asperities as two media with asperities having an elastic modulus of approximately one-half that of the bulk pad. Kim et al. [62] employed a hyper-elastic asperity model to quantify the behavior of the asperities relative to the bulk. In their "soft-hydrodynamic" approach, they were able to predict a film thickness that varied in two-dimensions for a balanced system of forces and moments, which resulted in the prediction of the two-dimensional fluid pressure. Both approaches obtained sub-ambient pressures, but the models did not predict the positive pressure region seen in the one-dimensional experiments.

2.7 Concluding Remarks

Chemistry plays a very important role in CMP whether it is directly responsible for material removal or is assisting the removal by mechanical action. The general belief for metal (e.g. copper and tungsten) CMP is that it is the abrasive action that makes the final removal of material after chemistry has altered the properties

of the surface. Some believe it to be the other way round where the dissolution of wafer material is assisted by the pressure and strain fields created by the abrasive particle. The exact relationship between chemisty and the abrasive particle is still vague. In most mechanical models of material removal, the particle indentation model is used. In this model, the particle first indents the surface of the wafer and then gets dragged across the wafer. Material gets removed by either repeated and overlapping ploughing or by cutting action. Given the small size of the abrasive particles used in CMP, typically less than 200 nm and some as small as 10 nm, the depth of indentation would be very small. Zhao and Chang [36] obtained a value of 0.0025 nm for a 10 nm alumina particle indenting into a tungsten wafer. Luo et al. [34, 35] proposed particle indentation depths ranging from 0.1 to 1 nm for CMP. With atomic diameter in the order of 0.2 nm, this would mean sub-atomic removal or removal at the atomic level. Cook [9] suggested that at the scale of interaction during polishing (in terms of single silica tetrahedra or small multiples), the process is chemical removal rather than mechanical.

One of the least understood component of CMP is the polishing pad. Studies on the effect of hardness and compressibility of the pad on removal rate and removal uniformity are inconclusive due to the difference in the structure and morphology of the pads used. Film stress on the wafer is seen to have an effect on the removal rate as observed in many studies. In pattern wafer polishing, the effects of linewidth and pattern density on dishing and erosion are well characterized by experiments. Most models predicting dishing and erosion are based on the softer pad bending into the metal or metal array, and also on the difference in selectivities of removal between the metal and dielectric. These models can predict the trend well but quantitative adjustments from process to process still require empirical inputs. The

contact and fluid mechanics of CMP are important as it concerns the distribution of contact pressure and fluid flow at the interface of the wafer and the pad. The existence of a net positive or negative fluid pressure will not only affect the contact pressure distribution but also the regime of the hydrodynamics (whether it is mixed lubrication or total separation between wafer and pad).

CHAPTER 3

STATIC CONTACT ANALYSES

The shape of the wafer during CMP is coupled with the film stresses and contact pressures on the wafer. The material removal rate could depend on the type of film stresses (tensile or compressive) and the contact pressure. A variation in the distribution of film stresses and contact pressures across the wafer would give rise to within-wafer nonuniformity (WIWNU). Many attempts have been made to look at the contact between the wafer and the pad theoretically. Most of these models consider the static loading of a wafer against the pad. In static loading, the pressure distribution at the bottom surface of the wafer is not uniform. There exists pressure peak at the edge of the wafer. The wafer carrier is a steel disk that is relatively much more rigid than the rest of the components. Due to the difference in boundary conditions on the carrier film side and pad side of the wafer, the wafer should bow. However, the amount of bowing is the issue here.

This chapter provides an analysis of the static contact conditions involving the stainless steel disk and the pad (the pressure measurement configuration), and that involving the actual CMP configuration. The latter consists of the wafer carrier, carrier film, wafer and pad as shown in Figure 3.1. The finite element method using ANSYS 7.1 software is used to analyze these two cases. Since all geometries, forces and boundary conditions are axisymmetric, two-dimensional axisymmetric models in ANSYS are used. Two-dimensional, eight-node elements are used to mesh the components. In addition, contact elements are used to simulate the contact

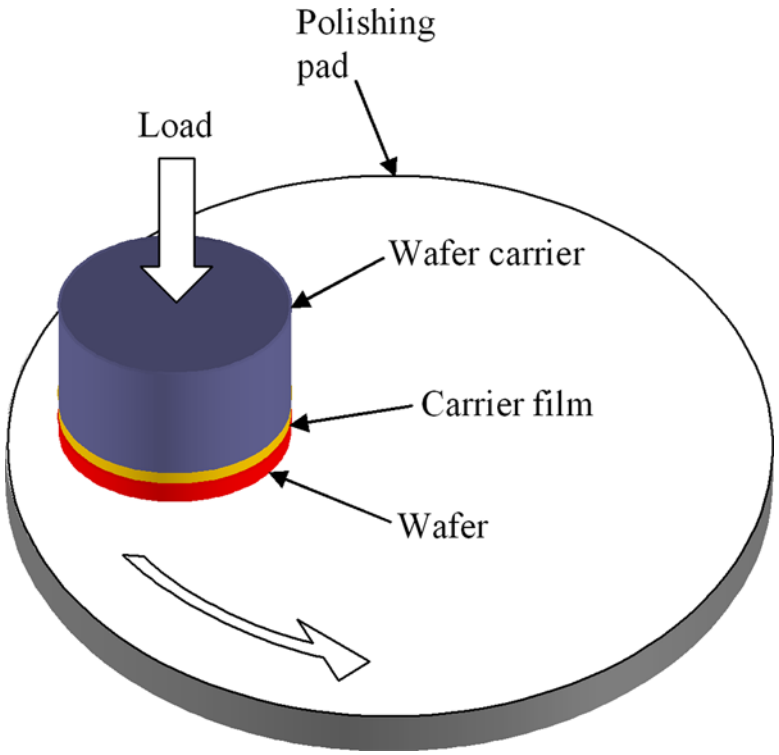

Figure 3.1: Typical CMP setup showing the "sandwich" configuration of the different components under loading

conditions at the interfaces.

A static wafer deflection experiment is also carried out to measure the amount of wafer bowing in typical CMP configuration to validate the FEM model.

3.1 Pad Model

The polishing pad is probably the least understood component in CMP. Hence, there is some variation in pad modeling found in the literature. Shan [61] modeled the pad as two layers of linear-elastic materials: the asperity layer and the bulk pad. The elastic modulus of the asperity layer was one-half that of the bulk pad in his finite element model. Seok et al. [63] employed a hyper-elastic asperity model to quantify the behaviour of the asperities relative to the bulk pad. Their finite element model was based on the deformation of hyper-elastic asperities attached

to a linear-elastic pad. They adopted the two parameter Mooney-Rivlin (M-R) constitutive model [64] to account for the nonlinear-elasticity of the asperities. In order to extract information on the film thickness profile due to asperity compression, both models described above treated the asperity layer and bulk pad as separate entities. Most other pad models treated the pad as a single entity with linear-elastic properties [22–24].

Many attempts have been made to model the hyper-elastic behavior of rubber-like materials. Some commonly used are the Mooney-Rivlin model and the neo-Hookean model. These models are well suited for solid rubber-like materials that exhibit incompressibility. Ogden built a model for incompressible rubber-like materials [65], and for compressible rubber-like materials [66] also known as the hyper-foam model. One of the most widely used constitutive models for compressible, isotropic, nonlinearly-elastic solids is the generalized Blatz-Ko model for foam-rubber. Blatz and Ko [67] conducted experiments on foamed polyurethane to validate their model. It is on this basis that the Blatz-Ko model is used to model the pad and the carrier film in the following FEM analyses. Note that this model treats the pad as a single entity and does not take into account the asperity layer of the pad. Both pad and carrier film materials have spherical voids dispersed in a matrix of polymeric material. The pad material is polyurethane and is known to have a closed-cell structure. The carrier film material is unknown but it is also foamed and has a more porous opened-cell structure. The simplified Blatz-Ko strain energy function for foamed polyurethane is given by

$$W = \frac{\mu}{2}(J_2 + 2J_3 - 5) \tag{3.1}$$

where μ is the shear modulus and $J_2 = I_2/I_3$ and $J_3 = I_3^{0.5}$. I_1, I_2 and I_3 are the invariants of the deformation tensor. It is from experiments that Blatz and Ko found that the Poisson's ratio for foamed polyurethane is 0.25. Consequently, μ is reduced to (E/2.5) where E is the elastic modulus.

3.2 Contact of Stainless Steel Disk and Pad

This configuration involves a 150 mm diameter stainless steel disk (similar in dimensions to the pressure measurement disk) pressing against a larger diameter pad. The contact pressure result is shown in Figure 3.2. The left edge of the model represents the centerline of the punch and pad. It is constrained from displacing in the horizontal direction. The bottom surface of the pad is constrained in all degrees of freedom since it is strongly adhered to the platen. Load is applied as a uniformly distributed pressure (27 kPa) over the top of the punch. At the interface of the punch and pad, contact elements with friction coefficient of 0.43 are implemented. Two-dimensional, eight-node elements are used to mesh the punch and the pad.

As mentioned in the previous chapter, almost the entire disk-pad contact area is under constant pressure except for a couple of millimeters from the edge where a sharp rise in pressure occurs. Analyses using frictionless contacts, different loads, implementing disk corner radii, and smaller mesh sizes give similar results. Only when the contact size is comparable or smaller than the thickness of the pad does the contact pressure take on a more power-law like profile as shown in Figure 3.3 and 3.4. In the two figures, the thickness of the pad and the applied pressure remains the same but the radius of the punch is reduced to one and one quarter times the thickness of the pad respectively.

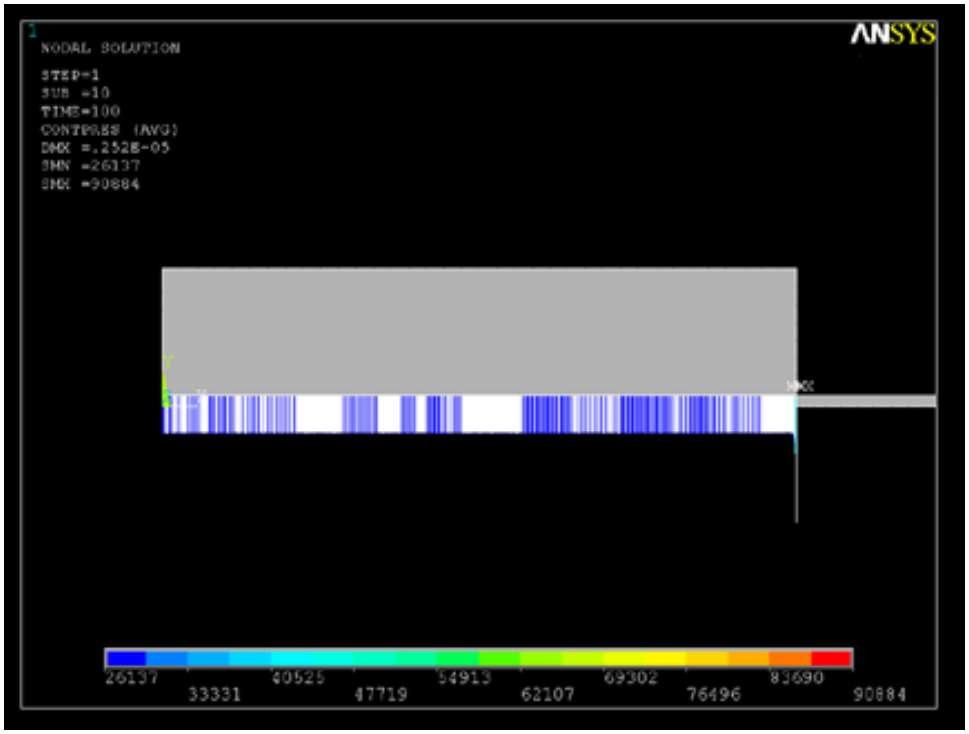

Figure 3.2: FEM contact stress analysis for 150 mm punch

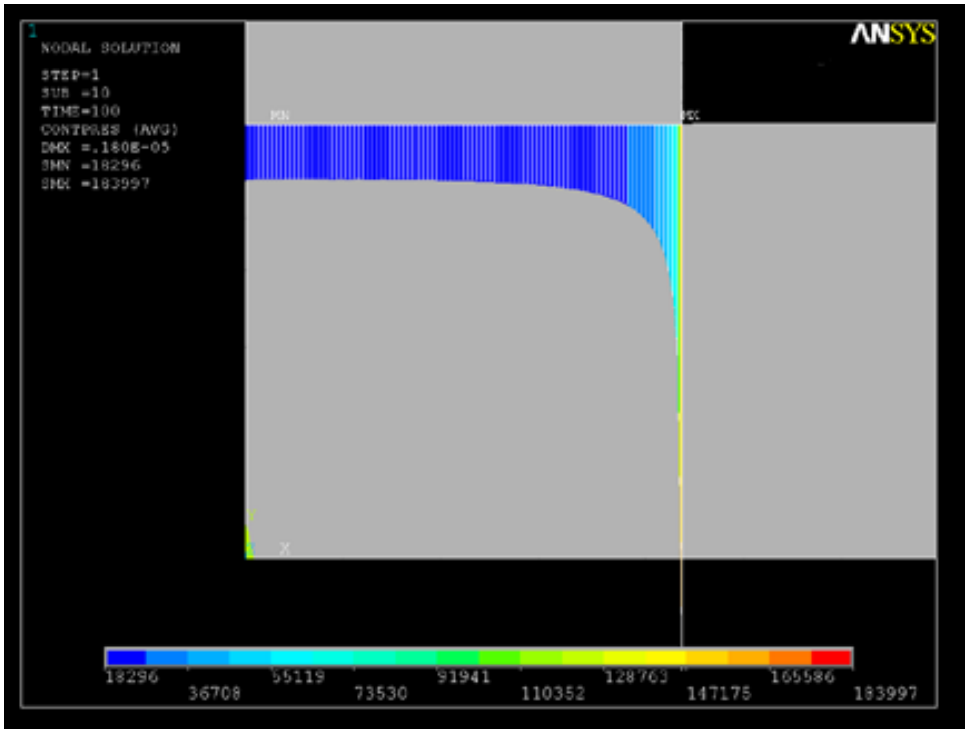

Figure 3.3: FEM contact stress analysis for 2.6 mm punch

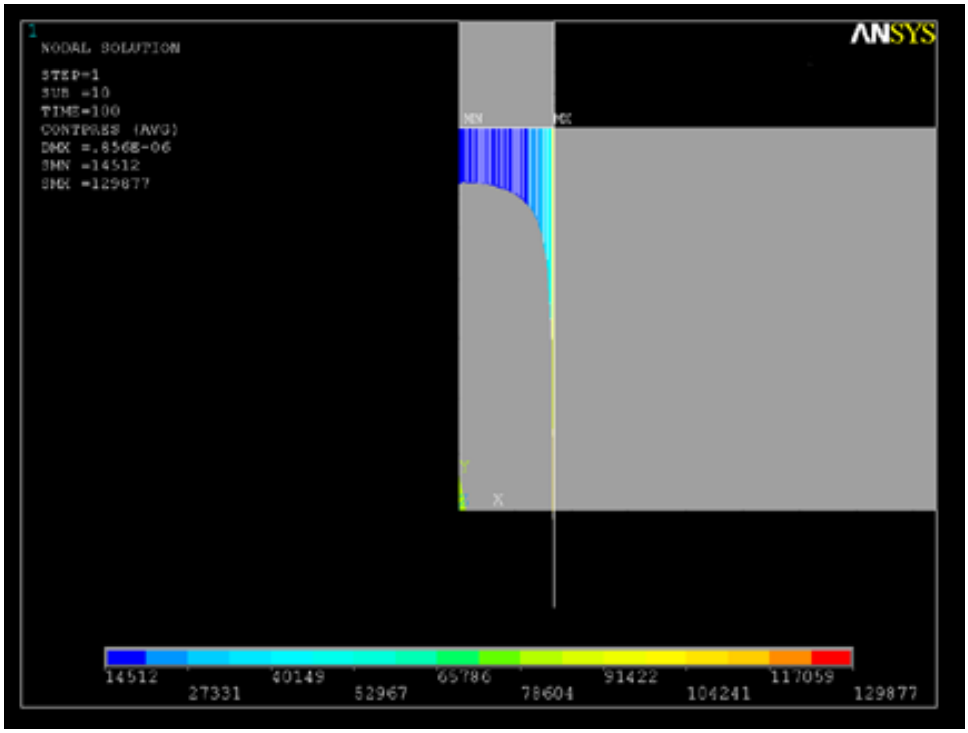

Figure 3.4: FEM contact stress analysis for 0.65 mm punch

3.3 Contact in the Actual CMP Configuration

This section decribes the FEM analysis on the static loading using the actual CMP configuration. The CMP configuration is a layered structure consisting of the wafer carrier, carrier film, wafer and the pad. The contact pressure distribution and wafer bending will be presented along with the stresses in the wafer.

In the model, a fillet radius of 100 μm is introduced to the top and bottom edges of the wafer. The boundary and contact conditions are summarized below.

Boundary conditions:

1) Axisymmetric setup with respect to the center of the wafer.

2) Displacement in the horizontal direction is constrained along the axis of symmetry.

3) All degrees of freedom constrained on the bottom surface of the pad since it is adhered strongly to the platen.

4) Load is applied as a uniformly distributed pressure on the top surface of the wafer carrier.

Contact conditions:

1) Wafer/pad interface coefficient of friction = 0.31 (measured by inclined plane method experimentally).

2) Wafer/carrier film interface coefficient of friction = 0.67 (measured by inclined plane method experimentally).

3) Carrier film is "glued" to the wafer carrier.

Other geometric and physical properties of the model are tabulated in Table 3.1. The two-dimensional ANSYS model is shown in Figure 3.5. Figure 3.6 shows a magnified view of the meshing in the ANSYS model.

A typical set of FEM results is shown in Figure 3.7. The top graph shows the film stresses and contact pressure profile from the center to the edge of the wafer. The contact pressure profile is essentially flat throughout except at the very edge where there exists a peak before going down to zero at the separation of the wafer and the pad. The peak pressure happens less than 100 μm from the edge of the wafer. The von Mises stress plot is flat in the central region of the wafer but rises up to a peak about 4 mm from the wafer edge. There is also a small second peak that coincides with the location of the peak contact pressure. The radial stress has a tensile peak at the same location of the von Mises stress peak. The tangential stress is tensile in the central region of the wafer and has a peak close to the edge

of the wafer. The transverse stress is essentially similar to the contact pressure in profile but is compressive. Since the von Mises stress is a function of the individual stresses, it can be noted that the first peak of the von Mises plot is a result of the peak in the radial stress and the second peak is the result of the transverse stress (or contact pressure).

In addition, the wafer profile is plotted to look at the amount of wafer bending as a result of static loading. As seen in Figure 3.7(b), the wafer experiences a certain degree of bending. The wafer bends upwards by about 0.14 μm at the edge as a result of the peak contact pressure.

From Figure 3.7(a), it is clear that the peak in the radial stress is a result of the wafer bending. Due to the high stiffness of the wafer material, a small amount of curvature is sufficient to generate high stresses. The radial stress on the top surface of the wafer at the same radial location experiences a peak compressive stress due to the bending.

A typical material removal profile for silicon oxide polishing is shown in Figure 3.8 [60]. The material removal is quite uniform in the central region of the wafer but within 5 mm from the wafer edge, the material removal starts to oscillate in a certain manner. The peaks in material removal occurs at the edge and 2.5 mm from the edge of the wafer. This form of within-wafer nonuniformity (WIWNU) is known as the edge effect. This zone is very visible especially in polished silcon oxide wafers and is seen as a series of colored rings at the periphery of the wafer. Due to the poor uniformity in this zone, also called the edge exclusion, devices are not designed to be in this zone. Going back to the von Mises stress and contact pressure generated by ANSYS, it seems that von Mises stress correlates better with the polishing results, based on the location of stress concentrations. The von Mises

stress concentrations occurs around 4 mm and 100 μm from the edge. The peak in removal rate closer to the wafer edge is a result of the peak contact pressure while the peak further in is a result of the tensile stresses on the wafer. Further analyses show the location of the peaks in the von Mises stress does not change significantly with load and wafer size. This suggest that the edge effect is very localized and is not much affected by the size of the wafer. Figure 3.9 shows the von Mises profile for a 100 mm diameter wafer with a 50 kPa applied pressure. The profile and occurence of the peaks are very similar to Figure 3.7 and to Figure 3.8. The results seem to suggest that the Preston relation of material removal rate being dependent only on pressure and velocity could not be applied to this edge exclusion region. Rather, film stress as discussed in Chapter 2 seems to play a role here.

Figs. 3.10 and 3.11 show the results when the carrier film and pad are rigid (by setting their elastic modulus to very high values) respectively. In both cases, the amount of wafer bending is reduced drastically ($\approx 0.02\ \mu m$) since the rigidity of the carrier film or the pad restricts any bending. As a result, the peak von Mises and radial stresses disappear.

3.3.1 Static wafer deflection experiment.

A 270 x 210 x 600 mm, static compression rig was designed and fabricated to carry out the static wafer deflection or bending measurements. As shown in Figure 3.12, the apparatus consists of a 90 mm thick base with a structure to hold the stainless steel shaft where the load is transmitted to the wafer carrier. The base is ground to a flatness of 2 μm and an IC1000 pad (about 1.3 mm thick) is adhered on top of it. The load is produced by dead weights that are placed on the stainless steel shaft which goes through a linear bearing in the structure.

Table 3.1: Material properties and physical dimensions

	Elastic modulus (MPa)	Poisson's ratio	Radius (mm)	Thickness (mm)
Wafer carrier	197000 [68]	0.27	75	15
Carrier film	1	0.25	75	0.7
Wafer	130000 [69]	0.279	75	0.68
Pad	12	0.25	150	1.3

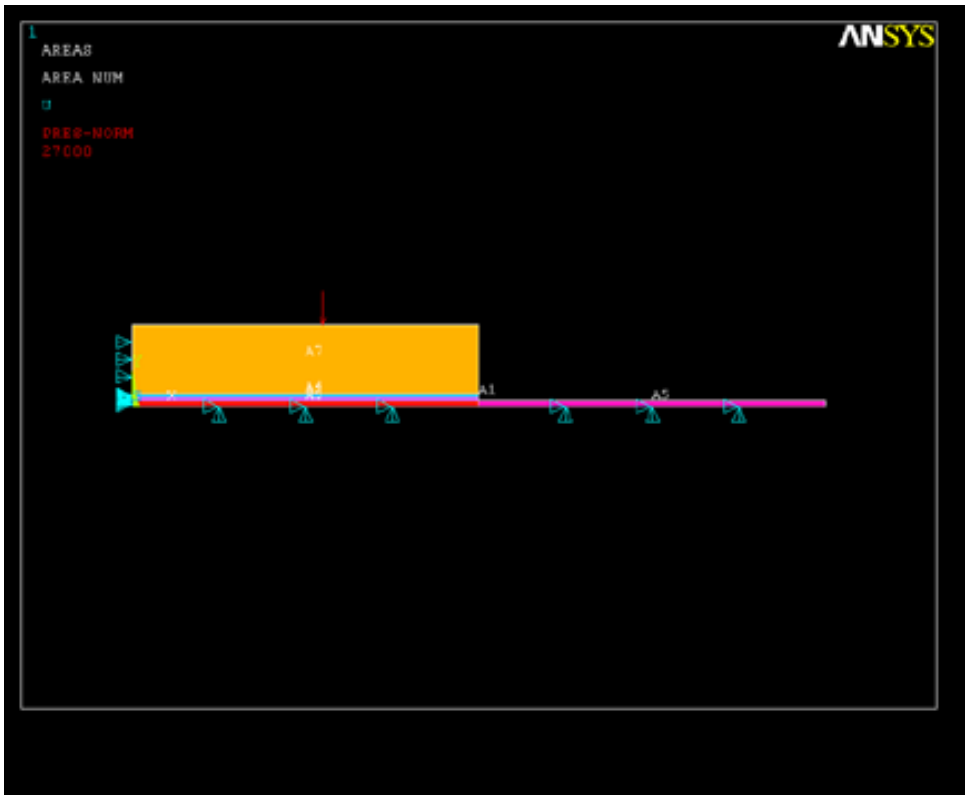

Figure 3.5: FEM contact model

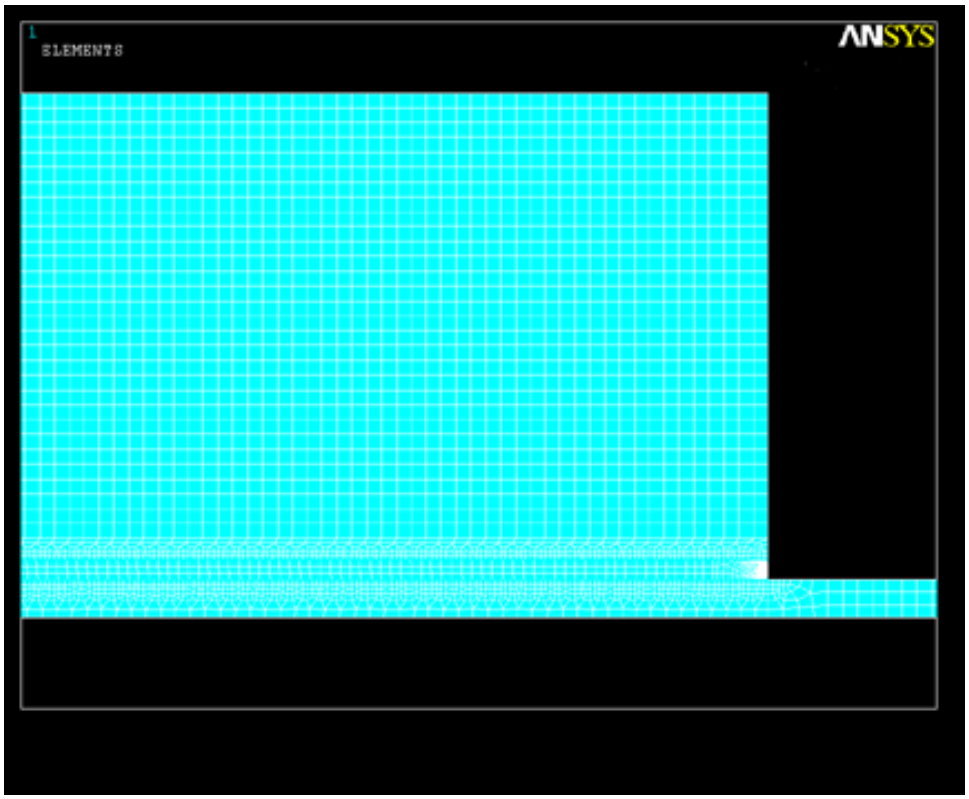

Figure 3.6: FEM mesh

The wafer carrier is a 150 mm diameter, 15 mm thick stainless steel disk. It has a gimbal joint where there is a conical cavity at the center of the top surface to accommodate a stainless steel ball. The load from the stainless steel shaft is transmitted through this ball to the wafer carrier. Eight holes are drilled and tapped along a diametric axis of the wafer carrier to hold eight capacitive probes. The Capacitec HPT-40 series probes are threaded and cylindrical in shape with a length of 14 mm and outer diameter of 4.75 mm. The sensor diameter is 1.02 mm with a sensitivity of 0.05 μm/mV and a linear range of up to 750 μm. In the experiments, the probes were operated in the 400 to 600 μm gap range. The probes are connected to a power supply and the signal amplified and monitored. The bottom surface of the wafer carrier is machined to within 2 μm flatness before a carrier film (about 0.7 mm thick) is adhered to it. Prior to that, eight holes are punched through the

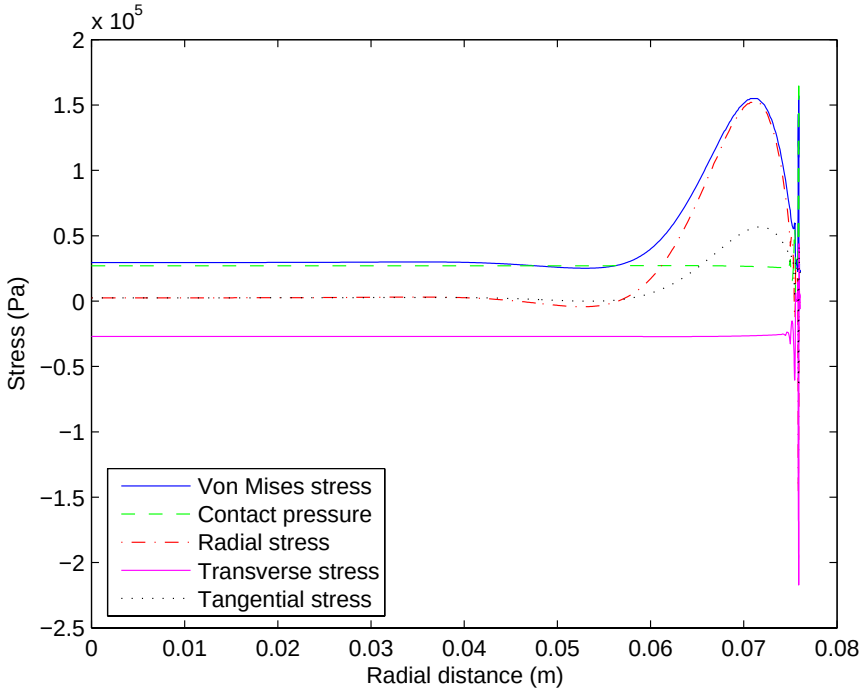

(a) Film stresses and contact pressure

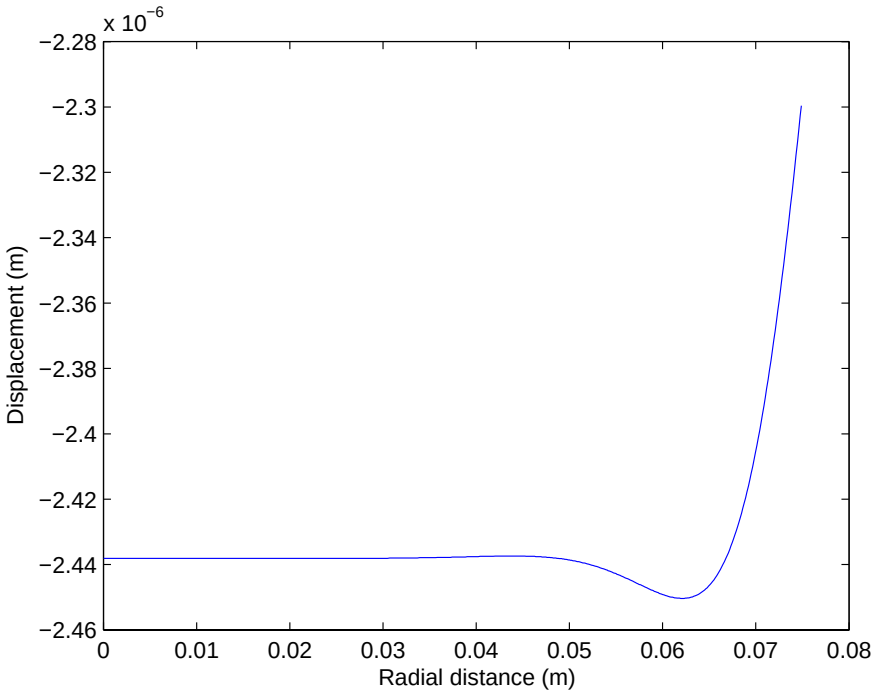

(b) Wafer profile

Figure 3.7: FEM results at 27 kPa load

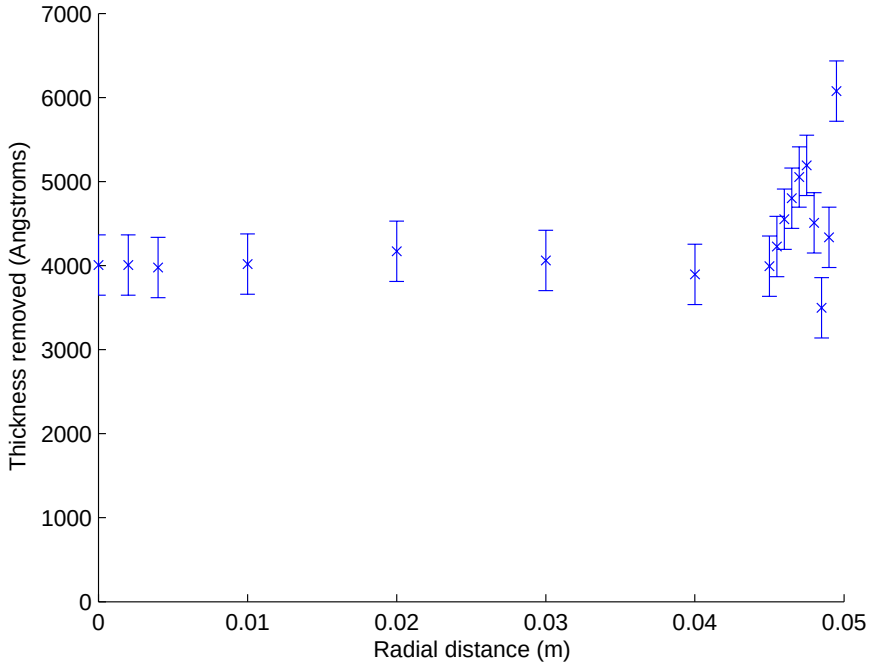

Figure 3.8: Typical material removal profile for silicon oxide polishing

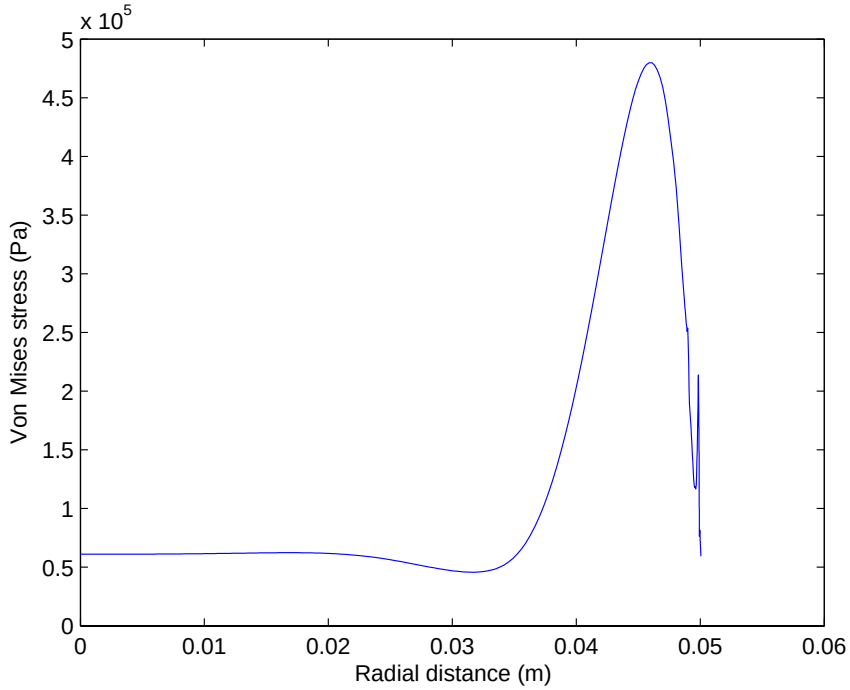

Figure 3.9: Von Mises stress profile for a 100 mm wafer (50 kPa)

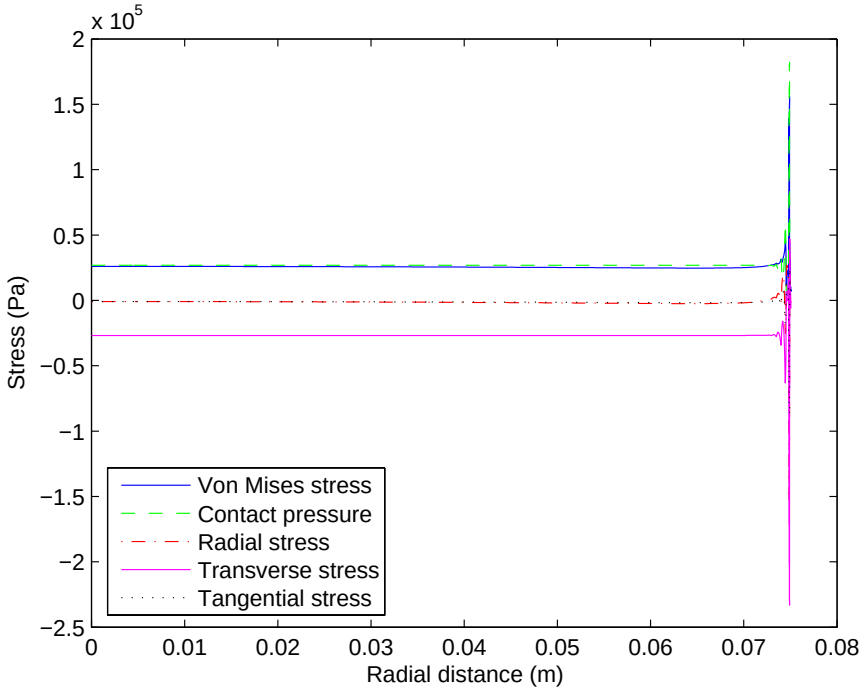

(a) Film stresses and contact pressure

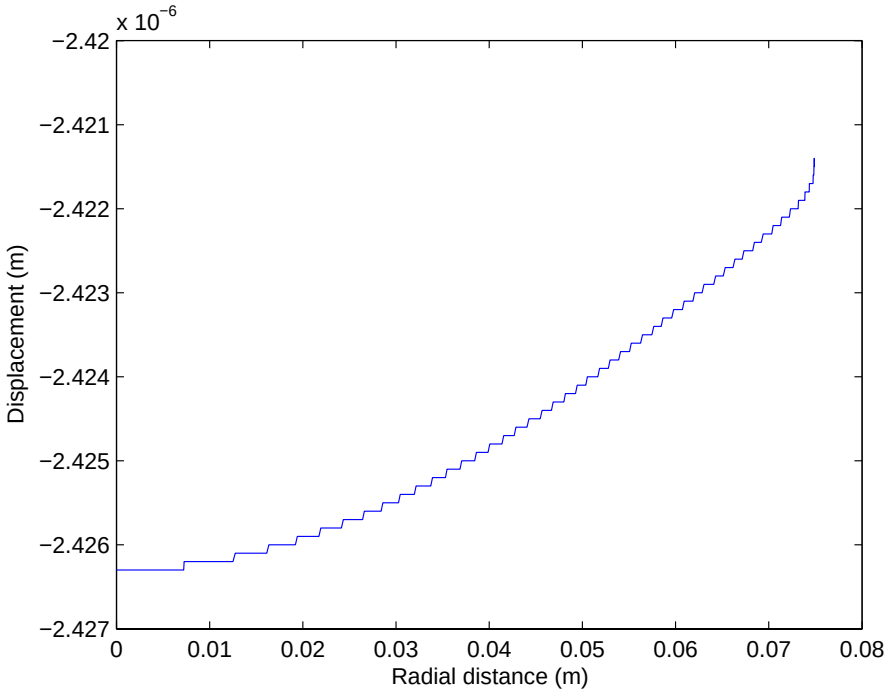

(b) Wafer profile

Figure 3.10: FEM results with rigid carrier film

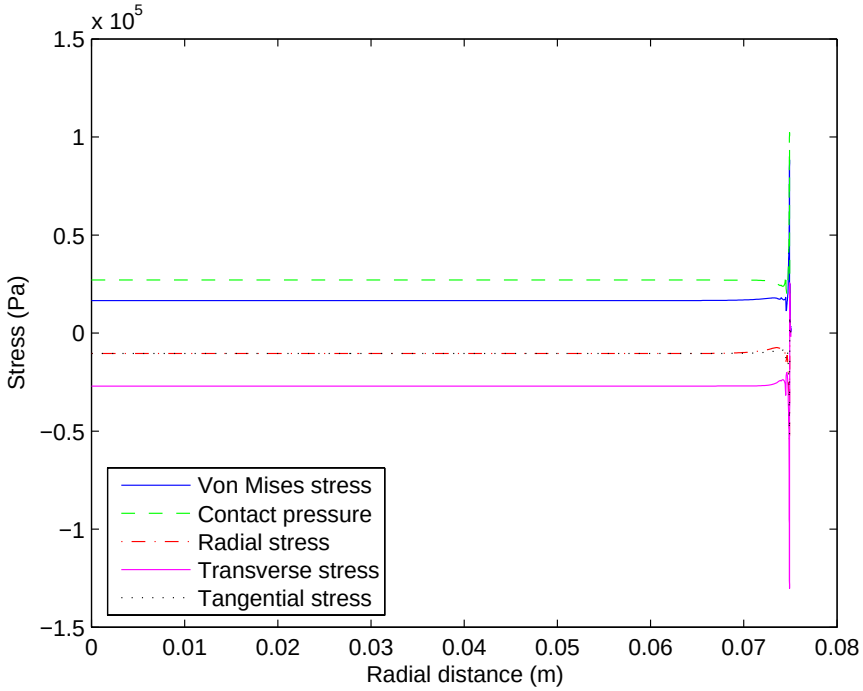

(a) Film stresses and contact pressure

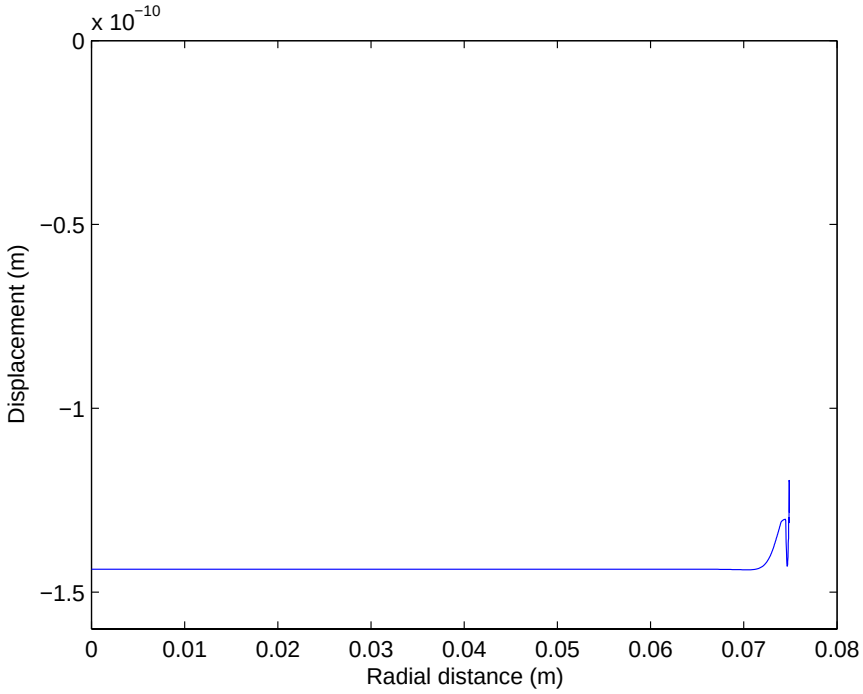

(b) Wafer profile

Figure 3.11: FEM results with rigid pad

carrier film to accommodate the eight capacitive sensors. The accuracy of the entire system is $\pm 1\ \mu m$.

A 150 mm diameter, 680 μm thick, p-type, silicon wafer is used in the experiments. The top surface of the wafer contains a 1 μm thick layer of metal (copper or aluminum) deposited by a DC sputtering process. This metal film serves as the target surface for the capacitive sensors. In a control test, the stainless steel wafer carrier is verified to exhibit no noticeable deflection which could affect the results. Other control tests include loading the wafer carrier against a granite flat and against the base of the fixture. Results show flat profiles indicating the good integrity of the setup.

Finally, the compression setup of Figure 3.12 is used to carry out the actual wafer bending tests. The wafer carrier is loaded in steps of 44.6 N (10 lbs) up to 446 N (100 lbs), the loads typically used in CMP. Compression tests are carried out on a Rodel IC1000 pad. The results are shown in Figure 3.13. Each data point represents the average of 8 repetitions of the test and each error bar represents one standard deviation. This error includes both the repeatability and system error. The wafer was rotated 45 degrees in each of the repetition. There is no significant wafer bowing as a result of the loads considering the error in the tests.

3.4 Concluding Remarks

Finite element analysis shows that the contact pressure distribution between the wafer and the pad is essentially uniform except at the edge of the contact where there is some nonuniformity and a peak contact pressure. This happens at most a couple of millimeters from the edge of the wafer. However, when the size of the contact area is approaching the thickness of the elastic medium (the pad), the

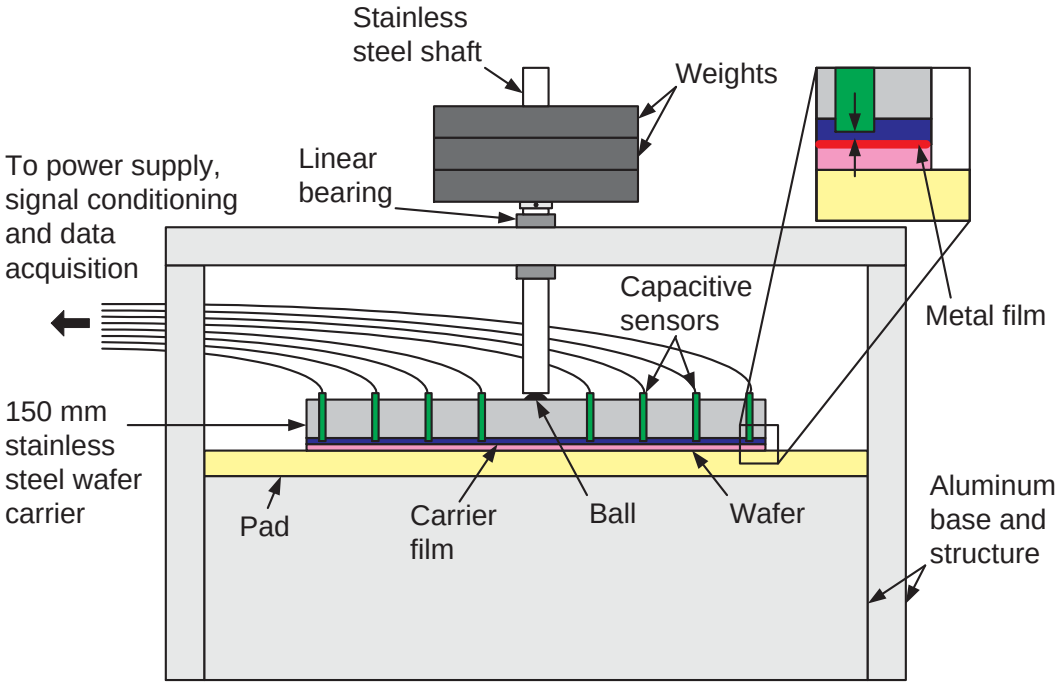

Figure 3.12: Static wafer deflection setup

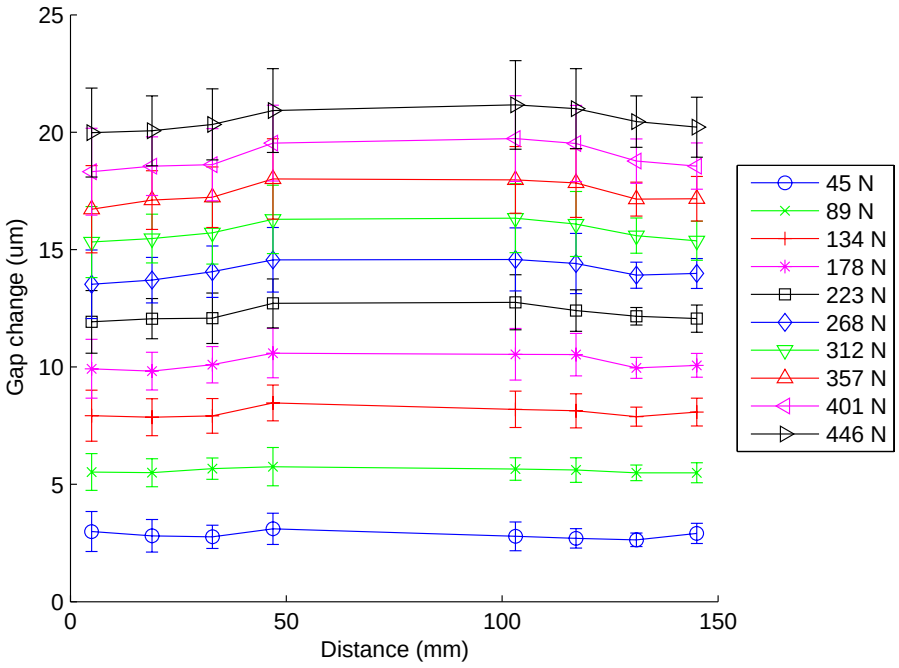

Figure 3.13: Static wafer deflection result

solution approaches that of a rigid punch indenting on a semi-infinite elastic flat: a power law-like pressure profile. The slight bending of the wafer close to the edge due to the peak contact pressure causes a ring of high von Mises stress 4 mm from the edge of the wafer. This peak von Mises stress is the result of tensile radial and tangential stresses at that location due to the bending of the wafer. The location of these stresses, 4 mm from the edge of the wafer, is close to the observed peak removal seen in the polishing of silicon oxide films suggesting the role of film stress. Studies have shown that film stress plays an important role in affecting water molecule penetration into the silicon oxide network. Wafers with tensile stresses tend to give higher removal rates than wafers with compressive stresses.

The deformed wafer profile from FEM showed the wafer bending by less than 1 μm, close to the edge of the wafer. Experimental static compression tests on a 150 mm wafer with loads from 44.6 to 446 N did not show significant bending of the wafer outside the accuracy of the system. This shows that the increasing load and peak pressures at the edge do not affect the curvature of the wafer significantly.

CHAPTER 4

EXPERIMENTS

This chapter describes the experiments. The polishing pad plays an important role in the CMP process. It transmits the applied load and kinetic energy of its rotation to the wafer resulting in the contact pressures and relative motion necessary for material removal. It also serves as a conveyor to entrain fresh slurry into the wafer-pad interface and to transport used slurry away from the interface. The microstructure and properties of the very top layer of the pad is especially important for the polishing since it is in direct contact with the slurry and wafer. Hence, characterization and understanding of the pad is important. Pad soaking experiments are conducted to understand the extent of water penetration into the pad. Scanning electron microscopy reveals the porosity and interconnectivity of the pad. Surface profilometry on the pad is conducted to understand the surface height distribution. The distribution of fluid pressure at the wafer-pad interface is important in CMP since it is coupled with the contact pressure distribution. The contact pressure distribution, in turn, is directly related to the material removal distribution. Two-dimensional pressure mapping is conducted to measure the distribution of fluid pressure at the wafer-pad interface. Since the wafer carrier used in this research is a gimbaled design, it has the freedom to tilt with respect to the pad. Tilting of the wafer carrier will affect the film thickness distribution at the wafer-pad interface. This will affect the fluid pressure distribution. The wafer carrier tilt is measured using a capacitive sensing technique. In addition, tilt and wafer bending experiments

are also conducted to correlate to the actual situation involving the carrier film and the wafer.

4.1 Polyurethane Pad

Polyurethane is commonly used in making polishing pads due to its good wear properties and manufacturability. The density and stiffness can be varied easily by producing it into a foam with voids in the matrix. One of the most widely used polyurethane polishing pads is the Rohm and Haas (formally Rodel) IC1000. This pad is available commercially and is often used and studied. Hence, this pad will be chosen for use in this research. The pad is made of a microcellular polyurethane material containing randomly distributed pores or voids. It is manufactured by the mixing of a urethane polymer, and pore forming and curing agents. This mixture is poured into a mold and allowed to cure before the "cake" is taken out and sliced into individual pads [3]. The manufacturing process is shown in Figure 4.1. The voids that form in a given pad are spherical with diameters in the range of 30 to 50 μm and these voids comprise about 30-35 percent of the total volume of the pad (see Figure 4.2). The structure is "closed-cell" meaning no interconnectivity of the voids. However, a small degree of interconnectivity can be seen as shown in Figure 4.3.

Industry practice dictates that the polishing pad be soaked in de-ionized water for a certain period before mounting it onto a polishing machine. The pad is then "conditioned" in order to achieve a constant surface roughness, and a "pad break-in" is conducted before proceeding to use the pad on actual wafers. The effect of soaking time on the dynamic shear modulus, G', of the pad has been studied by some researchers [70]. It was found that the dynamic shear modulus of the pad decreased with soaking time. The proposed explanation is a weakening of the

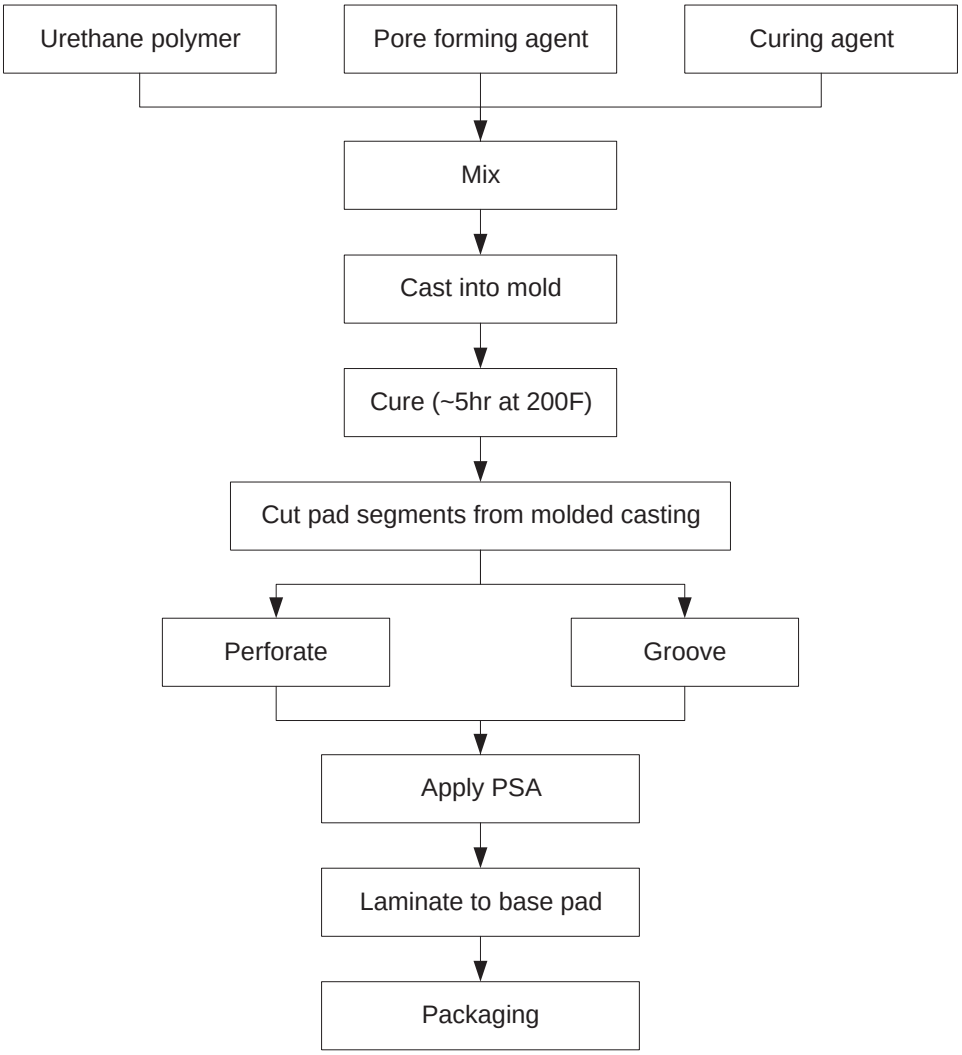

Figure 4.1: Manufacturing process flow for IC1000 pad

polymer structure by the water, therefore, making the pad softer. The Shore D hardness of the IC1000 pad has also been measured before and after a soak in which the pH was controlled [71]. Compared to a pad that was not soaked, there was a decrease in hardness after the pad was soaked in water for 24 hours. The decrease in hardness was greater as the pH of the solution increased.

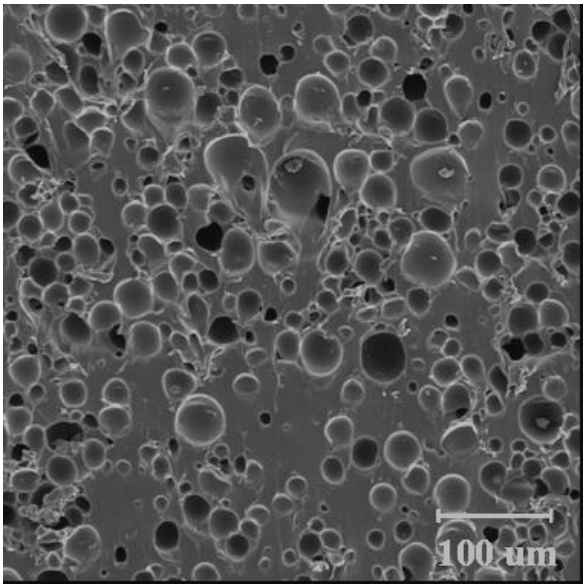

Figure 4.2: Scanning electron-micrograph of as-delivered IC1000 pad

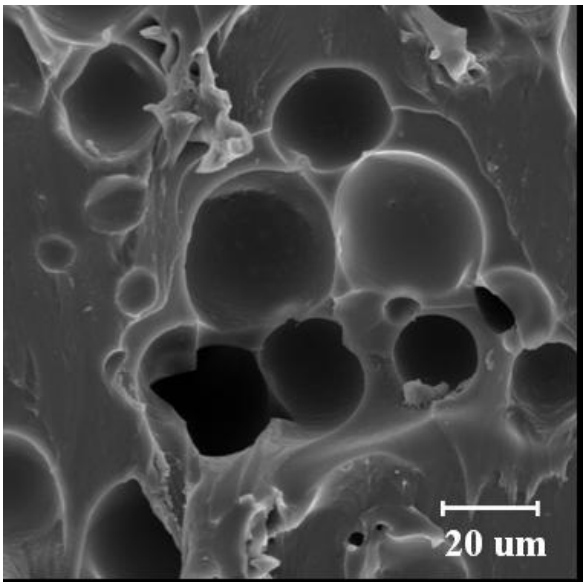

Figure 4.3: Scanning electron-micrograph of IC1000 pad showing interconnectivity of voids

4.1.1 Pad soaking.

In order to find the speed and extent to which water penetrates the voids, pad soaking experiments were conducted. IC1000 pads were used for all the experiments. In the first experiment, coupons were cut from an IC1000 pad. The size of each coupon was 4 x 4 cm with an average thickness of 1.3 mm. These coupons were stripped of the adhesive backing so water could be absorbed from all sides of the coupons. They were also observed under the microscope to ensure that there was no adhesive residue left. Then, the coupons were soaked in the same beaker of water with spacers to separate the coupons and prevent them from sticking together, sticking to the wall of the beaker, or lying flat on the surface of the water. Each time the coupons were taken out of the beaker, they were patted lightly on all sides with a lint free cloth to remove any excess water and also for consistency before weighing. The weighing was performed on a Mettler Toledo AB 104 analytical balance that has a resolution of 0.1 mg and an error of 1 mg. The experiment was run for more than three weeks, with more readings taken during the first day of soaking when the water absorption rate was the highest. Altogether, three sets of experiments were done.

Figure 4.4 shows the result from pad coupons of the same size. The graph shows the percentage increase in pad weight with respect to its dry weight plotted against time. There is a sharp increase in the pad weight during the first 50 hours of soaking. The pad weight then reaches a steady state, at around 100 hours, and does not show any apparent increase towards the end of the experiment (around 500 hours of soaking). The coupons did not change in dimensions before and after soaking when measured with a micrometer screw gauge and vernier callipers.

In the second experiment, coupons of different sizes were used and a soaking experiment was conducted in the same manner as the first experiment. Table 4.1 shows the breakdown of the sizes of coupons used for the experiment.

Figure 4.5 shows the result for the soaking of different size pads. Similar to Figure 4.4, there is a sharp increase in pad weight for the first few hours of soaking before stabilizing at around 100 hours. Except for the 10 x 10 mm size pad coupon, all other coupons had an equilibrium weight increase of 4-4.5 percent. Figure 4.6 shows the weight increase of the coupons of different sizes (after $\approx$ 240 hours of soaking) compared to their volume and surface area. The volume, surface area and weight increases were normalized to the 10 x 10 mm size. Comparing all three trends, it is very clear that the pad's weight increase correlates better to its surface area than its volume. This suggests that the water absorption is limited to the outer layer of the pad.

Assuming that polyurethane is impermeable and that water only gets absorbed by filling up the voids in the pad, the percentage volume of water-filled voids with respect to the pad volume can be calculated as

$$\text{Percentage volume} = \frac{100 \text{ x Mass of water absorbed}}{\text{Density of water x Volume of pad}} \tag{4.1}$$

The value obtained is 3.4 percent which is much lower than the 35 percent void volume of the pad, which means that only a fraction of the voids in the pad are filled with water. This is due to the impermeability of the pad and the fact that the voids are "closed-cell," indicating little or no interconnection between voids. Using a percentage void volume of 35 percent for the pad, this corresponds to a penetration of water to 59 μm or 1.5 "void layers" of the pad.

Further confirmation of the water penetration was obtained by soaking the pad material in black ink for more than a week. The coupons were then dried before cutting to expose the cross sections. The cross sections were observed under an optical microscope. Figures 4.7 and 4.8 show optical micrographs at low and high magnifications and reveal a penetration depth of about 60 μm which is very close to the calculated value of 59 μm from the water soaking experiment. Even though the IC1000 is classified as a "closed-cell" material, there is a certain degree of void interconnectivity as shown in Figure 4.3. It was also observed that the voids were interconnected between layers. These results suggest that water gets absorbed in the topmost layers of the pad and may alter its properties. The mechanism for the water penetration could be a process whereby some of the air in the voids first dissolves into the water. The dissolved air then diffuses to the bulk of the water. This process repeats itself over and over again until the voids are completely filled with water.

In conclusion, pad soaking is an important preparation procedure that has to be carried out in order to obtain consistent results. The impermeability of the pad indicates that large scale water diffusion of slurry through the thickness of the IC1000 pad is not possible. Only a small amount of water is diffused into the polyurethane material to alter its characteristics. The results showed that water penetrated and filled up the top layer of the voids completely when pad soaking is practised as in the industry. Further conditioning, pad break in and polishing may accelerate the penetration of water into the voids.

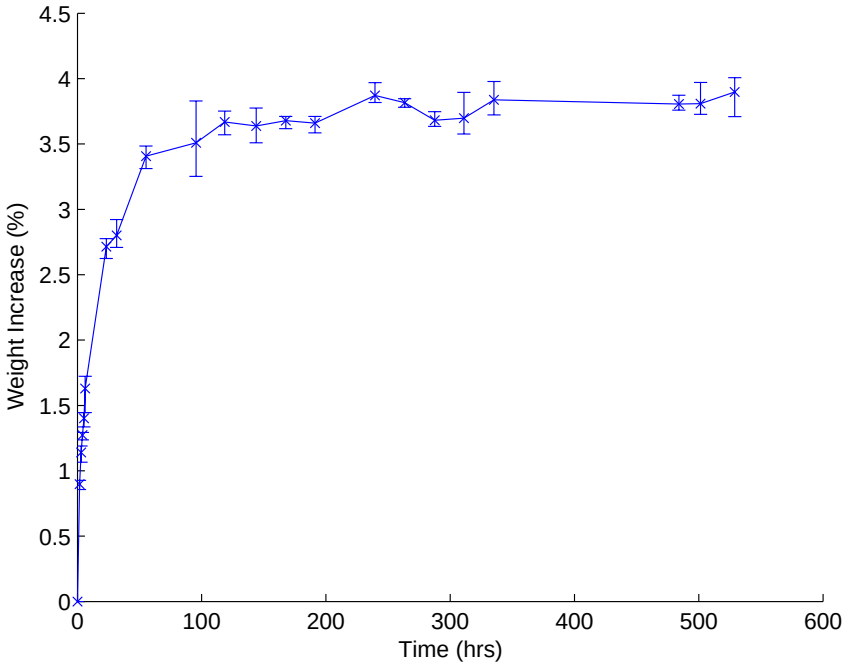

Figure 4.4: Weight increase (percent) versus soaking time (hrs) for IC1000 pad

Table 4.1: Dimensions of coupons used for the soaking of different size pads

Dimensions	Average Dry Weight (mg)
10 x 10 x 0.83 mm	66
20 x 20 x 0.83 mm	261
30 x 30 x 0.83 mm	605
40 x 40 x 0.83 mm	1050
50 x 50 x 0.83 mm	1660

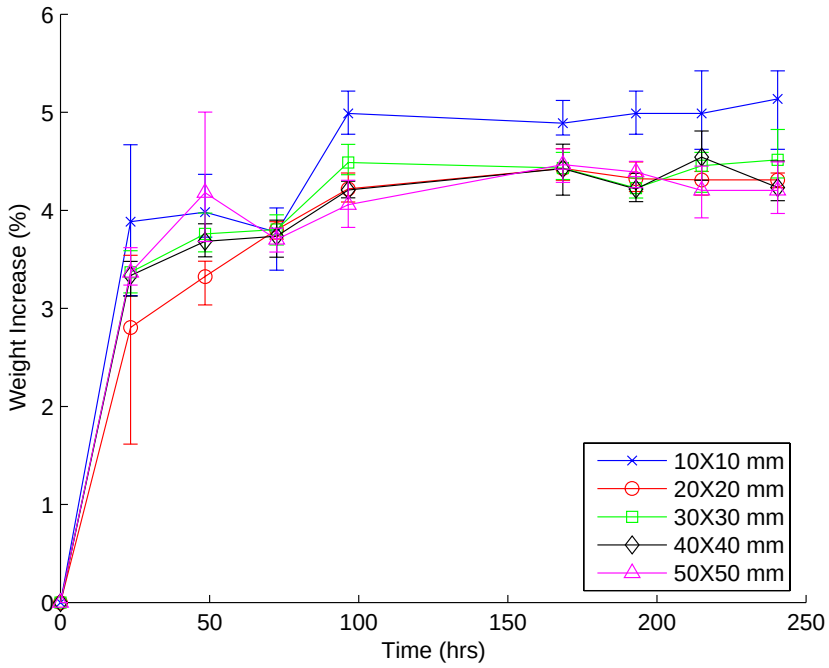

Figure 4.5: Weight increase (percent) versus soaking time (hrs) for different size pads

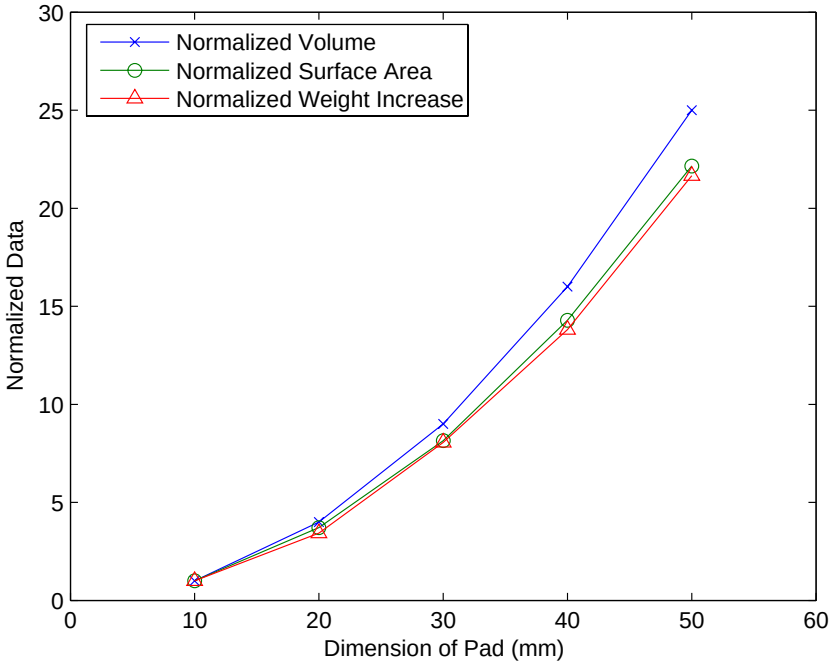

Figure 4.6: Comparison of normalized weight increase with volume and dimension of different size pads

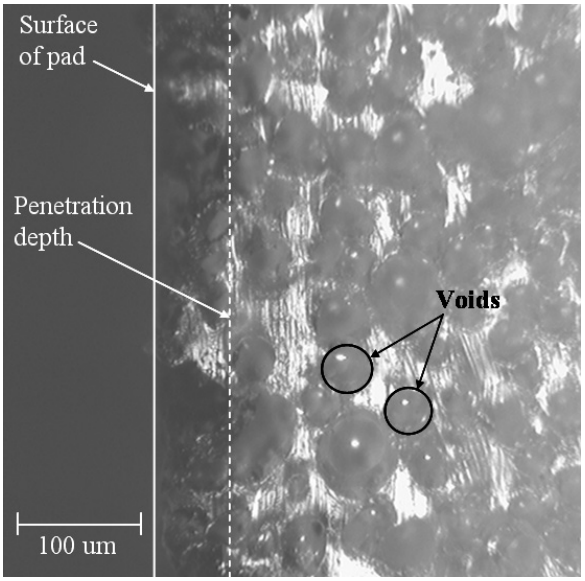

Figure 4.7: Low magnification optical micrograph of a cross-sectional view of pad soaked in black ink

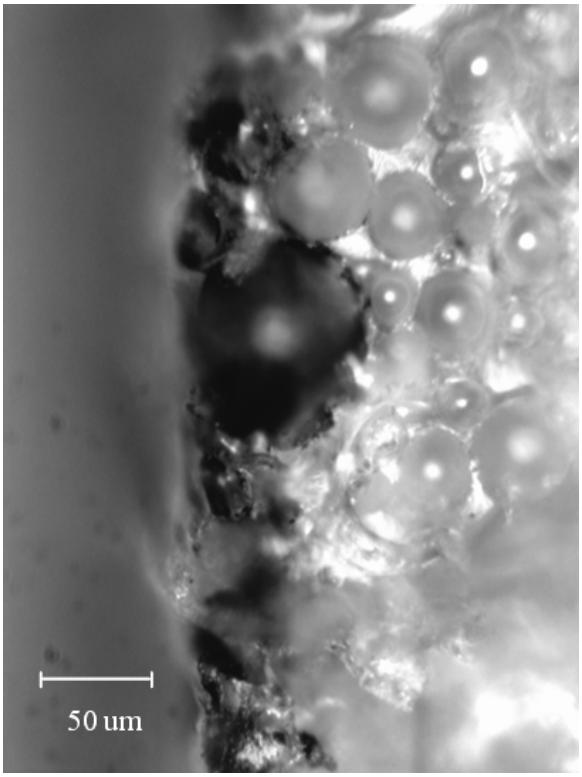

Figure 4.8: High magnification optical micrograph of a cross-sectional view of pad soaked in black ink

4.1.2 Pad surface height.

Non-contact, scanning, white light interferometry is used to obtain surface height data of an as-received polishing pad and a pad that has been conditioned with a diamond grit conditioner. Figure 4.9 shows the histograms of surface heights for both pads. The as-received pad has a negative skew while the distribution of the conditioned pad is essentially Gaussian. The skewness for the as-received pad is about -2 while that of the conditioned pad is approximately zero (i.e., -0.002).

Typical one-dimensional profiles of the pad surfaces are shown in Figure 4.10. It can be seen that the as-received pad has a higher number of "flat" asperities while the conditioned pad shows a Gaussian-like profile with sharper peaks. The reason for the difference is clearly shown in Figure 4.2 where the pad surface is magnified by scanning electron microscopy. The polishing pad is made of polyurethane impregnated with "micro-voids." The material between the voids is flat due to the manufacturing process where the pad is sliced from a "casting." It is this flat region that contributes to the "flat" asperities in the one-dimensional surface profile of the as-received pad. This leads to more "counts" at higher surface heights and gives rise to the negative skew in the histogram. The conditioning process which actually uses a flat disk impregnated with diamond particles to abrade the pad, alters the surface characteristics of the pad (as can be seen in Figure 4.11) and causes it to be Gaussian-like. The kurtosis for the as-received pad is approximately 7.5 indicating a high and narrow peak, while that of the conditioned pad is approximately 3.3 (a Gaussian distribution has a kurtosis of 3).

Interferometric data of conditioned IC1000 pads from Lawing [72] showed slightly different results. Based on his data, Borucki [73] modeled the surface height distribu-

tion as having an intrinsic exponential form at the left tail due to the foam structure. The right tail representing the top of the asperities is Gaussian determined by both the foam structure and the conditioning process.

The Peklenik number [74], γ is used to characterize the directional properties of a surface. It is defined by the ratio of x and y correlation lengths, that is

$$\gamma = \frac{\lambda_{0.5x}}{\lambda_{0.5y}} \tag{4.2}$$

where $\lambda_{0.5}$ is the length at which the autocorrelation profile of a function reduces to 50 percent of its initial value.

A conditioned pad was scanned in different directions with a profilometer in order to obtain the information for any directional property of the surface. Figure 4.12 shows the scanning procedure and the calculated Peklenik number for different scan angles. The average Peklenik number is approximately 1.1 and the asperities seem to have no preferred orientation. Figure 4.13 shows typical autocorrelation functions for a pair of profilometric scans. Based on the result, it can be assumed that the conditioned pad used in this study exhibits isotropic roughness with a Peklenik number of 1.

4.2 Pressure Mapping

A modified benchtop lapping machine (Struers RotoPol 35) is used for the fluid pressure mapping as shown in Figure 4.14. The apparatus incorporates a 300 mm diameter platen that varies in rotational speed from 40 to 600 rpm in 10 rpm increments. The platen is driven by a 1000 W DC motor. Load is applied pneumatically by a polishing head (Struers RotoForce 3), and spans from 30 to 400 N in 10 N

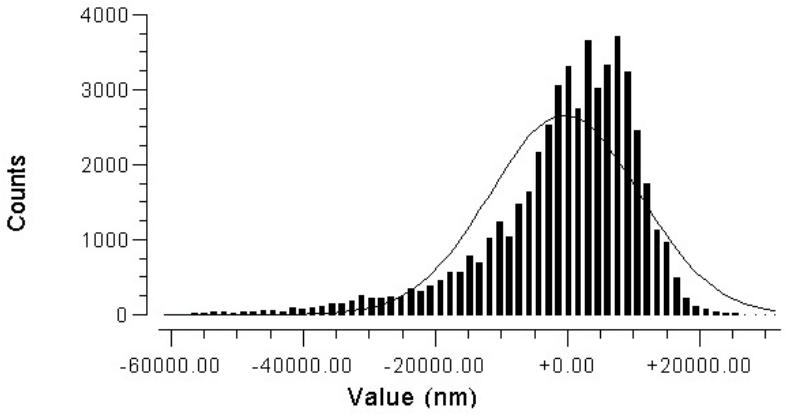

(a) As-received pad

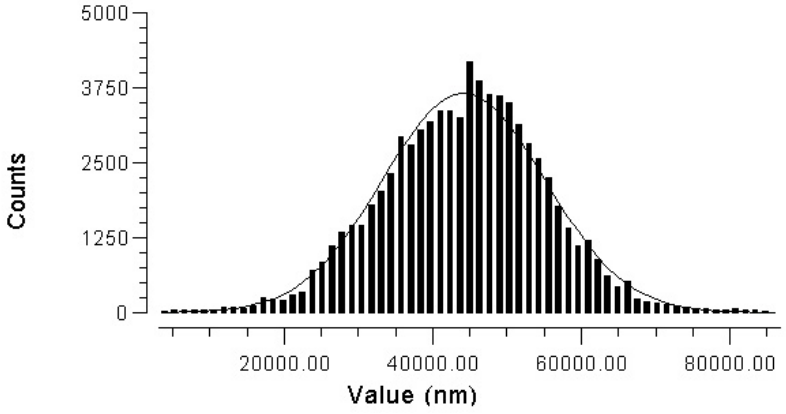

(b) Conditioned pad

Figure 4.9: Surface height distributions of pads

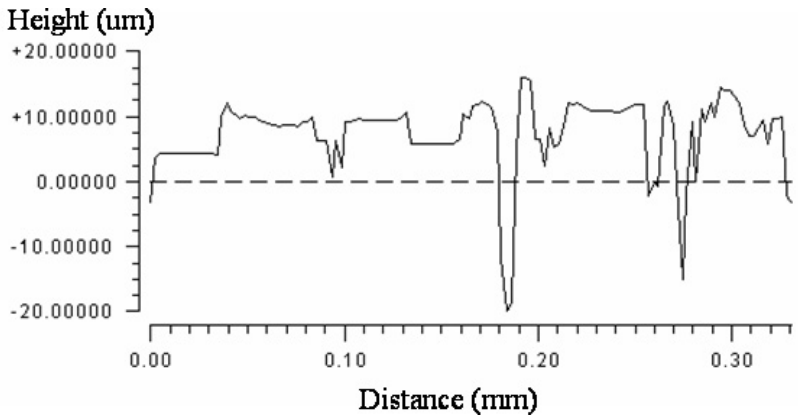

(a) As-received pad

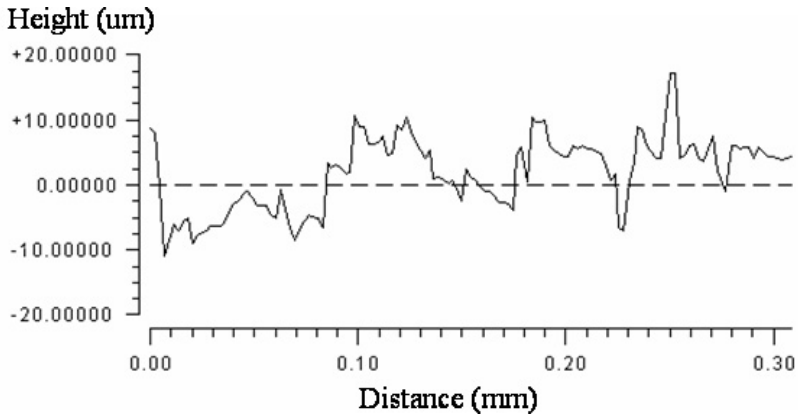

(b) Conditioned pad

Figure 4.10: One-dimensional surface profiles of pads

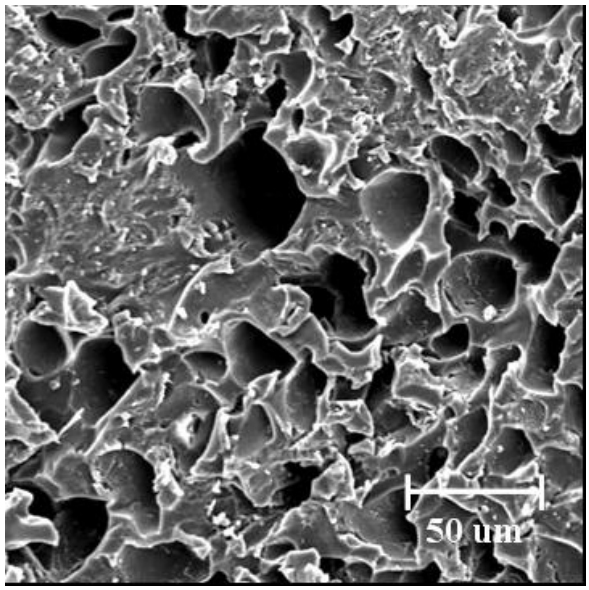

Figure 4.11: Electron-micrograph of conditioned IC1000 pad

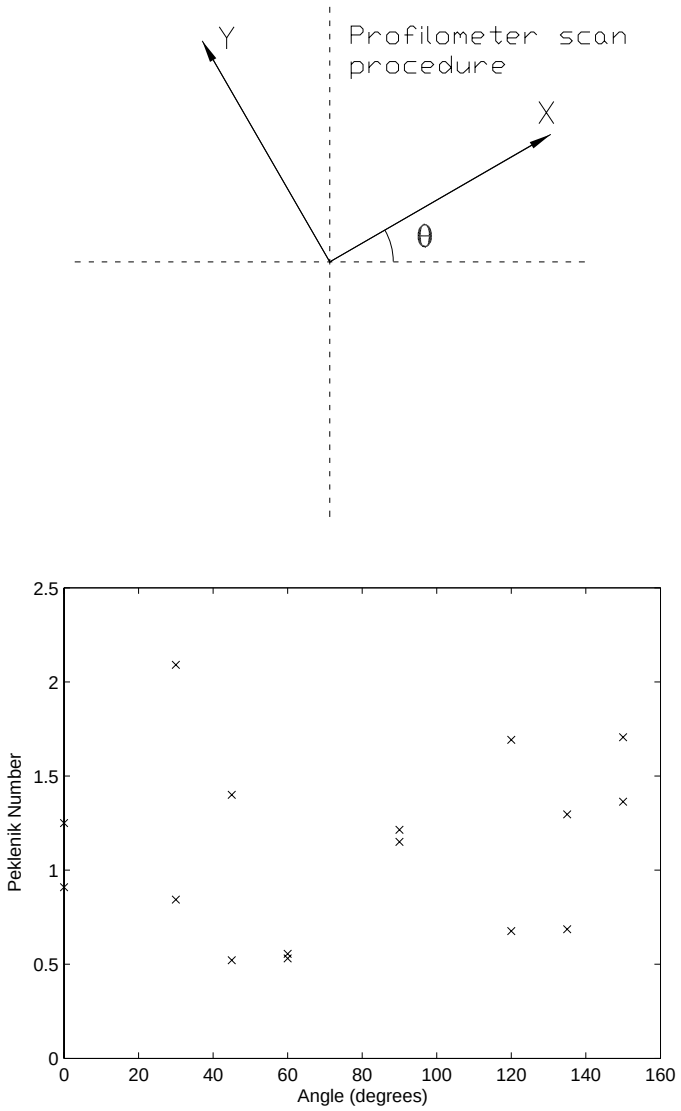

Figure 4.12: Scan procedure and Peklenik number of pad

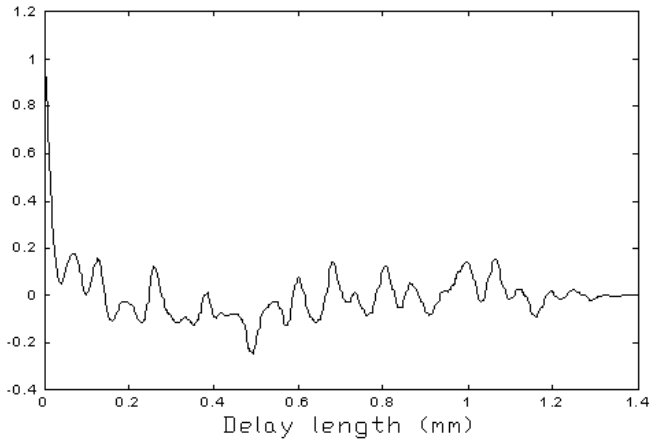

(a) Scan in x-direction

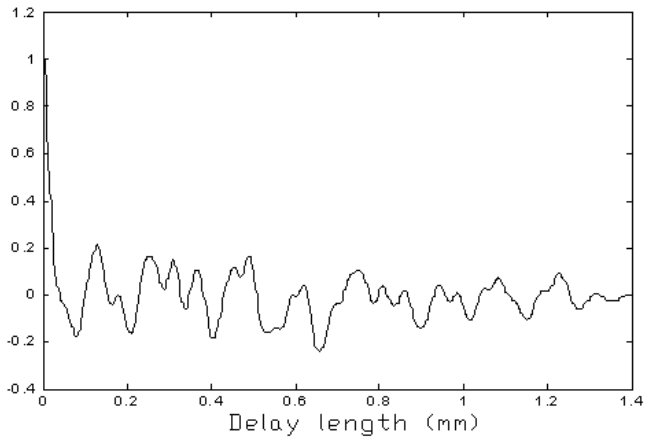

(b) Scan in y-direction

Figure 4.13: Autocorrelation functions from a pair of profilometric scans

increments. The polishing head is driven by an 80 W motor and has a fixed rotational speed of 150 rpm (rotating in the same direction as the pad). It is modified to prevent rotation of the pressure sampling disk during the pressure mapping experiments. The Rodel IC1000 polishing pad is adhered to the polishing platen by the pressure-sensitive adhesive that comes with it. The conditioning of the pad is done by sweeping a 100 mm diameter diamond-impregnated disk across the pad to get the pad to a consistent roughness. The conditioner is manufactured by Abrasive Technology, Inc. and has 160 um size diamond particles embedded on it. Water is used instead of slurry to prevent clogging of the sensors and polishing of the disk. This is delivered onto the rotating pad "upstream" of the disk so that the freshly deposited wafer/slurry can get entrained under the leading edge of the disk. Slurry can be delivered by a Masterflex HV-77200-60 L/S Easy-Load II peristaltic pump manufactured by Cole-Parmer Instrument Co. The pump rate can go from 0.06 to 2300 ml/min and it can accomodate different size tubings. Water can either be delivered by the peristaltic pump or by the water outlet of the Struers RotoPol 35. Water flow rate is adjusted so that a bow wave is formed at the periphery of the disk.

The fluid pressure at the disk/pad interface is measured with a stainless steel disk shown in Figure 4.15. The disk is 15 mm thick and 150 mm in diameter. The bottom surface of the disk has been lapped and polished to a flatness of about 1 μm and an average roughness of about 0.05 μm. Twenty membrane pressure sensors (Honeywell 26PCC) with a range of -103 to +103 kPa and a resolution of 0.1 kPa are mounted on top of the disk. The sensors have a response time of 1.0 ms and have a sensitivity of 6.67 mV/psi. The sensors are temperature compensated for a span from 0 to 50 °C and can be used to measure vacuum or positive pressure. It is also

ideal for wet applications. Vertical holes are drilled through the disk for sampling of pressure at the bottom face of the disk. The sensors are positioned such that there is a tangential row of sensors along a constant velocity line of the pad and a second row of sensors arranged in the radial direction. The pressure sensors provide signals to a National Instruments data acquisition system, and Labview software is used to collect the data. The 12 bit PCI-6071E National Instrument card can sample up to 32 differential channels simultaneously and has a maximum sampling rate of 1.25 MS/s per channel. The pressure sampling rate is normally set to 2 samples per second per sensor in the pressure mapping experiments. The disk is mounted onto the polishing head by a gimbal joint consisting of a stainless steel ball that allows the disk to pivot about the joint. It is through this joint that the load is applied.

The pressure measurements are made without rotation of the fixture. However, the fixture is rotated through increments of 60 ° after each set of pressure measurements. For each set, the speed is increased from 50 to 250 rpm in 50 rpm intervals and there is a dwell of 2 minutes for each speed. Pressure profiles for each speed is carried out by extracting the middle 30 seconds of the dwell and taking the average. In this way, 2D pressure maps for different speeds can be obtained. A total of 120 data points per condition is generated as shown in Figure 4.16. The pad is rotating counter-clockwise in the figure and this convention will be used. Figure 4.17 shows typical pressure profiles sampled along the tangential row of pressure sensors from leading to trailing edge for different parts of the dwell of 2 minutes. It can be seen that the data is fluctuating within a maximum range of about 6 kPa. There is no significant change in pressure profile throughout the 2 minutes.

Figure 4.18 shows the pressure mapping results for pad rotation speeds from 50 to 250 rpm in 50 rpm increments. The range of pad speeds is typical of an actual

CMP process. Changing the applied load does not have much effect on the fluid pressure. The plots are created using the surface plot function in Matlab. Using the same orientation as in Figure 4.16, the leading edge is situated at the top of each plot. Given that there are only 120 data points, the pressure results might not appear as smooth but trends in the data are easily seen. There is a large region of sub-ambient pressure that occupies about 70 percent of the area under the disk. The highest sub-ambient pressure is located near the leading edge and slightly toward the center of the pad. The magnitude of the sub-ambient pressure increases with pad speed, which is consistent with one-dimensional data from previous work. A small region of positive pressure can be seen at the trailing edge of the disk.

Typically, both positive and negative fluid pressures developed quickly within the first two seconds after the pad starts rotating. The positive pressure region is always present. When the trailing edge of the disk is pushed down manually, the positive pressure region is enhanced. This is seen by the movement of the negative-to-positive pressure transition point towards the leading edge, along the tangential row of pressure sensors as illustrated in Figure 4.19.

4.3 Wafer/Disk Tilt

A capacitive sensing technique was used to monitor the orientation of the disk. A spanning aluminium frame was built across the top of the polisher to support 3 miniature micrometer stages holding capacitive probes similiar to the ones used in the static wafer deflection experiment. The probes were positioned at three different locations as shown in Figure 4.20. The probes were offset from the top of the steel disk to the operating range using the micrometer stages; and the disk acts as the target for the sensors. The air gaps between the sensors and the disk at the 3

Figure 4.14: Polishing machine

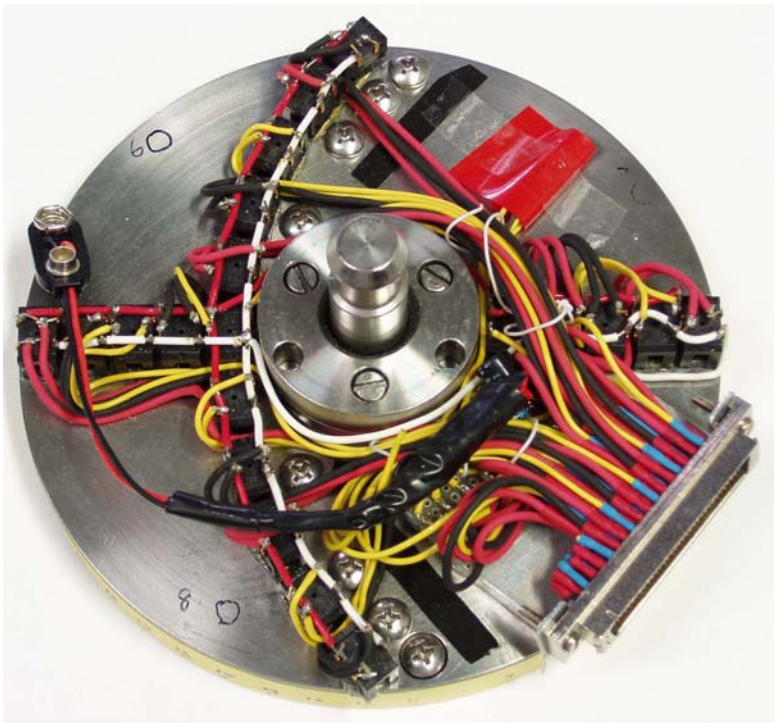

Figure 4.15: Pressure measurement disk

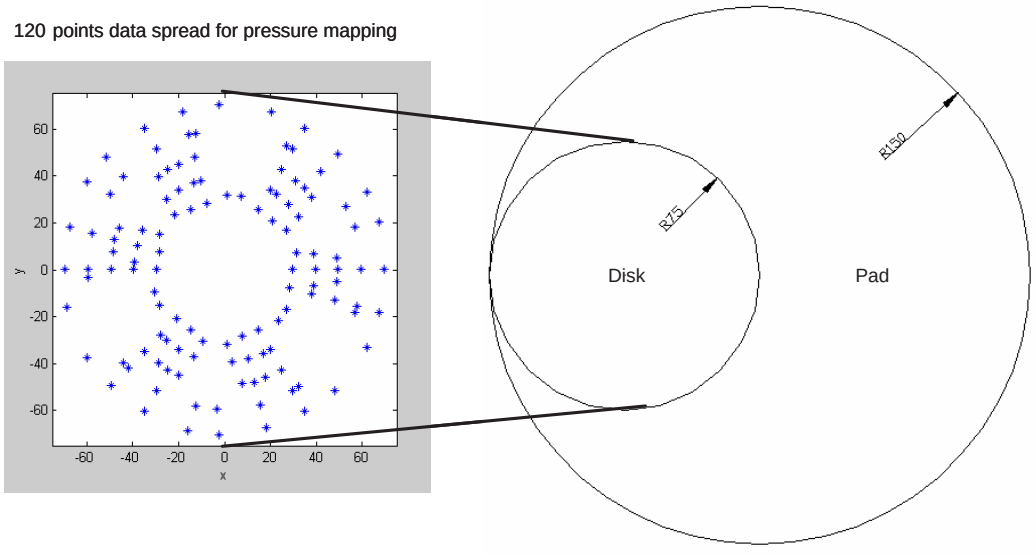

Figure 4.16: Experimental layout for pressure mapping

locations were monitored. There is no physical contact between the spanning frame and the polisher.

Before the pad was rotated, the air gaps were sampled at eight evenly spaced angular positions of the pad to average out the runout of the pad surface. Figure 4.21 shows a typical set of readout. All three curves are cyclic with Sensor 2 having a smaller amplitude since it is located closer to the center of the pad. Changes to the air gaps during the experimental runs were with respect to the mean value of static gap. Experiments were run for 30 N, 100 N, 200 N of loads for pad rotation speeds of 50 to 250 rpm in 50 rpm increments. The mean values of the fluctuations in gaps during the runs are used as input in further computations.

4.3.1 Orientation angles.

For a rigid body, 6 degrees of freedom are required to describe its motion and orientation in space, namely, the translations and moments in x, y, z axes (for cartesian coordinate systems). The disk in the setup is constrained in translations

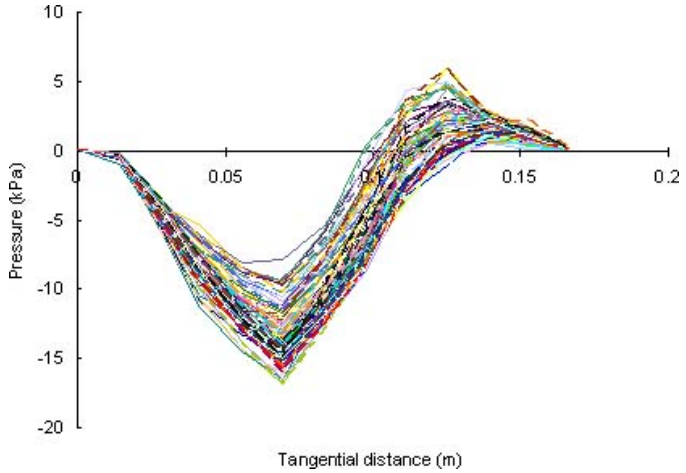

(a) 0 to 45 s

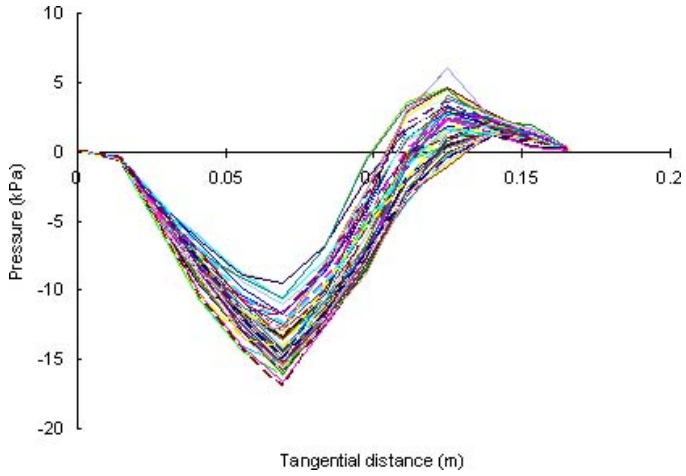

(b) 45 to 75 s

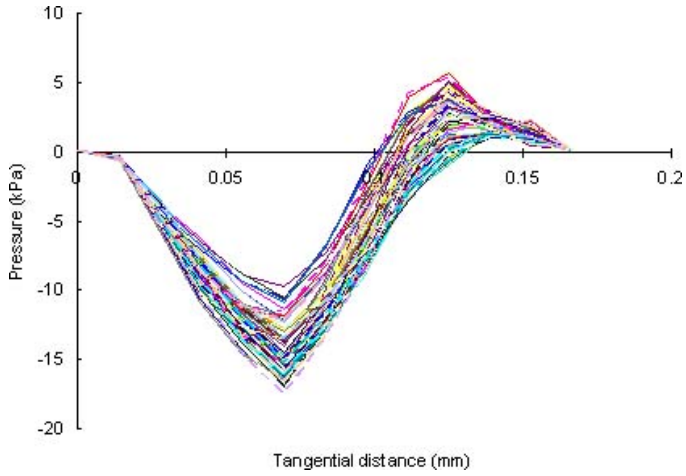

(c) 75 to 120 s

Figure 4.17: Tangential pressure profiles

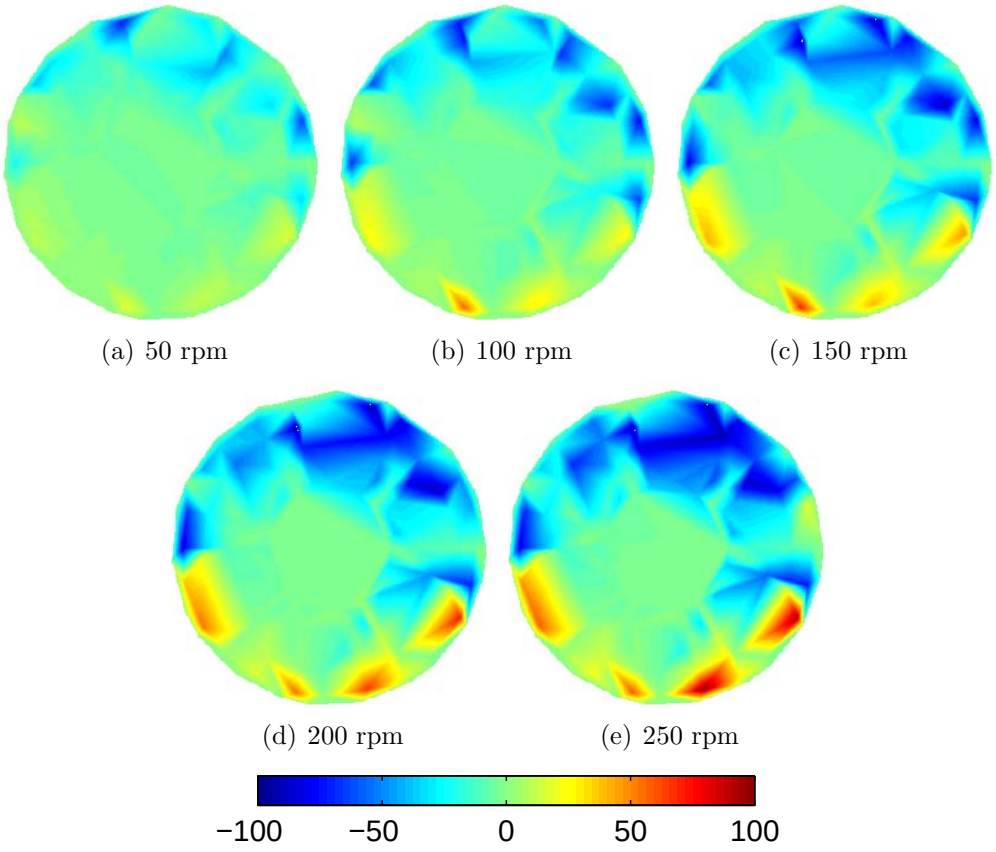

(a) 50 rpm (b) 100 rpm (c) 150 rpm

(d) 200 rpm (e) 250 rpm

Figure 4.18: Pressure maps from experiment (colorbar units in kPa)

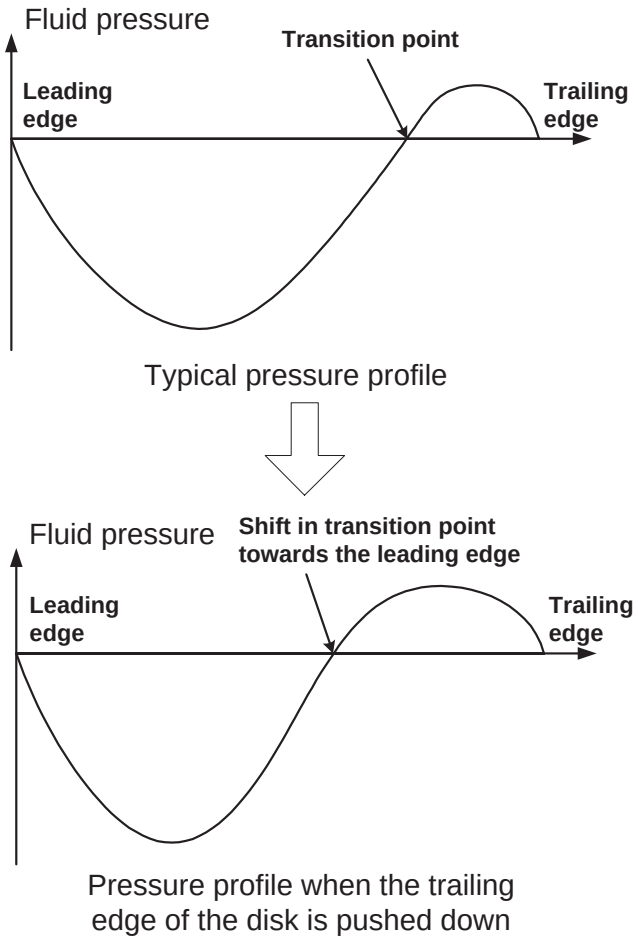

Figure 4.19: Shifting of the negative-to-positive pressure transition point

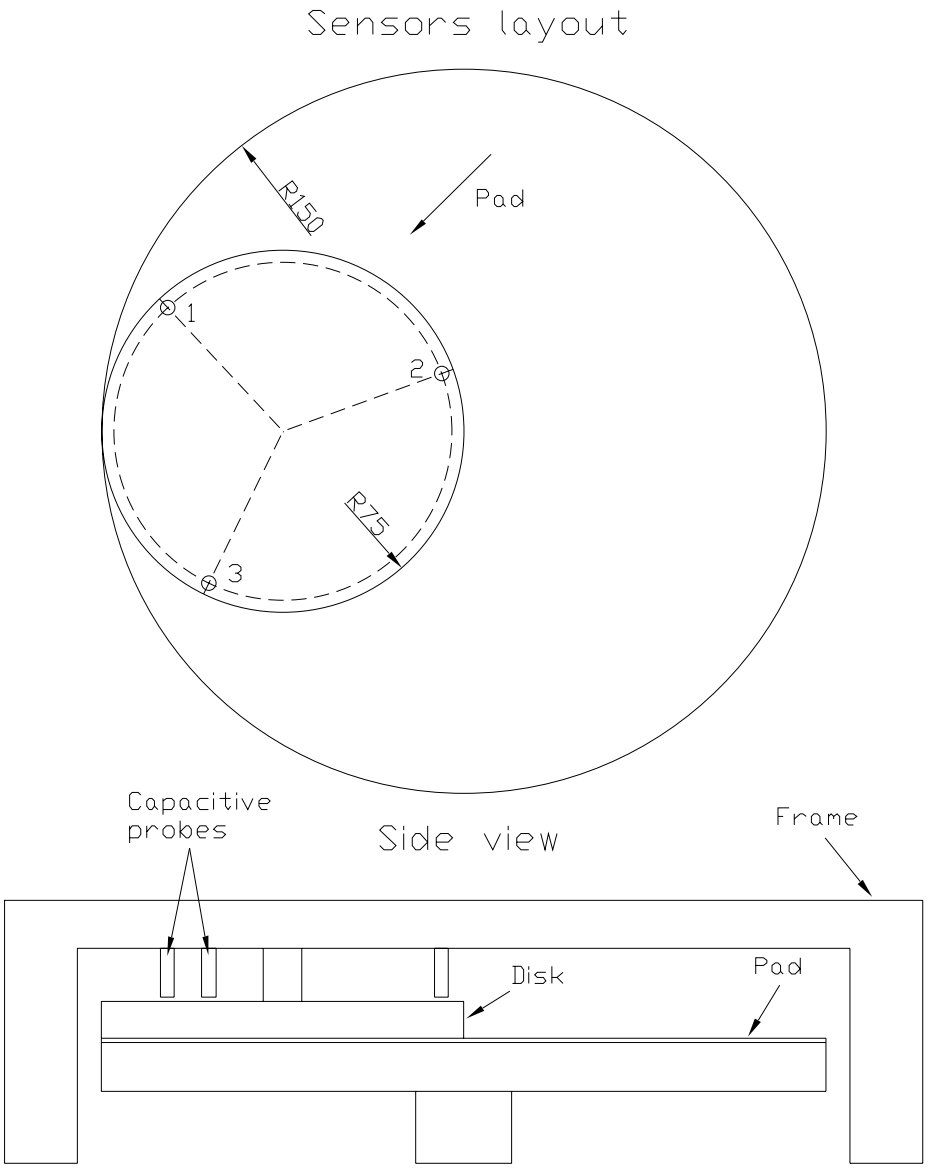

Figure 4.20: Sensors layout and side view of disk tilt setup

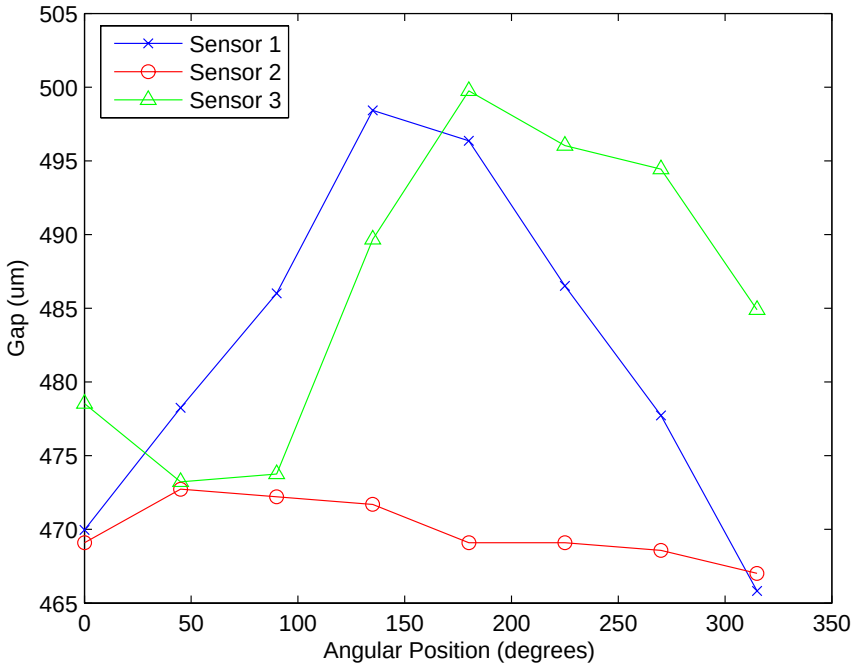

Figure 4.21: Static gap at 30 N

in the x and y directions and in rotation about the z-axis. That leaves 3 degrees of freedom and the orientation of the disk can be described by 3 parameters. Each set of data at the 3 capacitive probe positions can be computed to give two angles to describe the rotation of the disk and a third parameter, which is translation in the vertical direction. The convention used is shown in Figure 4.22. θ_a, the azimuth angle, locates the angular position of the lowest point of the disk (indicating tilt). ϕ, the tilt angle, describes the degree of tilt. The third parameter, d_z, is not shown but is the vertical displacement of the center of the bottom of the disk with respect to the static position. So, a positive value of d_z would mean the center of the bottom of the disk has moved vertically upwards away from the pad and vice versa.

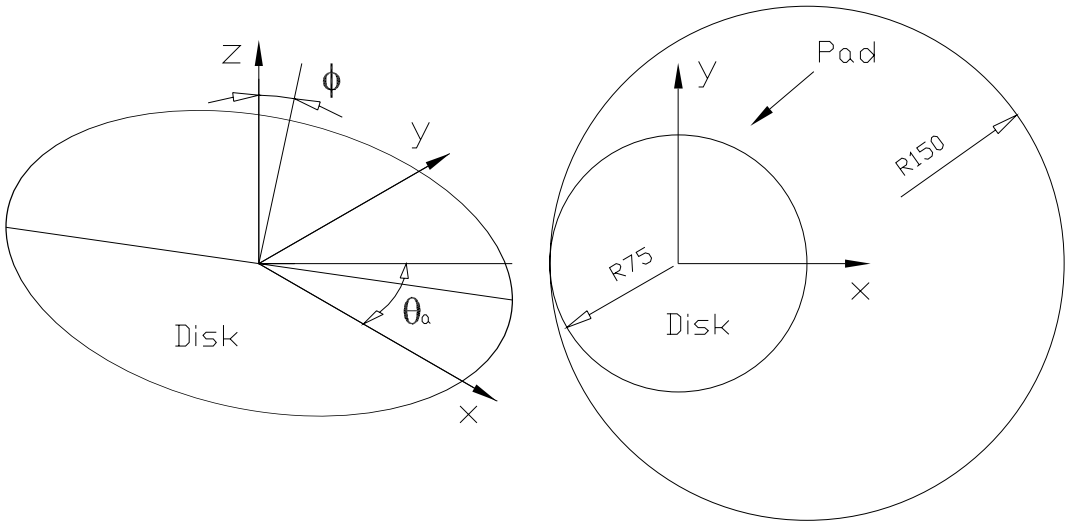

Figure 4.22: Definition of the tilt angles

4.3.2 Results.

Figure 4.23 shows a typical set of tilt data. The ordinate shows the displacement of the disk at the three sensor locations which is obtained through the change in air gap with respect to the static gap. The abscissa shows the pad speed. For all speeds, it can be seen that the disk at Sensor 1 and 3 locations has been moved upwards while at Sensor 2 location it has gone down. Sensor 3 location has the largest displacement magnitude while Sensor 2 location has the lowest magnitude. Referring back to Figure 4.20 for the locations of the sensors, this indicates that the disk is tilting towards the leading edge and towards the center of the pad. As speed increases, the amount of tilting seems to increase.

This tilt data is processed to give the azimuth angle, tilt angle and vertical displacement. Figure 4.24 shows the geometry of the tilted disk and the locations

of the three sensors. The unit normal vector of the tilted disk, U_n, can be computed from the vector product of V_{12} and V_{13}. The azimuth angle can be calculated from the x and y components of U_n. The scalar product of U_n and the global z vector will give the tilt angle. Setting the scalar product of the V_{10} and U_n to zero, the vertical displacement can be obtained.

The results for ϕ, θ_a and d_z for different combinations of speeds and loads are shown in Figure 4.25. The effect of pad rotation speed appears to be more dominant than the effect of applied load. This is consistent with previous pressure experiments [61] showing that load does not have much of an effect. As speed increases, θ_a decreases, ϕ and d_z increase. In other words, the disk starts off tilting down towards the leading edge and banking towards the center of the pad. As the pad picks up speed, it banks more and more towards the center of the pad and with the amount of tilt increasing. The center of the disk also gets lifted up.

4.4 Extending the Case to the Wafer Carrier

An attempt is made to extend the case to the actual CMP configuration. The pressure measurement fixture is a steel disk without a wafer. The basic CMP wafer carrier would also consist of a carrier film (or sometimes called the backing film) and a retaining ring. The carrier film is a thin (≈ 0.7 mm) piece of porous polymer attached to the bottom of the disk by pressure-sensitive adhesive. It serves to conform to the shape of the wafer and cushion it to prevent localized peak contact stresses. The carrier film used in the experiments is the Rohm and Haas DF200. Figure 4.26 shows an electron-micrograph of the carrier film. The retaining ring is usually a piece of ceramic consumable that surrounds the periphery of the wafer to prevent the wafer from sliding out from under the disk during polishing.

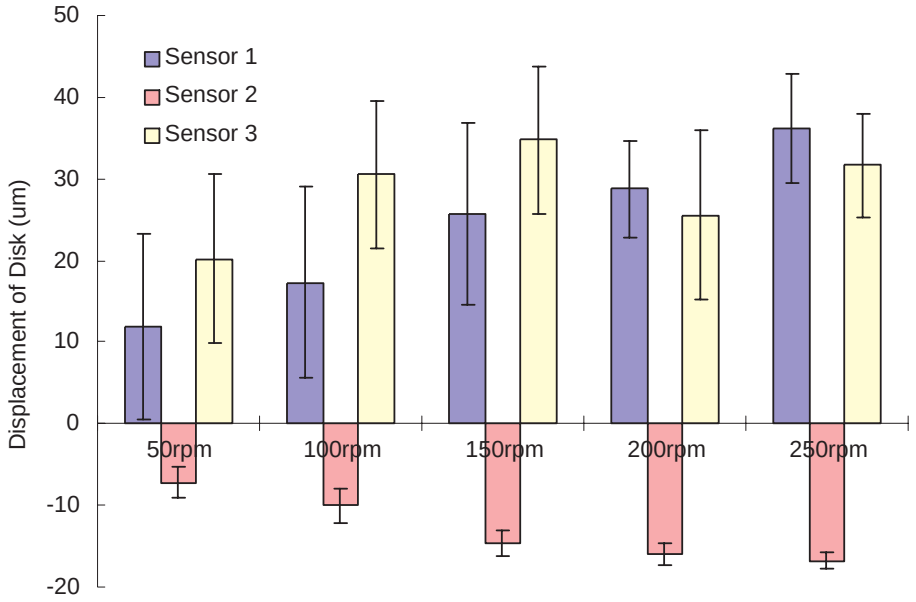

Figure 4.23: Tilt data at 30 N

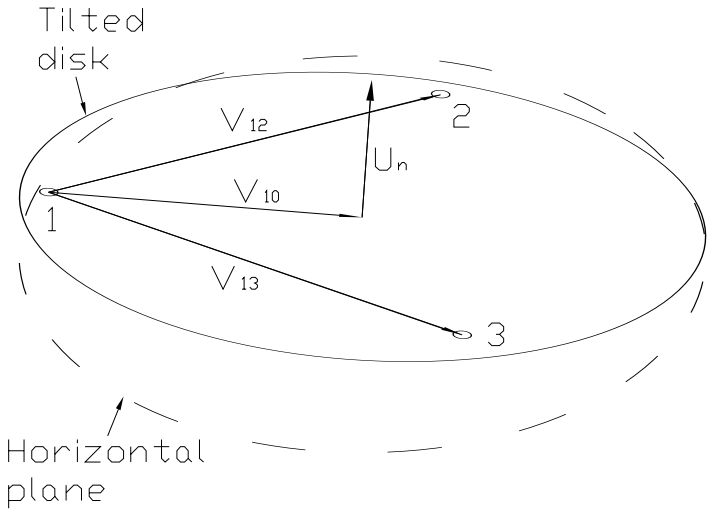

Figure 4.24: Tilt geometry

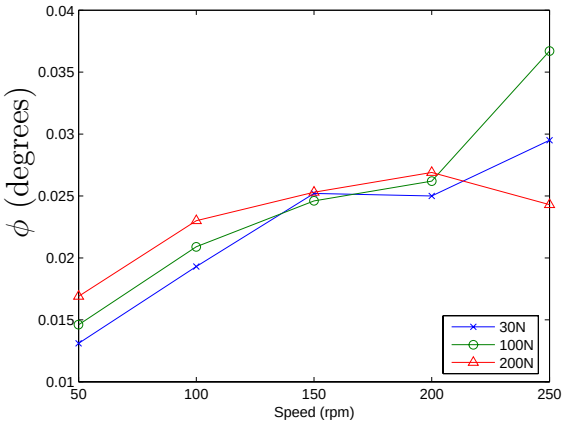

(a)

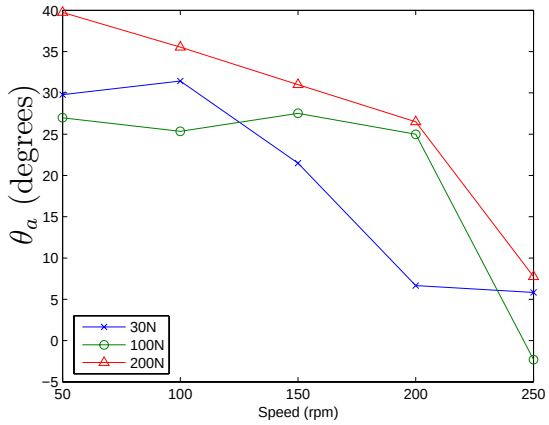

(b)

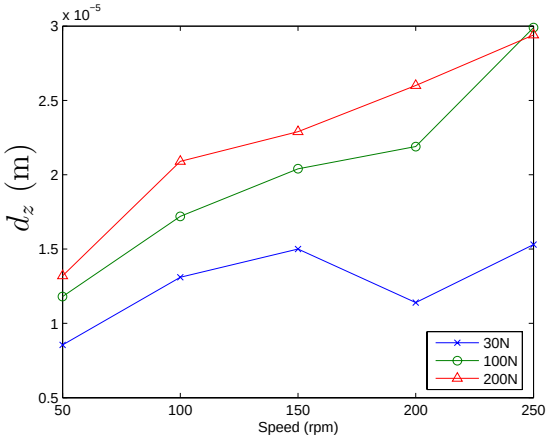

(c)

Figure 4.25: Speed and load effect on ϕ, θ_a, d_z

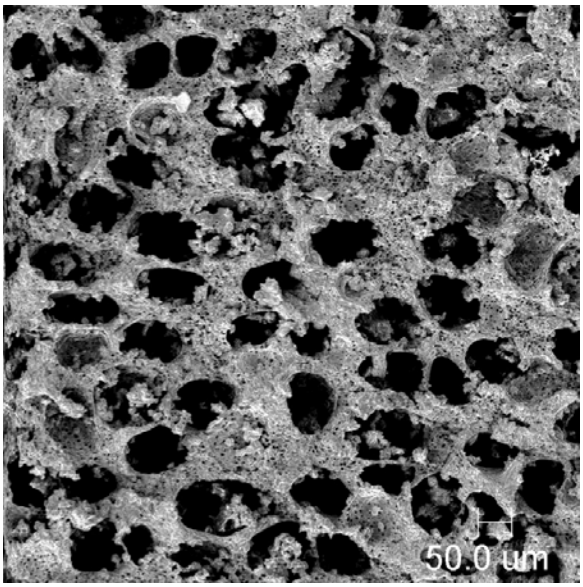

Figure 4.26: Electron-micrograph of DF200 carrier film

4.4.1 Wafer carrier tilt.

Attempts to measure the fluid pressure using the same technique proved to be a challenge due to difficulties in sealing and leakage through the porous carrier film. An indirect method is used to investigate the validity of the model by measuring the tilt of the wafer carrier with the wafer mounted. The same procedure as for the disk tilt experiments is used. The results on ϕ, θ_a and dz are shown in Figure 4.27.

It is clear from the graphs that the orientation of the wafer carrier is maintained (θ_a in the first quadrant) after adding the carrier film, retaining ring and wafer to the disk. Similar trends in ϕ, θ_a and dz are also observed.

The tilt results show that it is possible that the gap and fluid pressure are still maintained when the disk is switched to the wafer carrier. However, the results show only the orientation of the wafer carrier; the wafer might bend or tilt with respect to the wafer carrier, thereby, altering the gap. A second set of experiments is conducted to determine the shape and orientation of the wafer with respect to

the wafer carrier.

4.4.2 Wafer bending experiment.

One of the assumptions in the modeling of the fluid pressure is that the wafer is flat. This might not be true in the real situation since the wafer is flexible (especially for the larger wafers) and it is compressed between the soft carrier film and polishing pad. With the nominal fluid film thickness between the wafer and the polishing pad ranging from 10 to 30 μm, wafer shape change of a few microns will affect the results. Levert found out experimentally that suction is unlikely for wafers with an out-of-flatness greater than 8 μm [51].

The 150 mm wafer carrier used in the static wafer deflection experiment was used for this experiment. Eight holes were drilled and tapped along a diametric axis of the wafer carrier to hold eight capacitive sensors similar to the ones used in the wafer deflection measurement. The bottom surface of the wafer carrier was machined to within 2 μm flatness before a piece of carrier film was adhered to it. Prior to that, eight holes were punched through the carrier film to accommodate the eight capacitive sensors. A 150 mm diameter, 680 μm thick p-type silicon wafer was used in the experiments. The top surface of the wafer was covered with a 1 μm thick layer of metal (copper or aluminum) deposited by a DC sputtering process. This metal film was necessary to serve as the target surface for the capacitive sensors. As in usual CMP practice, a retaining ring was added to the wafer carrier to prevent the wafer from flying out from under the wafer carrier. In addition, a 10 μm thick polyethylene sheet was inserted between the carrier film and the wafer to prevent fluid from getting to the sensors. The capacitive sensors were recalibrated with the polyethylene film and the wafer target but the results showed no noticeable

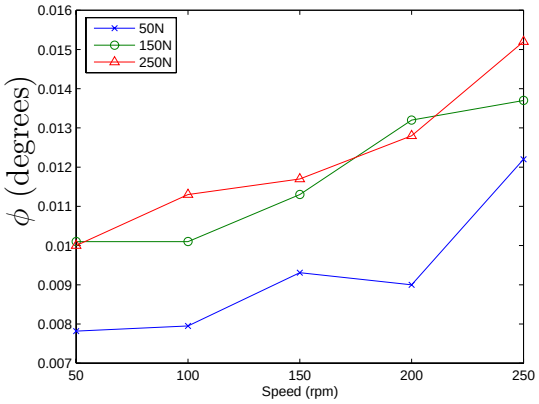

(a)

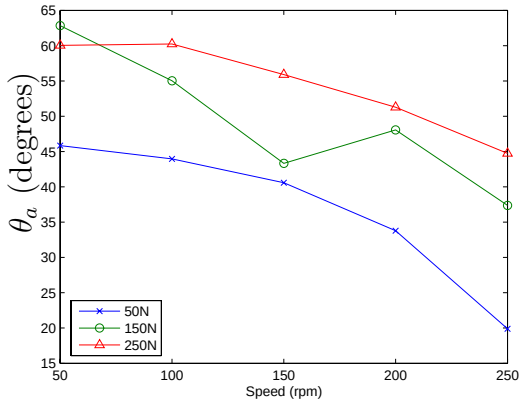

(b)

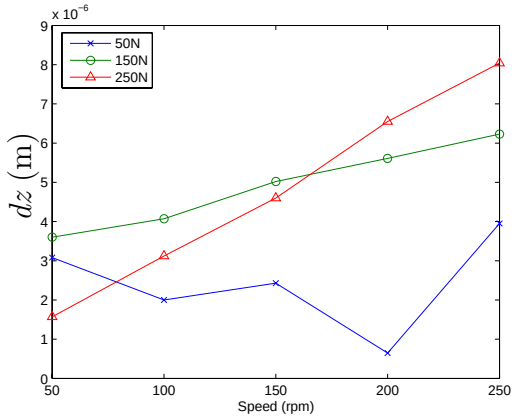

(c)

Figure 4.27: Speed and load effect on ϕ, θ_a, dz using wafer carrier

difference with calibration done without the polyethylene film. Details of the wafer carrier are shown in Figure 4.28.

The wafer carrier was prevented from rotating and load was applied to the wafer carrier, pressing it against the pad. Figure 4.29 shows two layouts for the experimental setup. The pad was rotating counter-clockwise and the capacitive sensors were aligned along a diametric axis. Both layouts were used for each condition to determine the displacement of the wafer with respect to the disk.

Dynamic experiments were conducted with different combinations of loads and platen speeds. The gaps between the sensors and the wafer were monitored. Changes in the gaps were taken with respect to the static gap. The static gap was the mean value of gap at different static angular positions of the pad for the purpose of eliminating any runout effect from the polisher. Figure 4.30 shows a typical set of results for the static gap. The static gap for each sensor was arbitrary set to within the linear operating range of the capacitive sensor. The fluctuations were small, averaging about 1 to 2 μm indicating that the gap was not much affect by the runout of the polisher.

The results from the experiments are shown in Figure 4.31. In the graphs for Layout 1 (L1), the leading edge of the wafer is at 0 mm distance while the trailing edge is at 150 mm distance. For Layout 2 (L2), the center of the pad is at 0 mm. There does not seem to be any wafer bending as seen from the graphs. Static wafer bending experiments (with normal loads up to 446 N) discussed earlier on have also indicated that the wafer bowing from center to edge is less than 2 um and the steel disk does not deflect under the loads. Here, wafer tilting with respect to the wafer carrier is detected. Displacement on the y-axis refers to the amount of compression of the carrier film or the decrease in gap separation. In all three cases, the leading

edge of the wafer is pressed more against the wafer carrier than the trailing edge (from Layout 1), and the wafer is pressed more against the wafer carrier close to the center of the pad (from Layout 2). The difference in carrier film compression between the leading and trailing edge regions is 5 to 7 μm, while for Layout 2 it is 1 to 2 μm. Except for a few data points, the error bars are about 1 to 2 μm (full range) indicating that the contact pressure across the wafer is quite constant during any run. There are no noticeable speed or load effects. The results suggest that the wafer is experiencing larger contact pressures at the leading edge, and at the inner edge close to the center of the pad.

It is possible to estimate the gap between wafer and the pad from the data gathered. The amount of tilt of the wafer carrier ranges from 20 to 40 μm. The tilt here refers to the vertical height difference of the highest and lowest points on the bottom surface of the wafer carrier. The amount of wafer bow is less than 2 μm and the wafer tilt with respect to the wafer carrier is 5 to 7 μm. This indicates that the wafer carrier tilt is dominating over the wafer bow and tilt, suggesting that the geometry of the gap is not much different from that using the disk. Consequently, the pressure trend should not be much different from the case using the disk alone.

4.5 Concluding Remarks

Pad soaking tests revealed that the IC1000 pad was impermeable to water. Due to the closed-cell microstructure of the pad, water penetrated only the very top layer of voids. This water penetration occurred rapidly during the first 50 hours of pad soaking and diminished after that. The results indicated that mass diffusion of water through the thickness of the pad was not occurring. White light interferometry on the pad showed that the as-delivered pad had a skew in the surface height probability

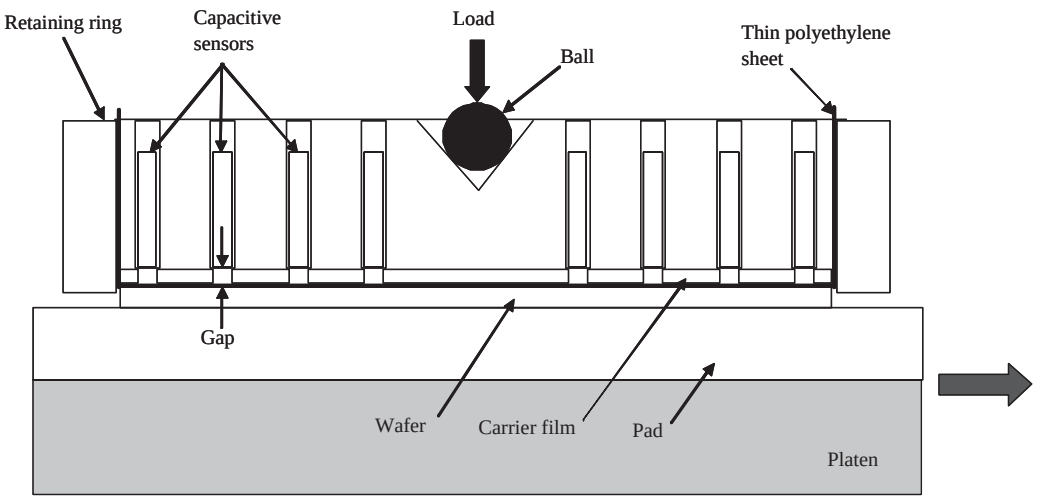

Figure 4.28: Details of wafer carrier for wafer bending experiments

density function while that of the conditioned pad was close to Gaussian. The skew in the surface height probability density function for the as-delivered pad was a result of the nature that the pad is manufactured. Conditioning of the pad resulted in a more Gaussian surface height distribution. Fluid pressure mapping showed that sub-ambient pressure occupied about 70 percent of the area under the disk. A small positive pressure region existed at the trailing edge of the disk. The highest sub-ambient pressure occurred at the leading edge and toward the center of the pad. The magnitude of sub-ambient pressure increased when the pad speed is increased. Disk tilt results indicated that the disk was leaning down towards the leading edge and towards the center of the pad: a condition resulting in the formation of a diverging gap in the fluid film thickness profile. This would lead to the generation of sub-ambient fluid pressures. With a typical CMP wafer carrier, a similar tilt was seen. Dynamic wafer bending experiments revealed that the amount of wafer bow and wafer tilt with respect to the wafer carrier was dominated by the wafer carrier tilt. This indicated that the diverging film thickness profile and hence the sub-ambient pressure should still exist although the magnitudes might be different.

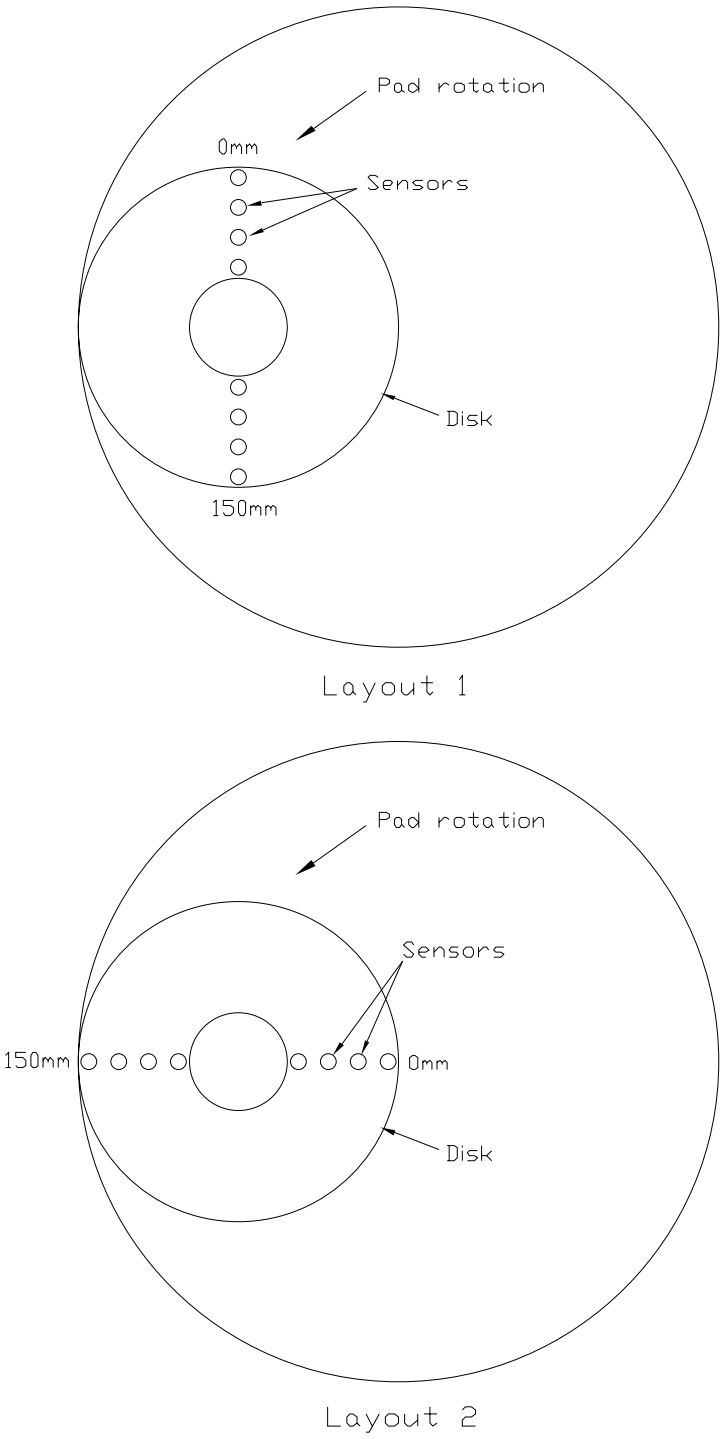

Figure 4.29: Layouts for dynamic wafer bending experiments

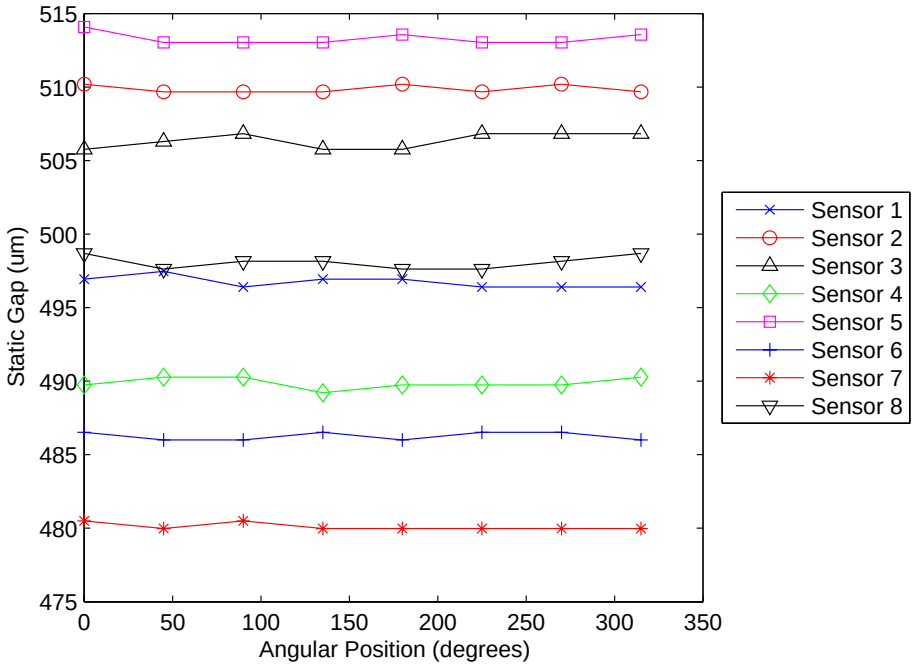

(a) 50 N (L1)

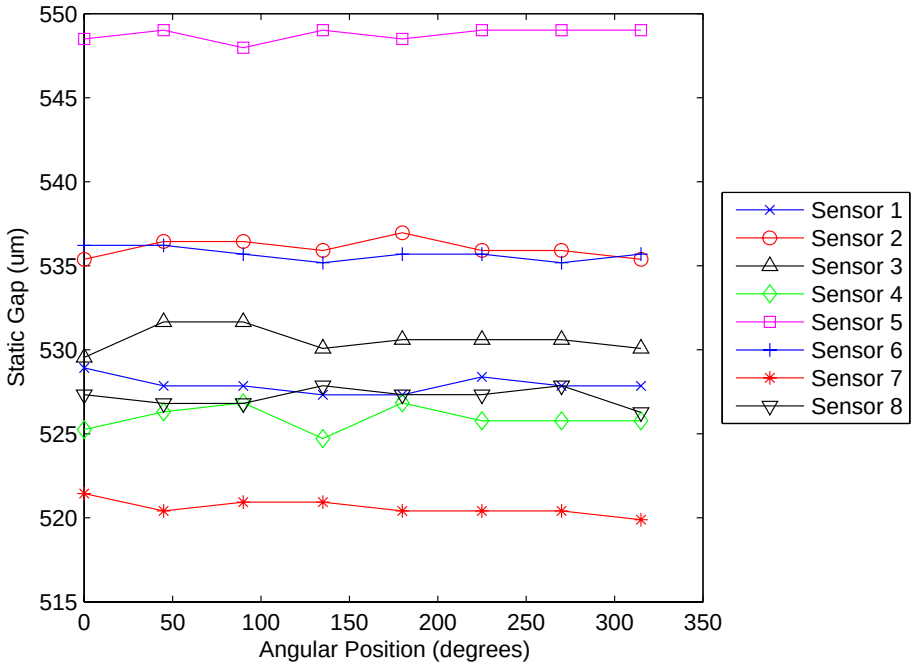

(b) 50 N (L2)

Figure 4.30: Static gaps for wafer bending

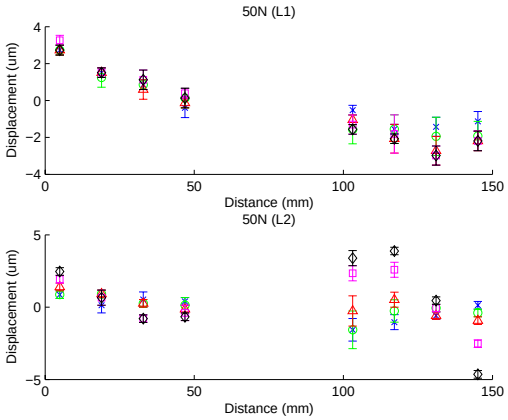

(a) 50 N

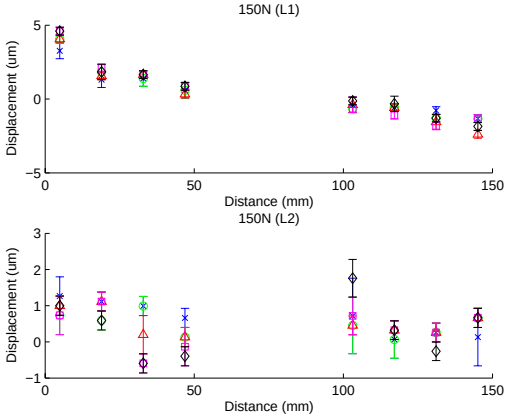

(b) 150 N

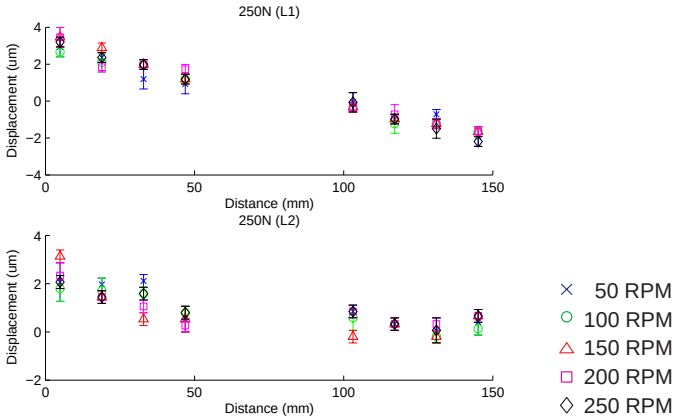

(c) 250 N

Figure 4.31: Wafer bending results

CHAPTER 5

FLUID PRESSURE MODELING

This chapter presents the modeling of the fluid pressures. The pad is modeled as a rough surface which can contain a certain topography. The contact between the disk and the asperities of the pad, and the deformation of the pad asperities are modeled with the Greenwood and Williamson equation. The fluid flow is modeled with the average Reynolds equation for mixed-lubrication taking into account the roughness of the pad. Thermal analysis is not incorporated into this model. The model also accounts for a balance of forces acting on the disk. A code is written in Matlab to incorporate the above features and the finite difference method is used to generate the solution.

5.1 Contact and Deformation Analysis

In this section, the contact refers to that between the disk and the polishing pad and the deformation occurs in the pad. The IC1000 pad is modeled since it is utilized in all the experiments in this research. Due to conditioning, the surface of the pad that is in contact with the disk is different from that of the bulk pad. Furthermore, the softening effect of water on the material occurs only on the surface. Dynamic mechanical analysis studies [75, 76] showed that the IC1000 bulk pad demonstrates storage modulus of 200 to 400 MPa while surface compression tests [61, 77, 78] showed elastic modulus values of less than 15 MPa. The bulk pad is apparently stiffer than the surface layer. Hence, the surface asperity layer

and the bulk pad are modeled separately. The asperity layer is modeled using the Greenwood and Williamson equation for a rough surface while the bulk pad can be approximated as a linear elastic layer since its deformation will be small.

The Greenwood and Williamson equation is given by

$$p_c = \frac{4}{3} E^* \eta R_s^{\frac{1}{2}} \int_d^\infty (z-d)^{\frac{3}{2}} \phi_z(z) dz \tag{5.1}$$

where E^* is the contact modulus defined by the relation

$$\frac{1}{E^*} = \frac{1-\nu_p^2}{E_p} + \frac{1-\nu_w^2}{E_w} \tag{5.2}$$

where p_c is the contact stress, η is the pad asperity density, R_s is the pad asperity tip radius, d is the disk/wafer and pad separation distance, and z is the pad asperity height. $\phi_z(z)$ is the pad asperity height distribution function and can be assumed to be Gaussian in nature as found in the previous chapter. E_p and ν_p refer to the elastic modulus and Poisson's ratio of the pad respectively. E_w and ν_w refer to the elastic modulus and Poisson's ratio of the disk/wafer respectively.

Assuming $E_w \gg E_p$ and replacing $\phi_z(z)$ by the Gaussian function, Equation 5.2 can be written as

$$p_c = \frac{4 E_p \eta R_s^{\frac{1}{2}}}{3(1-\nu_p^2)} \int_d^\infty (z-d)^{\frac{3}{2}} \frac{1}{s\sqrt{2\pi}} e^{-\frac{z^2}{2s^2}} dz \tag{5.3}$$

where s is the standard deviation of z and can be equated with the root-mean-square roughness of the pad surface obtained through profilometry measurements.

The integral part of the Greenwood and Williamson equation is solved numerically by the composite Simpson's rule using an interval of 1 nm and the upper bound truncated at 166 standard deviations.

The normal vector of the tilted disk with respect to the global cartesian coordinate system is given by

$$\vec{n_w} = \begin{pmatrix} sin\phi cos\theta_a \\ sin\phi sin\theta_a \\ cos\phi \end{pmatrix} \tag{5.4}$$

Consequently, d is given by

$$d(x,y) = -(xtan\phi cos\theta_a + ytan\phi sin\theta_a) + z_{off} - S_{pn} \tag{5.5}$$

where z_{off} is the vertical distance between the center of the bottom face of the disk and the surface of the platen, and S_{pn} is the deformed thickness of the bulk pad. The cartesian coordinates x and y are with respect to the center of the disk.

The stress and deformation experienced by the bulk pad is related by

$$p_c + p = E_{bp}(\frac{S_{p0} - S_{pn}}{S_{p0}}) \tag{5.6}$$

where p is the fluid pressure, E_{bp} is the bulk pad modulus and S_{p0} is the undeformed thickness of the bulk pad. Figure 5.1 shows the variables used in the contact and deformation model.

5.2 Fluid Mechanics

The Reynolds equation reduced from the Navier-Stokes equations is used to simulate the fluid mechanics of the process. To adjust for the fluid flow due to roughness of the pad, the flow factors method developed by Patir and Cheng [79, 80] is used.

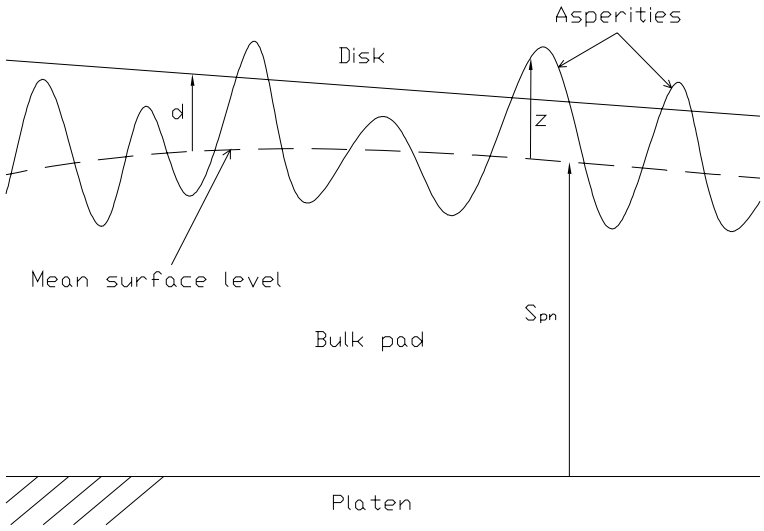

Figure 5.1: Contact and deformation model

5.2.1 Navier-Stokes and Reynolds equations.

The Navier-Stokes equations in Cartesian coordinates for constant viscosity and constant density are given by

$$\rho(\frac{\partial u}{\partial t}+u\frac{\partial u}{\partial x}+v\frac{\partial u}{\partial y}+w\frac{\partial u}{\partial z}) = -\frac{\partial p}{\partial x}+\mu(\frac{\partial^2 u}{\partial x^2}+\frac{\partial^2 u}{\partial y^2}+\frac{\partial^2 u}{\partial z^2})+\rho g_x \quad (5.7)$$

$$\rho(\frac{\partial v}{\partial t}+u\frac{\partial v}{\partial x}+v\frac{\partial v}{\partial y}+w\frac{\partial v}{\partial z}) = -\frac{\partial p}{\partial y}+\mu(\frac{\partial^2 v}{\partial x^2}+\frac{\partial^2 v}{\partial y^2}+\frac{\partial^2 v}{\partial z^2})+\rho g_y \quad (5.8)$$

$$\rho(\frac{\partial w}{\partial t}+u\frac{\partial w}{\partial x}+v\frac{\partial w}{\partial y}+w\frac{\partial w}{\partial z}) = -\frac{\partial p}{\partial z}+\mu(\frac{\partial^2 w}{\partial x^2}+\frac{\partial^2 w}{\partial y^2}+\frac{\partial^2 w}{\partial z^2})+\rho g_z \quad (5.9)$$

where u, v and w are velocities in the x, y and z directions respectively. g_x, g_y and g_z are associated with the body forces in the x, y and z directions respectively.

The Navier-Stokes equations in cylindrical polar coordinates for constant viscosity and constant density are given by

$$\begin{aligned}&\rho(\frac{\partial v_r}{\partial t}+v_r\frac{\partial v_r}{\partial r}+\frac{v_\theta}{r}\frac{\partial v_r}{\partial \theta}+v_z\frac{\partial v_r}{\partial z}-\frac{v_\theta^2}{r})\\&=-\frac{\partial p}{\partial r}+\mu(\frac{\partial^2 v_r}{\partial r^2}+\frac{1}{r}\frac{\partial v_r}{\partial r}+\frac{1}{r^2}\frac{\partial^2 v_r}{\partial \theta^2}+\frac{\partial^2 v_r}{\partial z^2}-\frac{v_r}{r^2}-\frac{2}{r^2}\frac{\partial v_\theta}{\partial \theta})+\rho g_r\end{aligned} \tag{5.10}$$

$$\begin{aligned}&\rho(\frac{\partial v_\theta}{\partial t}+v_r\frac{\partial v_\theta}{\partial r}+\frac{v_\theta}{r}\frac{\partial v_\theta}{\partial \theta}+v_z\frac{\partial v_\theta}{\partial z}+\frac{v_r v_\theta}{r})\\&=-\frac{1}{r}\frac{\partial p}{\partial \theta}+\mu(\frac{\partial^2 v_\theta}{\partial r^2}+\frac{1}{r}\frac{\partial v_\theta}{\partial r}+\frac{1}{r^2}\frac{\partial^2 v_\theta}{\partial \theta^2}+\frac{\partial^2 v_\theta}{\partial z^2}-\frac{v_\theta}{r^2}+\frac{2}{r^2}\frac{\partial v_r}{\partial \theta})+\rho g_\theta\end{aligned} \tag{5.11}$$

$$\begin{aligned}&\rho(\frac{\partial v_z}{\partial t}+v_r\frac{\partial v_z}{\partial r}+\frac{v_\theta}{r}\frac{\partial v_z}{\partial \theta}+v_z\frac{\partial v_z}{\partial z})\\&=-\frac{\partial p}{\partial z}+\mu(\frac{\partial^2 v_z}{\partial r^2}+\frac{1}{r}\frac{\partial v_z}{\partial r}+\frac{1}{r^2}\frac{\partial^2 v_z}{\partial \theta^2}+\frac{\partial^2 v_z}{\partial z^2})+\rho g_z\end{aligned} \tag{5.12}$$

The Reynolds equation can be derived from the Navier-Stokes equations and the continuity equation. The continuity equations from the principle of mass conservation in Cartesian and cylindrical polar coordinates respectively are given by

$$\frac{\partial u}{\partial x}+\frac{\partial v}{\partial y}+\frac{\partial w}{\partial z}=0 \tag{5.13}$$

$$\frac{\partial \rho}{\partial t}+\frac{1}{r}\frac{\partial}{\partial r}(\rho r v_r)+\frac{1}{r}\frac{\partial}{\partial \theta}(\rho v_\theta)+\frac{\partial}{\partial z}(\rho v_z)=0 \tag{5.14}$$

Considering only tangential motion and constant density and viscosity, the Reynolds equation in cylindrical polar coordinates is given by

$$\frac{\partial}{\partial r}(rh^3\frac{\partial p}{\partial r})+\frac{1}{r}\frac{\partial}{\partial \theta}(h^3\frac{\partial p}{\partial \theta})=6\mu[v_r\frac{\partial}{\partial r}(rh)+v_\theta\frac{\partial h}{\partial \theta}] \tag{5.15}$$

The polar Reynolds equation can be further simplified by choosing a coordinate system such that the orgin is situated at the center of the pad. The disk surface would be the stationary surface and the pad the moving surface. In this system, motion occurs only in the θ direction due to the pad rotation (hence, $v_\theta = r\omega$)

$$\frac{\partial}{\partial r}(rh^3\frac{\partial p}{\partial r}) + \frac{1}{r}\frac{\partial}{\partial \theta}(h^3\frac{\partial p}{\partial \theta}) = 6\mu r\omega\frac{\partial h}{\partial \theta} \tag{5.16}$$

5.2.2 The average Reynolds equation.

The Reynolds equation is useful for the hydrodynamic regime where the combined roughness, s, of the two opposing surfaces are smaller than the film thickness, h, and there is little or no contact between the asperities of the surfaces. For h/s $\gg$ 3, the roughness effects are not important and the smooth film Reynolds equation is sufficiently accurate. However, as h/s approaches 3, roughness effects become important. When h/s $<$ 3, contacts between asperities from the opposing surfaces can occur and the system goes into the mixed lubrication regime. In CMP, the surfaces involved are a relatively flat and rigid wafer, and a rough and soft pad. For the rates of material removal observed to occur, there has to be contact between the asperities of the pad and the wafer surface. Pad glazing is also another sign of intimate wafer and pad contact. So, a mixed lubrication approach has to be taken.

Much work has been done to incorporate roughness effect into lubrication. Studies [81, 82] to model the roughness deterministically prove to be computationally exhaustive when modeling large systems with small topographies. Sometimes, getting the topography of the system experimentally and in intricate details can be difficult and impractical. Hence, some work [83–87] has been done to employ stochastic concepts to solve the problem. Most of these models are limited to one-dimensional ridges oriented either transversely or longitudinally. It is very difficult to extend to three-dimensional or anisotropic roughness using the stochastic approach. There is also a perturbation method [88, 89] to model roughness in lubrication.

One of the most versatile and widely used is the average flow model developed by

Patir and Cheng [79, 80]. It is a heuristic approach based on numerically solving the Reynolds equation on a model bearing with a randomly generated surface roughness and then deriving the average Reynolds equation from mean flow quantities. Any three-dimensional surface with known statistical properties or even data from a real surface can be analyzed through the flow simulation and the pressure and shear flow factors used to modify the Reynolds equation derived. Patir and Cheng had tabulated the pressure and shear flow factor functions for a wide range of roughnesses including isotropic, longitudinally and transversely oriented surfaces. This model will be used in this research.

The average Reynolds equation in cylindrical polar coordinates is given by

$$\frac{\partial}{\partial r}(\phi_r r h^3 \frac{\partial p}{\partial r}) + \frac{1}{r}\frac{\partial}{\partial \theta}(\phi_\theta h^3 \frac{\partial p}{\partial \theta}) = 6\mu r\omega \frac{\partial h_{T,avg}}{\partial \theta} + 6\mu r\omega s \frac{\partial \phi_s}{\partial \theta} \tag{5.17}$$

where ϕ_r and ϕ_θ are pressure flow factors and are assumed to be equal due to isotropic roughness of the pad. The shear flow factor is given by ϕ_s.

The existence of asperities protruding into the film thickness causes obstruction in the fluid flow. Hence, the pressure flow factor compares the average pressure flow in a rough bearing to that in a smooth bearing, and can be expressed empirically as a function of the film thickness ratio H (= h/s). For isotropic surfaces with a Peklenik number of 1, the pressure flow factor as derived by Patir and Cheng is

$$\phi_r = \phi_\theta = 1 - 0.9e^{-\frac{0.56h}{s}} \tag{5.18}$$

The shear flow factor, ϕ_s, takes into account additional flow transport due to sliding between two rough surfaces. Figure 5.2 illustrates the two extreme cases where the rough surface moving with respect to a smooth surface would mean ad-

ditional flow transport revealed by a positive shear flow factor, and vice versa. In the special case of two surfaces moving past each other with identical roughness, the resultant shear flow factor would be zero. In CMP, the rough surface is moving, thus carrying additional fluid in the valleys of the polishing pad. Consequently, the shear flow factor as derived by Patir and Cheng is given by

$$\phi_s = 1.899(\frac{h}{s})^{0.98} e^{-0.92\frac{h}{s}+0.05(\frac{h}{s})^2} \tag{5.19}$$

Figure 5.3 shows the film thickness function between two surfaces. The local film thickness is given by

$$h_T = h + \delta_1 + \delta_2 \tag{5.20}$$

where h is the nominal film thickness and δ_1, δ_2 are the random roughness amplitudes of the two surfaces measured from the mean levels. The combined roughness is $\delta = \delta_1 + \delta_2$ and it has a standard deviation, $s = \sqrt{{s_1}^2 + {s_2}^2}$.

Since h_T is zero when contact occurs, the average gap, $h_{T,avg}$, can be defined as

$$h_{T,avg} = \int_{-h}^{\infty} (h + \delta) f_\delta(\delta) d\delta \tag{5.21}$$

where $f_\delta(\delta)$ is the probability density function of δ.

A Gaussian function for δ is assumed due to the random nature of the pad surface and after setting the mean of δ to zero

$$f_\delta(\delta) = \frac{1}{s\sqrt{2\pi}} e^{-\frac{\delta^2}{2s^2}} \tag{5.22}$$

Solving for $h_{T,avg}$ yields

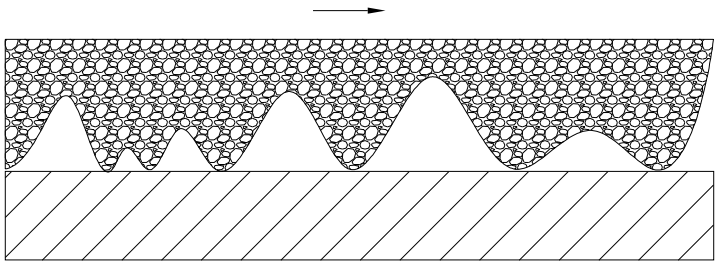

(a) Rough surface moving, $V_{r1} = 1$

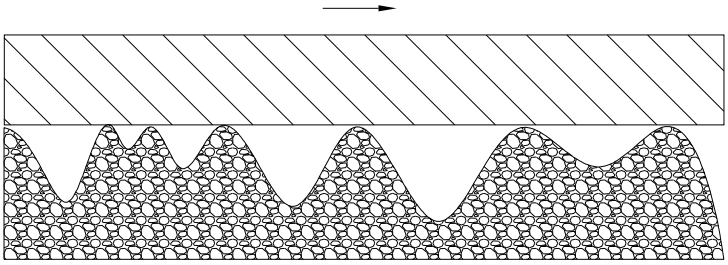

(b) Smooth surface moving, $V_{r1} = 0$

Figure 5.2: Variance ratios for shear flow factor

$$h_{T,avg} = \frac{h}{2} + \frac{h}{2} erf(\frac{h}{s\sqrt{2}}) + \frac{se^{-\frac{h^2}{2s^2}}}{\sqrt{2\pi}} \tag{5.23}$$

Substituting the above equation and the flow factors functions into Equation 5.17 gives

$$\begin{aligned} &\frac{\partial}{\partial r}[(1 - 0.9e^{-\frac{0.56h}{s}})rh^3\frac{\partial p}{\partial r}] + \frac{1}{r}\frac{\partial}{\partial \theta}[(1 - 0.9e^{-\frac{0.56h}{s}})h^3\frac{\partial p}{\partial \theta}] \\ =&3\mu r\omega\frac{\partial h}{\partial \theta}[1 + erf(\frac{h}{s\sqrt{2}})] + 6\mu r\omega s\frac{\partial}{\partial \theta}[1.899(\frac{h}{s})^{0.98}e^{-0.92\frac{h}{s}+0.05(\frac{h}{s})^2}] \end{aligned} \tag{5.24}$$

5.3 Force and Moment Balance

To elucidate the orientation of the disk, a force and moment balance of the disk is required. Figure 5.4 shows the free body diagram of the disk. The load is applied vertical downwards through the ball joint on the top surface of the disk. A holding

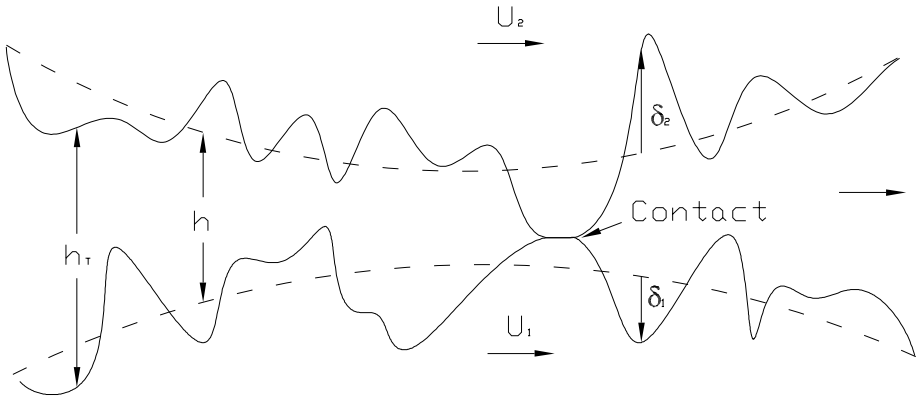

Figure 5.3: Film thickness function

force is required to prevent horizontal displacement of the disk. The contact, fluid and shear forces indicated are all distributed forces acting on the bottom of the disk. The contact force is the upward force acting by the asperities of the pad on the disk. The shear force refers to the horizontal frictional force due to the pad asperities on the disk and is assumed to be the contact force multiplied by the friction coefficient. The fluid shear acting on the disk is very small compared to the solid shear and is not taken into account. For a typical pad speed of 50 rpm and a nominal film thickness of 20 μm, the fluid shear stress that can arise on the surface of the disk is about 20 Pa, whereas, the typical solid shear stress is 3 orders of magnitude higher. The fluid force acts vertically and can be upwards or downwards at different regions. Surface tension and buoyancy forces are small in comparison and are not incorporated. Since the disk is constrained from moving horizontally and from spinning, the force and moment balance equations reduce to force balance in the vertical direction and moment balance about the x and y axes. The summations of force and moments are then given by

$$\sum F_z = F_c + F_f - F_L - mg \tag{5.25}$$

$$\sum M_x = M_{x,c} + M_{x,f} \tag{5.26}$$

$$\sum M_y = M_{y,c} + M_{y,f} \tag{5.27}$$

where F_c is the summation of solid contact pressure, F_f is the summation of fluid pressure, F_L is the applied load and m is the mass of the disk. In the moment equations, the subscript "c" refers to moment contributed by the solid contact pressure and the subscript "f" refers to moment contributed by the fluid pressure. The solid and fluid components of the moments are given by

$$M_{x,c} = \sum (F_{c,ij} y + F_{sy,ij} d_{pivot}) \tag{5.28}$$

$$M_{x,f} = \sum F_{f,ij} y \tag{5.29}$$

$$M_{y,c} = -\sum (F_{c,ij} x + F_{sx,ij} d_{pivot}) \tag{5.30}$$

$$M_{y,f} = -\sum F_{f,ij} x \tag{5.31}$$

The term d_{pivot} refers to the height of the pivot point above the bottom surface of the disk. The terms $F_{sx,ij}$ and $F_{sy,ij}$ refers to the x and y components of the solid shear force respectively. $F_{s,ij}$ can be computed by

$$F_{s,ij} = \mu_k F_{c,ij} \tag{5.32}$$

where μ_k is the kinetic friction coefficient between the disk and the pad.

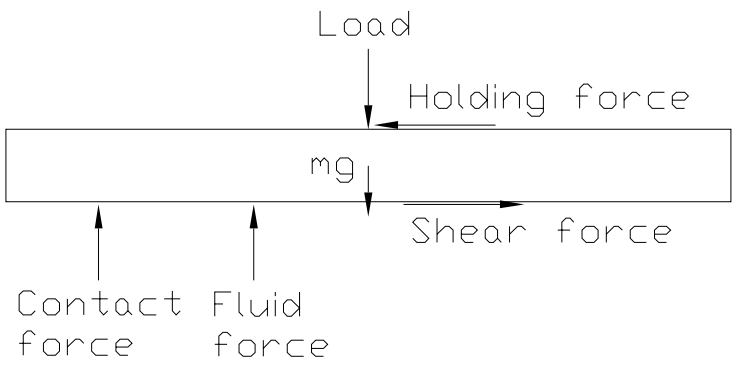

Figure 5.4: Free body diagram of disk

5.4 Finite Difference

5.4.1 Discretization of the solution domain.

The solution domain consist of the an area larger than the size of the disk. The area is meshed with a polar grid with the origin at the center of the pad. Contact and fluid pressures outside the disk-pad region are set to zero. Figure 5.5 shows part of the mesh.

5.4.2 Discretization of the average Reynolds equation.

The film thickness and fluid pressure are set to be linear between grid points and using the finite central difference method gives

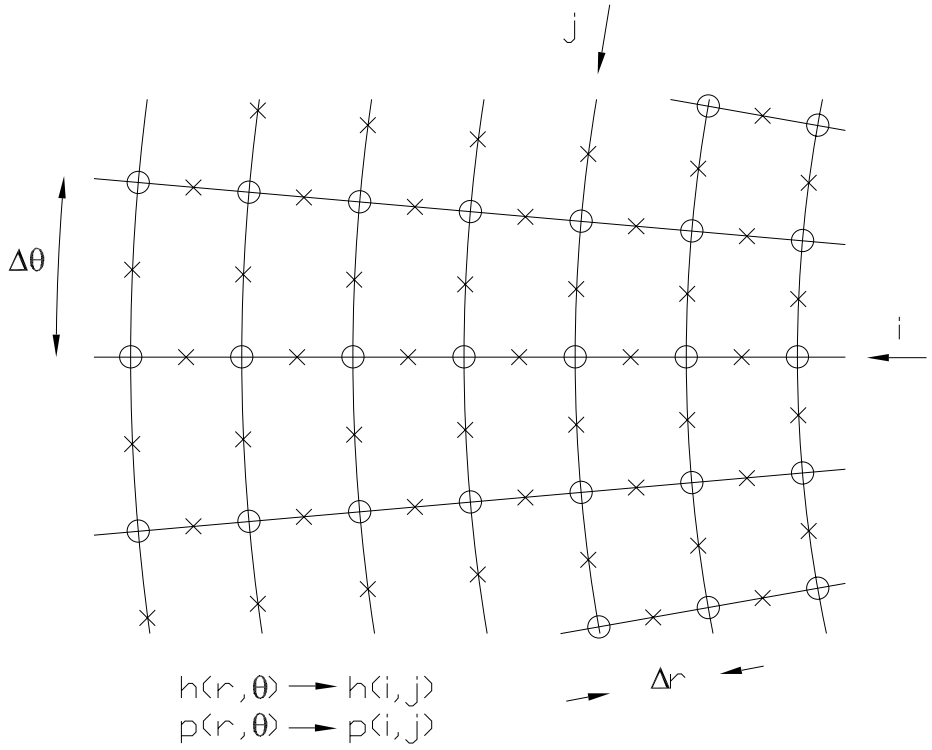

Figure 5.5: Finite difference mesh

$$(\frac{\partial p}{\partial r})_{i,j} = \frac{p_{i+1,j} - p_{i-1,j}}{2\Delta r} \tag{5.33}$$

$$(\frac{\partial p}{\partial \theta})_{i,j} = \frac{p_{i,j+1} - p_{i,j-1}}{2\Delta \theta} \tag{5.34}$$

$$(\frac{\partial^2 p}{\partial r^2})_{i,j} = \frac{p_{i+1,j} - 2p_{i,j} + p_{i-1,j}}{(\Delta r)^2} \tag{5.35}$$

$$(\frac{\partial^2 p}{\partial \theta^2})_{i,j} = \frac{p_{i,j+1} - 2p_{i,j} + p_{i,j-1}}{(\Delta \theta)^2} \tag{5.36}$$

$$(\frac{\partial h}{\partial r})_{i,j} = \frac{h_{i+1,j} - h_{i-1,j}}{2\Delta r} \tag{5.37}$$

$$(\frac{\partial h}{\partial \theta})_{i,j} = \frac{h_{i,j+1} - h_{i,j-1}}{2\Delta \theta} \tag{5.38}$$

The above equations are substituted into Equation 5.24 to obtain the discretized average Reynolds equation.

5.5 Computational Procedure

The computational procedure as seen in Figure 5.6 for the fluid pressure model consists of three loops: one for the contact pressure, one for the fluid pressure, and one for the force and moment balance. In the figure, I.G. stands for initial guess, R.E. stands for Reynolds equation, F.D. stands for finite difference, S.O.R. stands for successive over relaxation, and F.M.B. stands for force and moment balance. The model takes an initial guess of the orientations angles and fly height and computes the equivalent film thickness and the new bulk pad profile, $S_{pn,ij}$. The contact pressure loop uses a simple one-point iteration method and is exited when the maximum difference in two consecutive iterations of $p_{c,ij}$ is less than 1 millipascal. Typical number of iterations for this loop is less than 50. In the fluid pressure loop, the film thickness distribution is used to compute the fluid pressure profile using Reynolds equation. The successive over relaxation method is used to solve the Reynolds equation. The tolerance for exiting this loop is set to 1 millipascal. Typical number of iterations is less than 500. A summation of forces and moments acting on the disk is performed. A modified Newton's method is used to achieve convergence of the model. This is carried out by a Matlab software optimization function. The function is set to minimize the sum of the squares of the residuals from the load and moment balance equations. The tolerance for convergence is set to 0.0001. The number of iterations stays within 50. A new set of orientation angles and fly height is obtained and the model is updated. Multiple iterations are carried out until the solution converges. The values of the parameters used in the model are listed in Table 5.1.

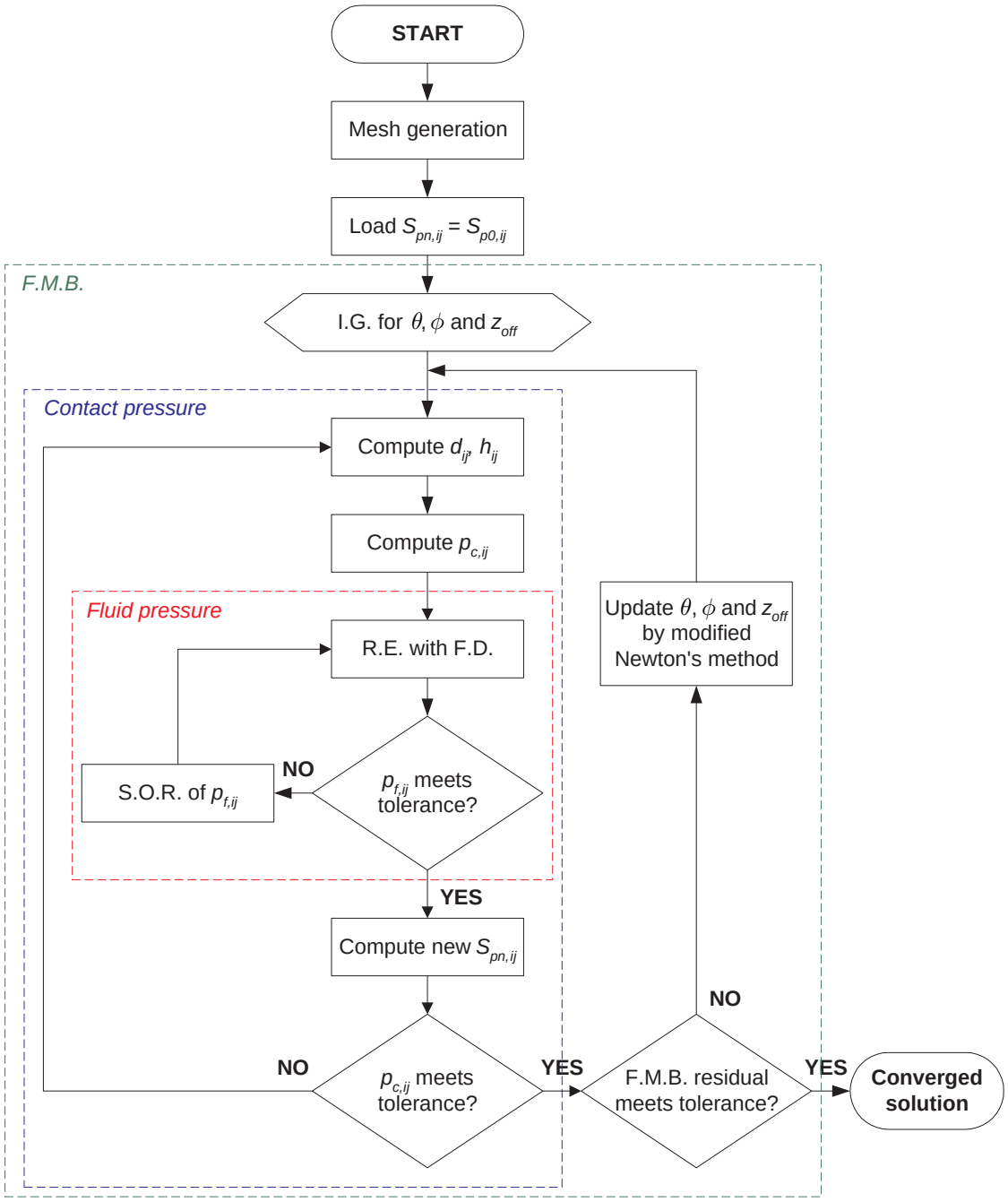

Figure 5.6: Computational procedure for fluid flow model

Table 5.1: Values of parameters used in the fluid pressure model

Parameter	Value
d_{pivot}	0.026 m
m	2.75 kg
s	6 μm
η	766x$10^6 m^{-2}$
μ	0.001 Pa·s
μ_k	0.43
ν_p	0.4
x_c	0.075 m
E_p	100 MPa
E_{bp}	300 MPa
R_p	0.15 m
R_s	68 μm
R_w	0.075 m

5.6 Results and Discussion

This section will describe two cases involving two different pads: which will be called Pad 1 and Pad 2. Surface height profiling was performed on both pads to obtain data on the topography of the pad. Pressure mapping and the modeling results will be compared. Further modeling results showing the effects of the various input parameters will be shown based on the topography of Pad 2.

5.6.1 Case studies.

Pad 1 was machined on a lathe to remove 150-200 μm of pad material. The pad surface prior to pressure mapping was conditioned with a diamond-impregnated disk and the pad had been soaked for more than 2 days. No machining was carried out on Pad 2 but it had been conditioned and soaked for at least 2 days before the pressure mapping. So, Pad 2 represents the typical pad used for CMP.

Both pads were profiled with a Taylor Hobson stylus profilometer, which has a maximum scan length of 0.12 m. Since the pads have diameters of 0.3 m, 3 scans of 0.12 m each were taken along the diameter of each pad. The left scan was from 0 to 0.12 m, the center scan from 0.09 to 0.21 m, and the right scan from 0.18 to 0.3 m. This results in overlaps in scan length of 0.03 m between the left and center scans, and between the center and right scans. These overlaps were used to stitch the 3 scans together to obtain a 0.3 m diametric scan. The procedure for this is as follows. The center scan was first leveled and the left 0.03 m overlap region of the scan was fitted with a linear regression line. The same was done for the 0.03 m overlap region of the left scan. The left scan was then rotated and translated such that the fitted lines of the overlap regions of the left and center scans coincide. This procedure was also carried out to match the right scan with the center scan. Figure 5.7 shows

the three scans across the diameter for Pad 1 after stitching. The scans show that the pad profile is axisymmetric about the center of the pad. Features that occur symmetrically on the scan are ridges from the tool bit on the lathe or are caused by conditioning. They are much larger in horizontal scale than the native roughness of the pad, which is a foam with a mean void size of 30 μm. A 249 point ($\approx$1.9 mm) moving average was used to estimate the mean surface of the stitched profile. The fitted profile for Pad 1 is shown in Figure 5.8. This figure shows that the mean surface constructed captures the high points on the pad. The stitched and fitted profiles for Pad 2 are shown in Figure 5.9 and Figure 5.10 respectively. For Pad 1, the difference in height between the center of the pad and the ridge close to the edge is about 40 μm. For Pad 2, this difference in height is about 20 μm. For simulation purpose, only half of the fitted profile is used since the profile is axisymmetric in nature.

Pressure mapping was carried out on Pad 1 with a load of 30 N and a pad rotation speed of 150 rpm. For Pad 2, the load was 50 N and the pad rotation speed was 50 rpm. Figure 5.11 and 5.12 show the pressure maps for Pad 1 and Pad 2 respectively. Triangle-based linear interpolation performed by Matlab was used to create the plots. In both cases, a large proportion of the area under the disk shows negative pressure. The highest negative pressure is located close to the leading edge and the center of the pad. A positive pressure region is seen at the trailing edge and skewed to the center of the pad. For Pad 1, the lowest pressure sampled was -90 kPa and the highest was +51 kPa. For Pad 2, the lowest pressure was -44 kPa and the highest +7 kPa.

Figure 5.13 shows the calculated fluid pressure distribution for Pad 1. It can be seen that the centers of positive and negative pressure produced by the model are

at 4 and 2 o'clock, in agreement with the data in Figure 5.11. The shape of contour of zero fluid pressure also has the same size and general shape as in the measured map. The calculated positive pressure maximum is 13 kPa compared with 51 kPa measured. The calculated maximum negative pressure is -80 kPa compared with the -90 kPa measured. The secondary minimum of suction at the 10 o'clock position in the experimental map is also predicted by the model at the same location.

The predicted fluid pressure map for Pad 2 is shown in Figure 5.14. Comparing with the measured pressure data in Figure 5.12, the extend and location of the positive pressure region are in agreement, from 3 to 9 o'clock. The location of the most negative pressure is also predicted by the model. There is also a suggestion in the data that the suction region from Pad 2 is more delocalized than the data from Pad 1, and this too is predicted by the model. The maximum and minimum fluid pressures are +3 and -7 kPa predicted vs. +7 and -44 kPa measured.

The film thickness distribution is affected by the tilt of the disk and the topography of the pad. Figure 5.15 shows the film thickness distribution for Pad 2. Typical film thickness ranges from 10 to 30 μm. Film thickness is small on the high ridges of the pad and is larger in the valleys. The root-mean-square roughness of the pad is 6 μm which means there is contact between the wafer and the pad, indicating mixed lubrication. Evidence of contact can be seen in the contact pressure distribution for Pad 2, in Figure 5.16. Contact pressures are higher on the ridges than at the valleys. At the leading edge of the disk/wafer, the contact pressure is also higher due to the forward tilt of the wafer.

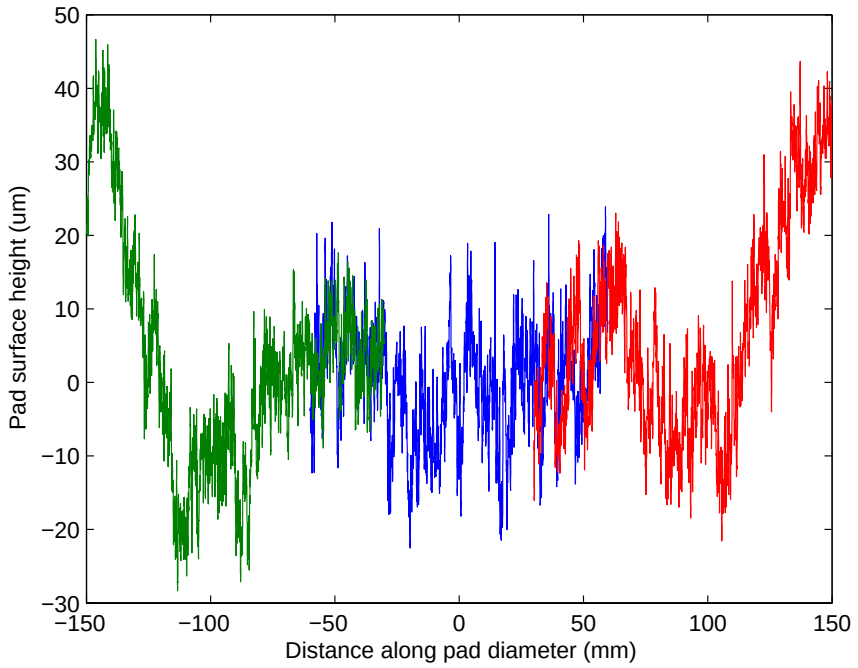

Figure 5.7: Pad 1 stitched profile

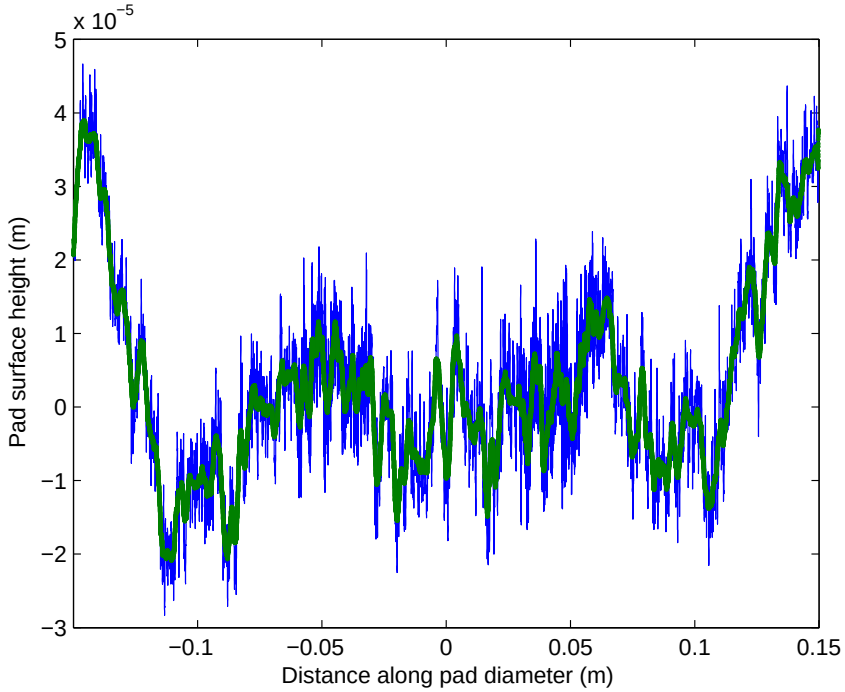

Figure 5.8: Pad 1 stitched and fitted profile

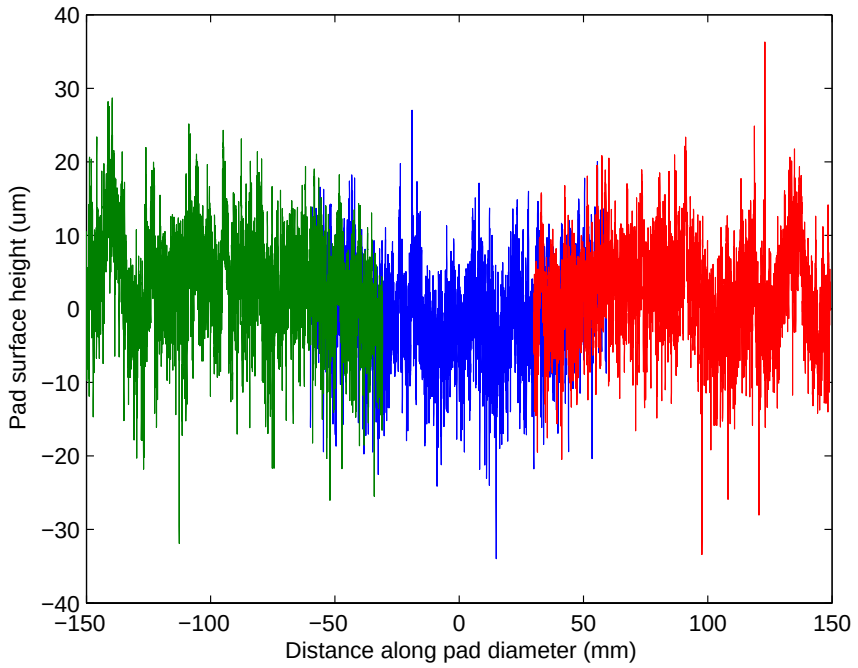

Figure 5.9: Pad 2 stitched profile

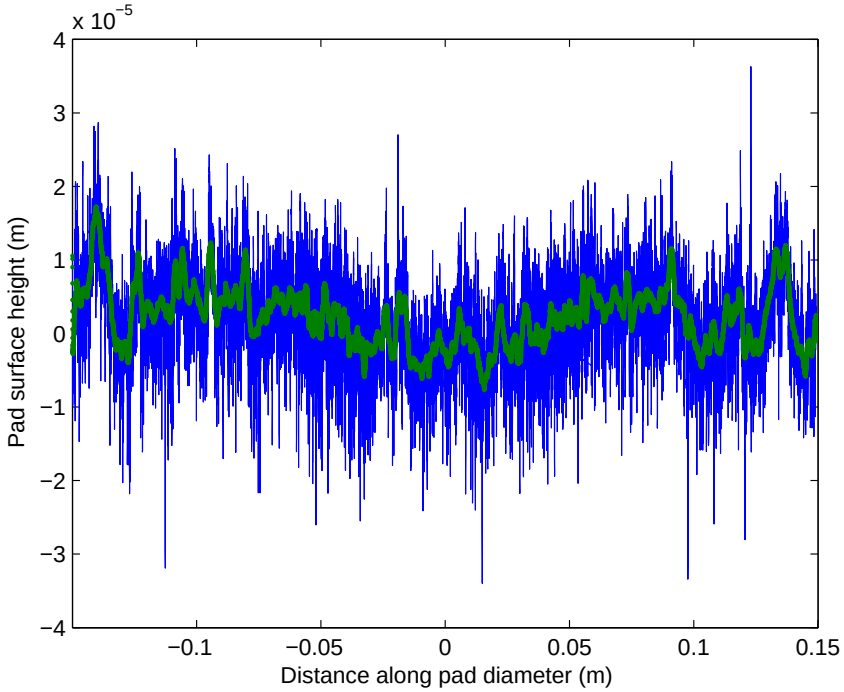

Figure 5.10: Pad 2 stitched and fitted profile

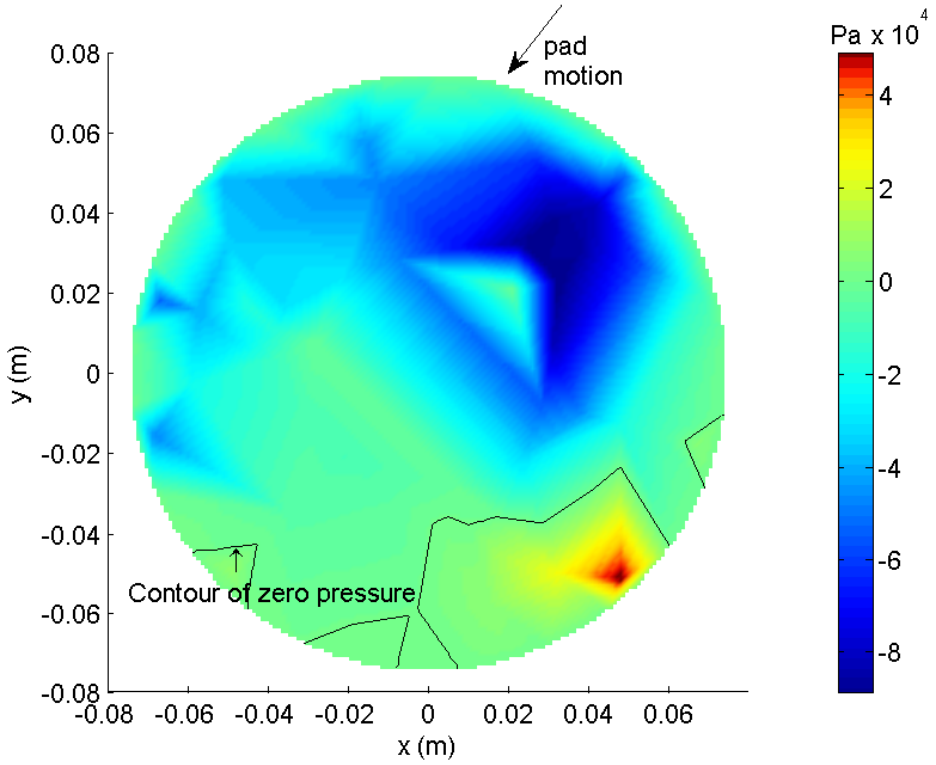

Figure 5.11: Experimental pressure map for Pad 1

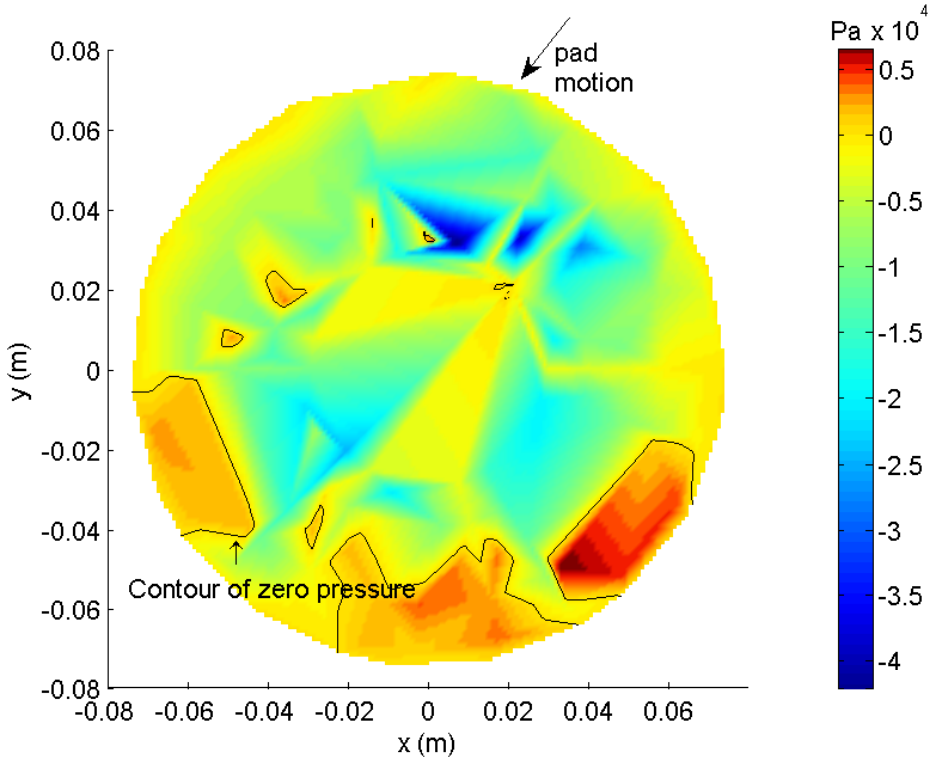

Figure 5.12: Experimental pressure map for Pad 2

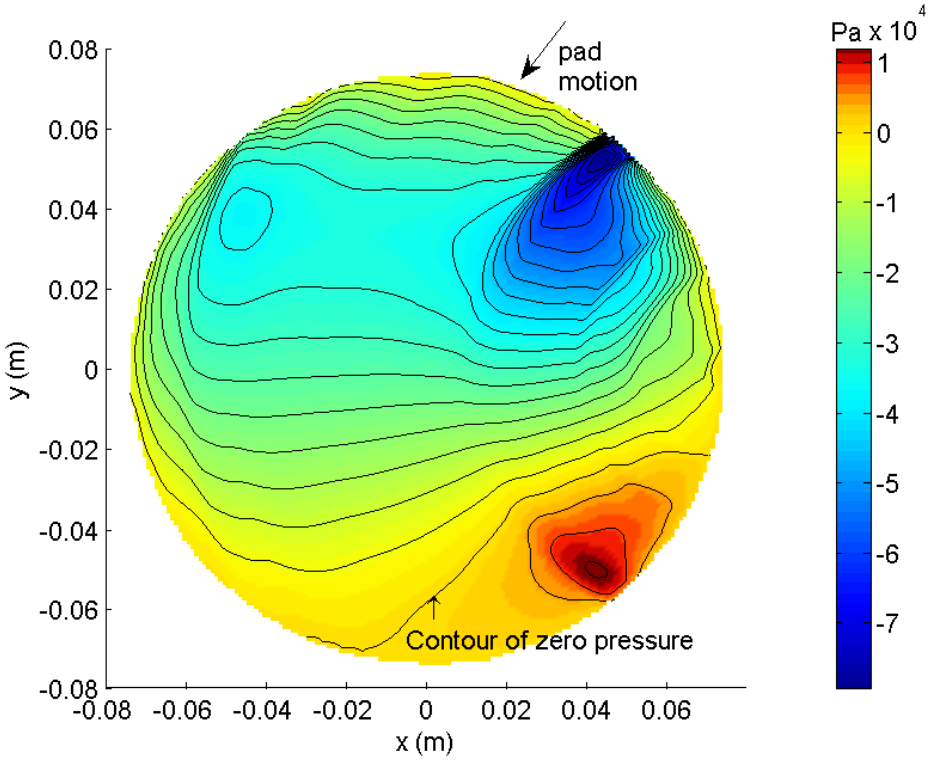

Figure 5.13: Predicted pressure map for Pad 1

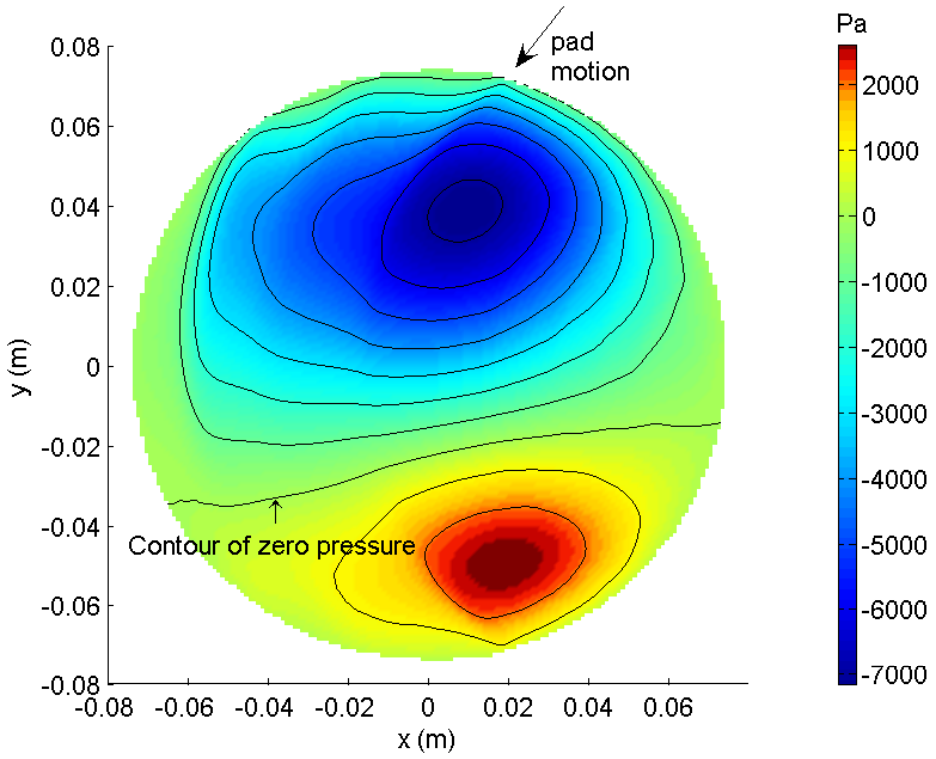

Figure 5.14: Predicted pressure map for Pad 2

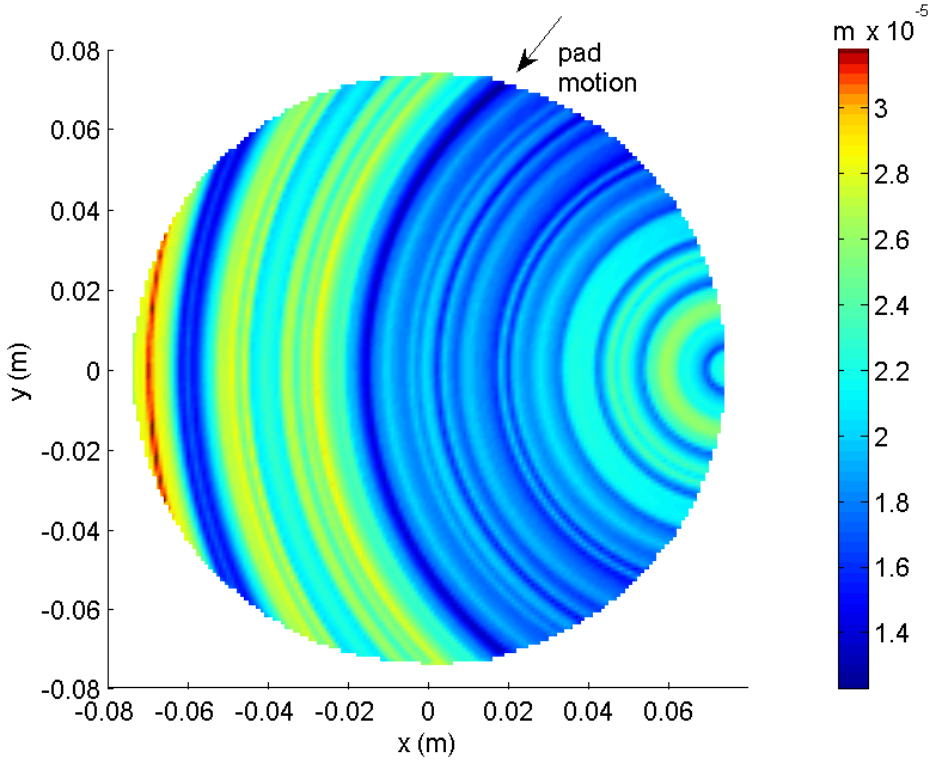

Figure 5.15: Predicted nominal film thickness map for Pad 2

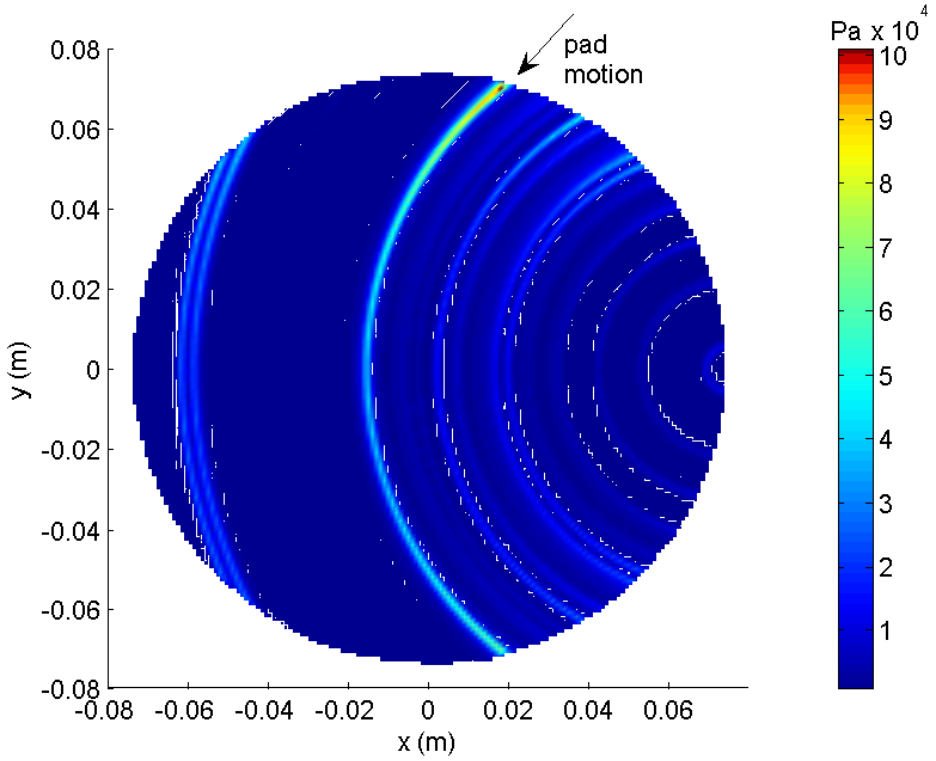

Figure 5.16: Predicted contact pressure map for Pad 2

5.6.2 Velocity effect.

The pad velocity effect on the fluid pressure is also predicted by the model. Figure 5.17 shows the speed effect on the fluid pressure predicted by the model using Pad 2 topography at an applied load of 50 N. It can be seen that as the pad velocity increases, both the magnitudes of the positive and negative fluid pressures increase, in agreement with the experimental observations.

5.6.3 Flow fields.

Figure 5.18 illustrates the kinds of flow between two parallel plates. The Couette flow is driven by shear flow while the Poiseuille flow is driven by fluid pressure gradient. In most practical situations, a combination of both flows are present as shown in the rightmost sub-figure.

The radial velocity component for full film can be derived from the Equation 5.10 and is given by

$$v_r = \frac{1}{2\mu}\frac{\partial p}{\partial r}(z^2 - hz) \tag{5.39}$$

The volumetric flow rate in the radial direction per unit θ after adjustment by the pressure flow factor is

$$q_r = -\phi_r \frac{h^3}{12\mu}\frac{\partial p}{\partial r} \tag{5.40}$$

Hence, the average radial velocity component across the film thickness is given by

$$\bar{v}_r = \frac{q_r}{h} = -\phi_r \frac{h^2}{12\mu}\frac{\partial p}{\partial r} \tag{5.41}$$

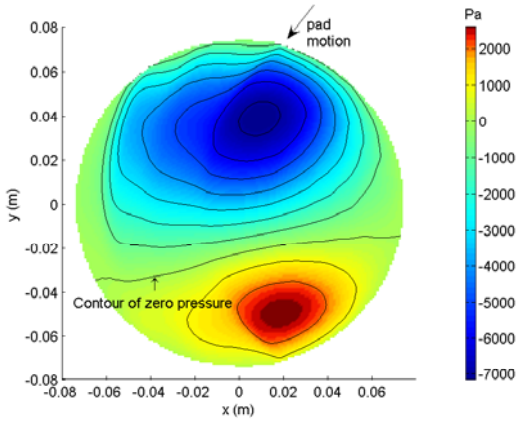

(a) 50 rpm

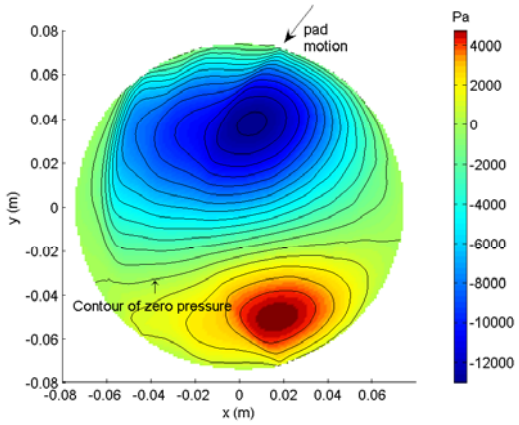

(b) 150 rpm

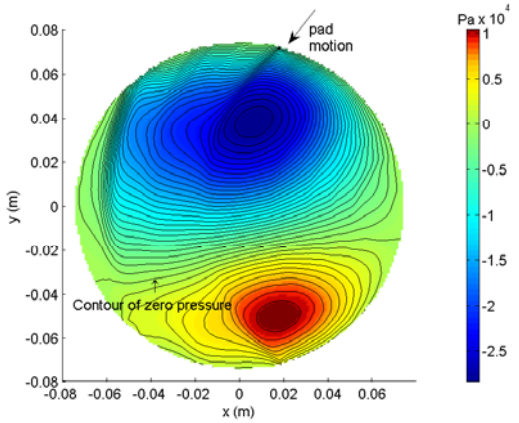

(c) 250 rpm

Figure 5.17: Velocity effect on fluid pressure (Pad 2, 50 N)

The tangential velocity component for full film can be derived from the Equation 5.11 and is given by

$$v_\theta = \frac{1}{2\mu r}\frac{\partial p}{\partial \theta}z^2 + \frac{z}{h}[r\omega - \frac{1}{\mu r}\frac{\partial p}{\partial \theta}\frac{h^2}{2}] \tag{5.42}$$

The volumetric flow rate in the tangential direction per unit r after adjustment by the pressure and shear flow factors is

$$q_\theta = -\phi_\theta \frac{h^3}{12\mu r}\frac{\partial p}{\partial \theta} + \frac{r\omega h}{2} + \phi_s \frac{r\omega s}{2} \tag{5.43}$$

Hence, the average tangential velocity component across the film thickness is given by

$$\bar{v}_\theta = \frac{q_\theta}{h} = -\phi_\theta \frac{h^2}{12\mu r}\frac{\partial p}{\partial \theta} + \frac{r\omega}{2} + \phi_s \frac{r\omega s}{2h} \tag{5.44}$$

Equations 5.41 and 5.44 can be used to compute the flow fields under the disk. Figure 5.19 shows the Poiseuille and Couette flow lines under the disk due to pressure gradient and pad shear respectively. In the Poiseuille flow plot, most of the flow is inwards across the boundary except for some outflow at the trailing edge where the positive pressure region is located. In the Couette flow plot, the flow lines are following the rotation of the pad. Figure 5.20 shows the radial and tangential fluid pressure gradients respectively for Pad 2. Contours of zero pressure gradient are shown. From the plots, it can be seen that under only pressure flow, fluid will be sucked in around the leading edge of the disk and expelled at the trailing edge. This is depicted in Figure 5.19(a) previously. Results indicate that the Couette flow velocity is dominant over the Poiseuille flow velocity. This suggests that most of the slurry supply to different parts of the wafer or disk comes from slurry entrainment by the pad.

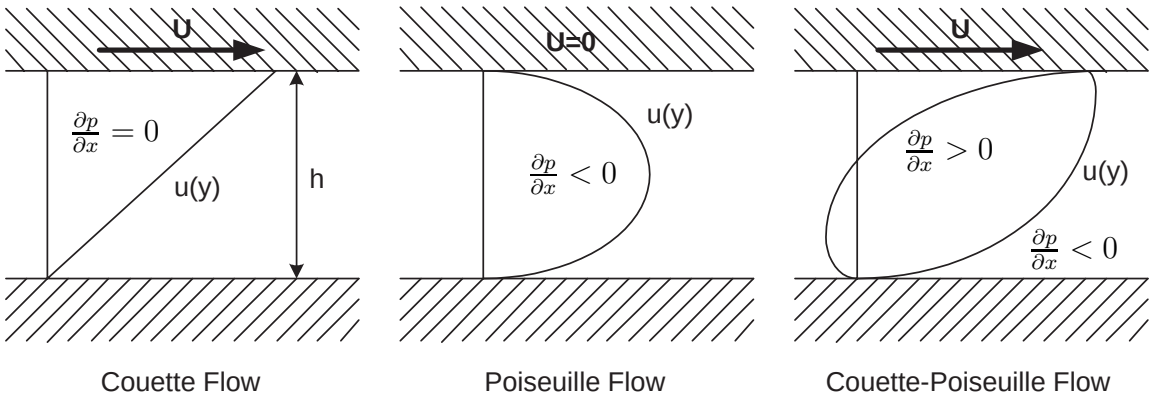

Figure 5.18: Plane unidirectional flow

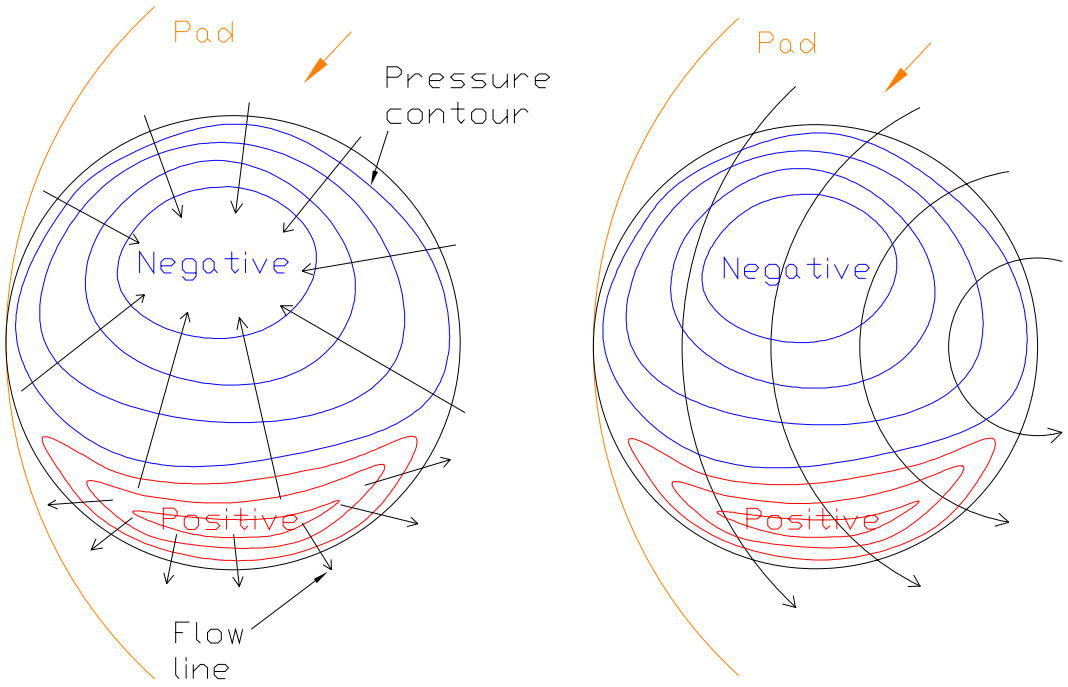

(a) Poiseuille flow

(b) Couette flow

Figure 5.19: Poiseuille and Couette flows

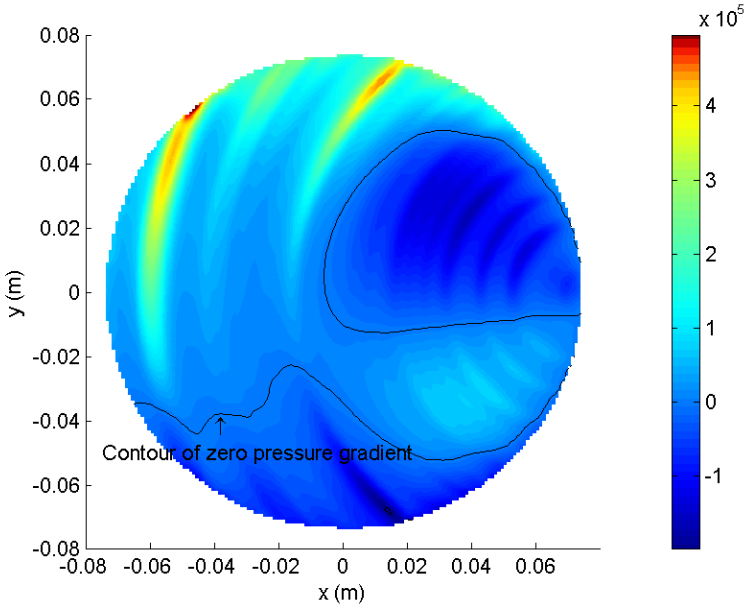

(a) Radial

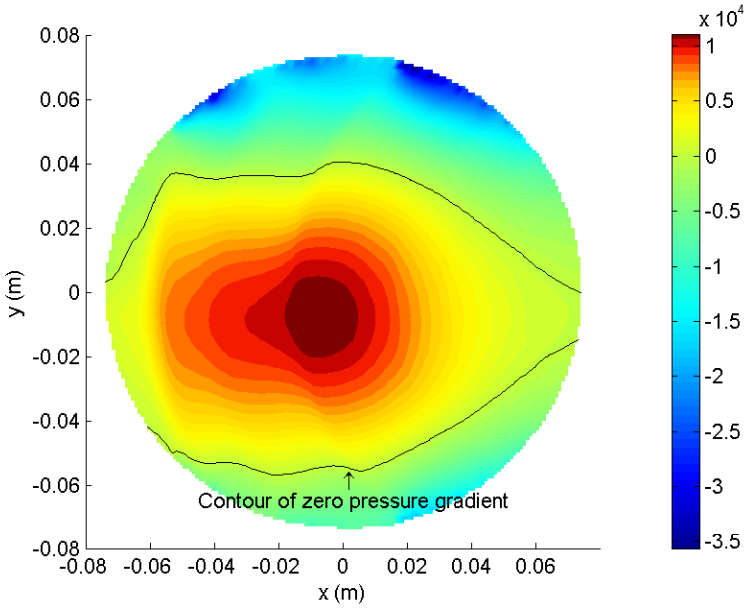

(b) Tangential

Figure 5.20: Fluid pressure gradients

5.7 Concluding Remarks

A mixed-lubrication model for predicting the fluid pressure during CMP has been developed. Experimental pressure results and model predictions show agreement in the distribution of pressure. Case studies of two pads treated differently showed that pad topography has a large effect on the distribution of fluid pressures. Ridges on the pad caused by either the conditioning or machining on a lathe can cause concentrations of fluid pressures. The difference in the results from the two pads is predicted by the model. Film thickness is a function of the orientation of the disk and the pad topography and has a high limit of about 30 μm. The contact pressure distribution is strongly affected by the ridges on the pad. Higher contact pressures occur on these ridges as the disk is resting on them. Contact pressures are also higher on the leading edge due to the forward tilting of the disk.

CHAPTER 6

MATERIAL REMOVAL RATE MODELING

The ultimate goal of CMP research is a single model that can predict the material removal rate distribution across the wafer. Due to the complexity of the process, the large number of variables, and the multidisciplinary approach required, few attempts have been made that covers a broad range of parameters. Most approaches are empirical and the most popular are the Prestonian models. The Preston equation [30] was derived from observations of glass polishing processes and was adopted for modeling CMP. The equation predicts that material removal rate is proportional both the pressure applied and pad velocity:

$$\text{Material removal rate} = k_p \text{ x Pressure x Velocity}$$

where k_p is the Preston constant that could be a function of all other input variables of the process. The Preston equation is essentially similar in form to the Archard wear equation [90]:

$$\text{Wear volume per unit sliding distance} = k_a \text{ x } \frac{Load}{Hardness}$$

where k_a is the dimensionless wear coefficient. The term k_a is often combined with the hardness to give the dimensional wear coefficient.

The Prestonian models included modifications to the original Preston equation. Based on Hertzian indentation of the abrasive into the wafer, Brown et al. [91]

suggested that the Preston constant can be expressed as 1/(2E) where E is the Young's modulus of the surface being polished. Zhao and Shi [46] proposed that for soft pads, a $P^{2/3}$ dependence should be used for the pressure to modify the Preston equation.

There are some models based on chemical removal. Hocheng et al. [92] modeled the removal rate based on chemical removal and shear flow. They proposed the removal rate increases with the increasing polishing speed and pressure to the power of 1/2. Zhao et al. [93] proposed a mathematical model based on the conversion of strongly bonded surface atoms/molecules to weakly bonded molecular species through chemical reaction while mechanical action delivers the energy needed to break the weakened bonds, thereby removing material at the molecular scale.

Luo et al. [33] and Zhao et al. [36] developed models based on mechanical abrasion. Both models postulated that abrasives caught in the tips of the asperities of the pad and the wafer were responsible for material removal from the wafer. Luo modeled the abrasive-wafer and abrasive-pad solid-solid contacts as plastic contacts while Zhao modeled elastic contact between pad and abrasives, and plastic contact between wafer and abrasives. Luo postulated that only the largest particles in the slurry take part in the material removal due to separation of the wafer and pad asperities. Zhao assumed no wafer and pad asperities separation. Both models predicted only the mean material removal and not the removal distribution across the wafer.

The model to be presented is based on mechanical abrasion and is able to compute the distribution of material removal across the wafer. One of the inputs is the distribution of contact pressure across the wafer, which can come from the fluid pressure model. Figure 6.1 shows the data flow for combining the fluid pressure and

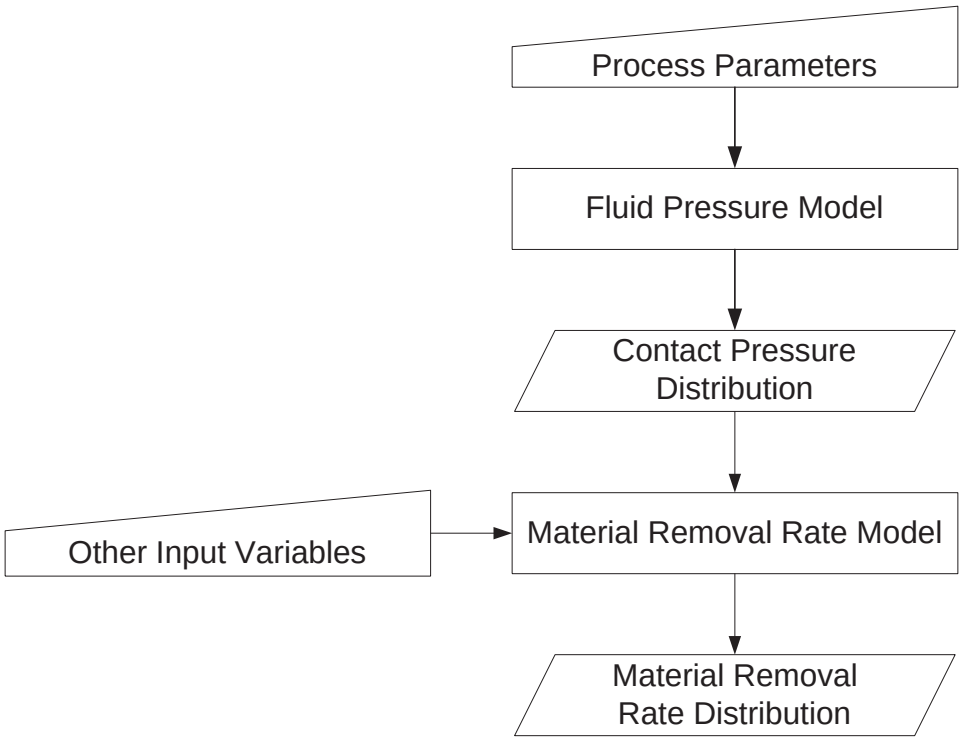

Figure 6.1: Fluid pressure and material removal rate models

material removal rate models.

6.1 The Abrasive Contact

The three-body contact between the wafer, abrasive and pad will change according to the relative hardnesses, the contact pressures and the abrasive concentration of the slurry. In this model, it is assumed that the abrasive particle is fully embedded into the pad due to its small size and the softness of the pad relative to the wafer. This model does not cover factors such as chemical effects, thermal effects, pad wear, and so on. The model is based on the assumptions of the abrasive wear theory that the abrasive indents and causes plastic deformation in the wafer. Material is removed when the abrasive contacts and slides relative to the pad. The abrasive-pad and wafer-pad contacts are modeled as elastic contacts. Assuming

that the abrasive particle is fully embedded into the pad asperity as illustrated in Figure 6.2, the indentation depths of the abrasive into the pad asperity and wafer, δ_{ap} and δ_{aw} respectively, are related by

$$\delta_{ap} = D - \delta_{aw} \tag{6.1}$$

By geometry, the contact radius at the abrasive-wafer interface is found to be

$$a_{aw} = \sqrt{D\delta_{aw} - {\delta_{aw}}^2} \tag{6.2}$$

As the pad is much softer than the wafer, most of the particle would be indented into the pad and the contact radius can be approximated by

$$a_{aw} \approx \sqrt{D\delta_{aw}} \text{ , since } \delta_{aw} \ll D \tag{6.3}$$

Every abrasive trapped at the wafer and pad asperity interface is subjected to a downward force due to the wafer and an upward force due to the pad asperity. The force acting on an abrasive due to the wafer assuming plastic deformation of the wafer is given by

$$W_1 = \frac{1}{2} H_w \pi {a_{aw}}^2 \tag{6.4}$$

where H_w is the hardness of the wafer.

The force acting on an abrasive due to the pad asperity assuming elastic deformation of the pad is given as

$$W_2 = \frac{4}{3}(\frac{D}{2})^{\frac{1}{2}} {E_{ap}}^* {\delta_{ap}}^{\frac{3}{2}} + \frac{\pi D^2}{4} p(r) \tag{6.5}$$

The first term on the right hand side of the equation accounts for the indentation by the abrasive into the pad asperity. The second term is the force due to the pad asperity that is already compressed by the wafer. Both terms are based on Hertzian indentation. The term p(r) is the Hertzian pressure at different locations on the asperity contact.

Using Hertz theory, the distribution of pressure at the asperity tip is given by

$$p(r) = \frac{2{E_{wp}}^{*}{\delta_{wp}}^{\frac{1}{2}}}{\pi {R_s}^{\frac{1}{2}}}\sqrt{1 - \frac{r^2}{{a_{wp}}^2}} \tag{6.6}$$

where

$${a_{wp}}^2 = \delta_{wp} R_s \tag{6.7}$$

The abrasive-pad and wafer-pad contact modulus can be approximated by

$${E_{ap}}^{*} \approx {E_{wp}}^{*} = \frac{E_p}{1 - {\nu_p}^2} \tag{6.8}$$

since the pad is much softer than the abrasive and wafer.

The term δ_{wp} can be computed if the contact pressure distribution over the wafer is known (e.g. from the fluid pressure model). Equating W_1 and W_2, substituting Eqn. 6.1, 6.3, 6.6, 6.7, and solving for δ_{aw} gives

$$\delta_{aw} = \frac{4\sqrt{2}}{3\pi}\frac{DE_p}{H_w(1 - {\nu_p}^2)} + \frac{DE_p{\delta_{wp}}^{\frac{1}{2}}}{\pi {R_s}^{\frac{1}{2}} H_w(1 - {\nu_p}^2)}\sqrt{1 - \frac{r^2}{\delta_{wp} R_s}} \tag{6.9}$$

By geometry, the cross-sectional area of interference between the abrasive and the wafer can be derived as

$$A = \frac{D^2}{4} sin^{-1}\left(\frac{2\sqrt{\delta_{aw}(D - \delta_{aw})}}{D}\right) - \left(\frac{D}{2} - \delta_{aw}\right)\sqrt{D\delta_{aw} - {\delta_{aw}}^2} \tag{6.10}$$

For $\delta_{aw} \ll D$

$$A \approx \delta_{aw}\sqrt{D\delta_{aw}} \tag{6.11}$$

Hence, the expectation of A taken over the contact area of the pad asperity tip, $E(A)$, is then given by

$$E(A) = \int_0^{2h_c}\int_0^{a_{wp}} A f_r(r) f_D(D) dr dD \tag{6.12}$$

where h_c is the central film thickness from the soft-EHL theory and will be covered in more detail in the next section. $f_r(r)$ is the probability density function associated with finding an abrasive at a radial distance, r, on the asperity tip. $f_r(r)$ could depend on many factors such as the size of the abrasive, etc. Here, $f_r(r)$ is assumed to scale with the circumference of a circle with radius r

$$f_r(r) = \frac{2r}{{a_{wp}}^2}\ ,\ 0 \le r \le a_{wp} \tag{6.13}$$

Typically, the abrasive diameter in a slurry follows the Gaussian function. Sometimes, the slurries are filtered to remove the largest abrasives that might cause defects during polishing so that the probability density function of abrasive diameter, $f_D(D)$, can be assumed to be a clipped Gaussian at 3 standard deviations from the mean at the upper bound

$$f_D(D) = \frac{1}{\sigma_D\sqrt{2\pi}} e^{-\frac{(D-D_m)^2}{2{\sigma_D}^2}} \tag{6.14}$$

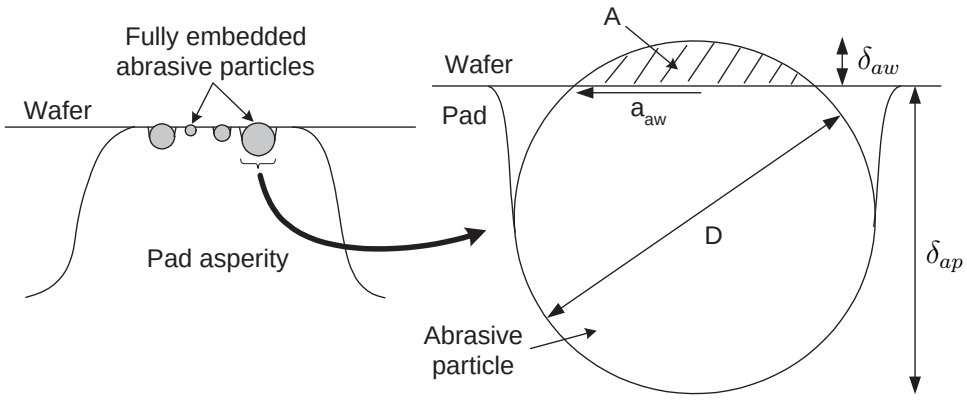

Figure 6.2: Three-body contact

6.2 Soft-EHL

Abrasives that are too large do not take part in the polishing as they could not get into the interface between the pad asperity and the wafer. Shan [61] suggested that only abrasives with diameters that are 1-2 times the central film thickness, h_c, take part in the polishing. While it is still not clear how large abrasives are filtered out from the interface, h_c from the soft-EHL theory could be useful in setting this upper limit. As the abrasive size increases, the probability that the abrasive could get trapped at the interface should decrease. In this model, for simplicity, abrasives that are 2 times h_c are filtered out from taking part in the polishing. The central film thickness for low-elastic-modulus materials (soft-EHL), elliptical conjunctions as obtained from Hamrock and Dowson (1978), is given by

$$h_c = H_c R_s \tag{6.15}$$

where H_c is the dimensionless central film thickness

$$H_c = 7.32(1 - 0.72e^{-0.28k_e})U^{0.64}W^{-0.22} \tag{6.16}$$

k_e is the ellipticity parameter and assumed to be 1 for circular contacts. The dimensionless speed parameter is given by

$$U = \frac{V\mu}{E'_{wp}R_s} \tag{6.17}$$

where V is the velocity, μ is the viscosity of the liquid and E'_{wp} is the effective modulus of elasticity

$$E'_{wp} = \frac{2E_p}{1-\nu_p^2} \tag{6.18}$$

The dimensionless load parameter is given by

$$W = \frac{w_z}{E'_{wp}R_s^2} \tag{6.19}$$

where w_z is the normal load component.

6.3 Number of Abrading Particles

The mass fraction of abrasives in the slurry is defined as

$$c_m = \frac{m_a}{m_a + m_s} \tag{6.20}$$

where m_a and m_s are the masses of abrasive and liquid in the slurry respectively.

Hence, the volume fraction of abrasive in the slurry is given by

$$c_v = \frac{m_a\rho_s}{m_a\rho_s + m_s\rho_a} \tag{6.21}$$

where ρ_a and ρ_s are the densities of the abrasive and the liquid in the slurry respectively.

The volume fraction of abrasive in the slurry can be related to its mass fraction by

$$c_v = \frac{\rho_s c_m}{\rho_s c_m + \rho_a - \rho_a c_m} \tag{6.22}$$

Assuming a cube of slurry with abrasives that are evenly distributed. The number of abrasives per unit length on each side of the cube is (n/l) where l is the length of each side of the cube and n is the number of abrasives along that side. The volume fraction of abrasives in the slurry can be written as

$$c_v = (\frac{n}{l})^3 v_a \tag{6.23}$$

where the average volume of an abrasive is

$$v_a = \frac{\pi}{6} \int_0^{D_m + 3\sigma_D} D^3 f_D(D) dD \tag{6.24}$$

For a single layer of abrasives, the number of abrasives per unit area is given by $(n/l)^2$.

Hence, the number of abrading particles per unit area at the wafer and pad interface can be related to the volume fraction of abrasives in the slurry and the average volume of the abrasive as

$$n_a = (\frac{c_v}{v_a})^{2/3} \int_0^{2h_c} f_D(D) dD \tag{6.25}$$

The number of abrading particles is given by

$$N_a = A_r n_a \tag{6.26}$$

where A_r is the real area of wafer-pad contact. The ratio of real to nominal area of wafer-pad contact is given by

$$\frac{A_r}{A_n} = \pi \eta R_s \int_d^{\infty} (z-d)\phi_z(z)dz \tag{6.27}$$

6.4 Material Removal

Figure 6.3 illustrates the kinematics of the process. The wafer-pad relative velocity in cylindrical polar coordinates with the origin at the wafer center can be derived as

$$v_{wp} = \sqrt{(\omega_p - \omega_w)^2 r^2 sin^2\theta + [(\omega_w - \omega_p)rcos\theta + \omega_p x_c]^2} \tag{6.28}$$

In the abrasion model, the indenter will cut out a groove of material from the workpiece. The volumetric removal will be the cross-sectional area of interference between the indenter and the workpiece multiplied by the distance travelled by the indenter. Therefore, the volumetric removal rate by a single abrasive can be computed by $E(A)$ x v_{wp}. The total number of active abrasives is given by A_r x n_a.

Hence, the thickness removed per unit time at any location on the wafer is given by

$$t_{mr} = k_{mr} \frac{A_r}{A_n} n_a E(A) v_{wp} \tag{6.29}$$

where k_{mr} encompasses factors such as the probability of material breaking free from the wafer, fraction of abrasives that are rolling, thermal effects, chemical effects, and so on. Studies [90, 94] have shown that the predicted abrasive wear coefficient for 2-body abrasion is about one order of magnitude higher than measured. For 3-

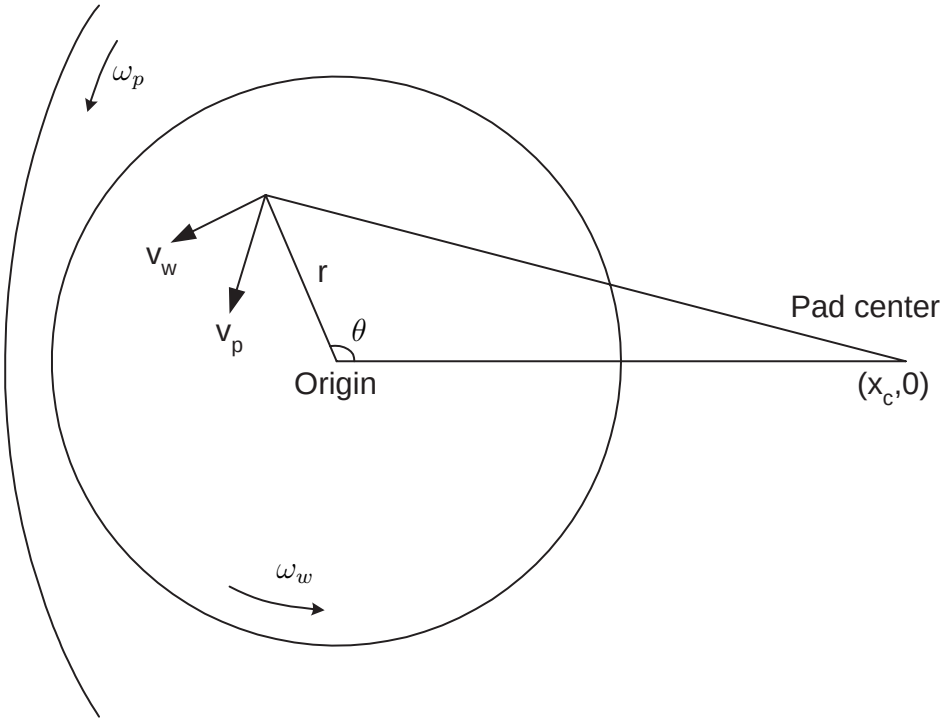

Figure 6.3: Wafer-pad relative velocity

body abrasion, it is about 2 orders of magnitude higher than measured. The value for k_{mr} is obtained by fitting to one set of experimental results. A value of 0.005 for k_{mr} is fixed for all simulations.

Finally, the thickness removed as a function of wafer radius with rotational averaging is given by

$$t_{mr}(r) = \frac{1}{2\pi} \int_0^{2\pi} t_{mr} d\theta \tag{6.30}$$

6.5 Results and Discussion

The results from this model are compared to the polishing of thermally grown silicon oxide film on 100 mm single crystal silicon wafers. Polishing was conducted on the same polisher as that in the fluid pressure measurements for a variety of load,

pad speed, abrasive size and mass fraction of abrasive. A grooved pad was used in the experiments which meant that there was no sub-ambient fluid pressure. Hence, the material removal rate model did not include fluid pressure. Relative velocity was integrated over the wafer to obtain a mean velocity.

Figure 6.4 shows the material removal rate versus PV from the experiments and from the model for 80 nm abrasives and abrasive mass fraction of 0.3. The Preston fits for both the experimental and model data are also presented. Individual data points for both cases show some deviations from the Preston fitted lines. While the model could not predict the locations of each data point, the trendline is similar to the experimental data. Both results seem to agree with the Preston relation. Figure 6.5 shows a typical predicted material removal rate versus down pressure for a pad linear velocity of 1.2 m/s. The increase in material removal rate with down pressure is mainly due to the increase in real contact area between the wafer and the pad. This results in an increase in the number of "active" abrasives. In which case, the material removal rate has a $P^{0.9}$ dependence. Figure 6.6 shows the predicted material removal rate versus the pad linear velocity at a down pressure of 19 kPa. Except for the lowest velocity, the curve follows the Preston relation well.

Figure 6.7 shows the material removal rate versus abrasive size from the experiments and the model. The experimental plots show peaks in the material removal rate for three different combinations of down pressure and linear velocity. The peaks occurred at an abrasive size of 80 nm. Reducing or increasing the abrasive size will result in a decrease in the material removal rate. Increases in pressure and velocity result in higher material removal rates. Bielmann et al. [95] reported a decrease in the polishing rate of tungsten when the abrasive size was increased. Alumina particles of similar phase and shape with size varying from 0.1 to 10 μm diameter

were used in the experiments. Luo et al. [33] predicted that there exists a minimum in material removal rate in the region of 40-100 nm. They rationalized this result as follows: for abrasive sizes smaller than some minimum, decreasing the abrasive size yields a larger material removal rate because the total number of active abrasives is larger. For abrasive sizes larger than the minimum, decreasing the abrasive size, however, yields a lower material removal rate because the probability of active abrasives becomes smaller, offsetting the effect of the total number of active abrasives.

While the model results in Figure 6.7 can predict peaks in material removal rates for all three cases, these were not as "sharp" as those seen in the experiments. The peaks occurred at 70 to 85 nm which is close to the 80 nm in the experiments. The decrease in material removal rate at larger abrasive sizes is also much steeper than observed in the data. The experimental trends can be attributed to the number of abrading particles and the expected indentation of the abrasive into the wafer. Figure 6.8 shows the expected abrasive-wafer cross-sectional area of interference versus abrasive size for the case at 18 kPa down pressure and 0.4 m/s linear velocity. At small mean abrasive sizes, most of the abrasives in the distribution are active in polishing the wafer since they are smaller than the central film thickness. The expected abrasive-wafer cross-sectional area of interference, E(A), would be small. As the abrasive size increases, E(A) increases since a large portion of the active abrasives has shifted to larger abrasive sizes. On the right end of the plot at the decreasing slope, most of the abrasives in the slurry have exceeded the central film thickness size. The active abrasives are those on the lower end of the abrasive size distribution. The distribution of abrasive sizes of these active abrasives is more uniform and less skewed towards h_c which results in the decrease in E(A). Figure 6.9

shows the area density of the number of abrading particles versus abrasive size. As the abrasive size increases, the number of abrading particles per unit area decreases due to the filtering effect caused by h_c. For a fixed mass fraction of abrasive in the slurry, the number of abrasives is also expected to decrease with increasing abrasive size.

Figure 6.10 shows the material removal rate versus the mass fraction of abrasive in the slurry from the experiments and from the model. A down pressure of 32 kPa and a pad linear velocity of 0.6 m/s were used. The data shows increases in material removal rate as the mass fraction of abrasive is increased which is due to the increase in the number of abrading particles per unit area. There is a slight deviation from linearity in the curves. The shapes of the curves from the model are similar to that in the experiment. The 140 nm (Model) curve gave a much lower prediction due to the sharp drop in material removal rate for large abrasive size as seen in Figure 6.7.

Figure 6.11 shows the predicted material removal rate versus the hardness of the wafer and demonstrates that the material removal rate increases as the wafer material gets softer, which is understandable for an indentation-based model. Typical indentation depths of the abrasive into the wafer are 1-10 angstroms which is of the same order of average roughnesses measured on the polished wafers.

Figure 6.12 shows the predicted material removal rate versus the elastic modulus of the pad. It is seen that the material removal rate increases as the pad material gets stiffer. This increase in material removal rate can be understood in terms of the increase in contact force between the abrasive particle and the pad. This leads to an increase in the indentation depth of the abrasive, resulting in a higher removal rate. As presented in Chapter 2, contradictory results have been reported with regard to the effect of pad modulus on the material removal rates. This is due to the difference

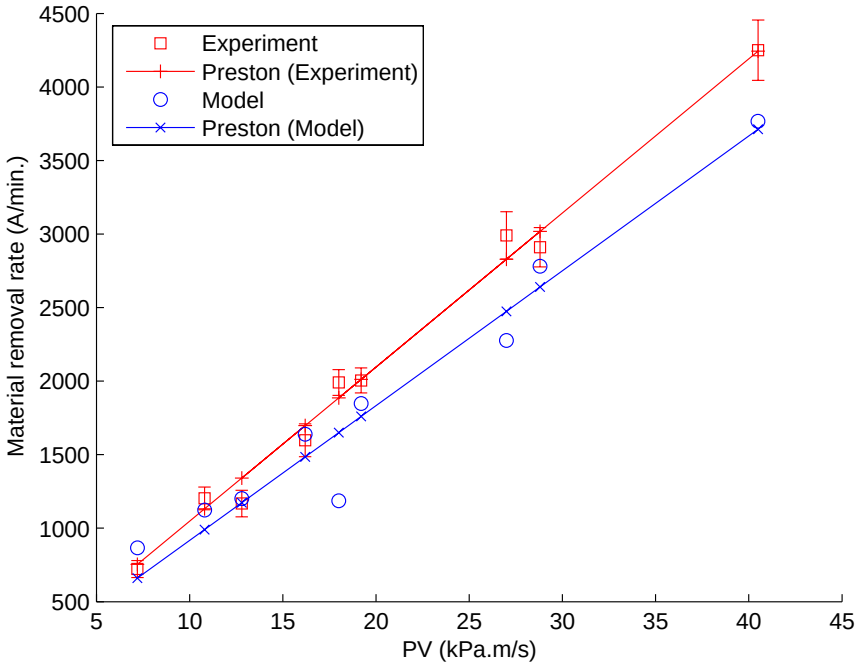

Figure 6.4: Predicted material removal rate versus PV

in the morphology and structure of the pads used.

6.5.1 Material removal rate with suction pressure.

The difference in material removal rates with and without taking into account negative fluid pressures are compared. The fluid pressure model is run to generate contact pressure maps with and without the fluid pressures. These two contact pressure maps are then fed into the material removal rate model to generate the removal rate distribution. Figure 6.13 shows the comparison for the two cases both at a 2.8 kPa downpressure and a 1.2 m/s linear velocity. Both curves show similar trends having higher removal rates towards the edge of the wafer. This is due to the tilt of the wafer, generating higher contact pressures at the wafer edge. The curve taking into account suction pressure is shifted to higher material removal rates relative to that without suction. In addition, the difference in material removal rates

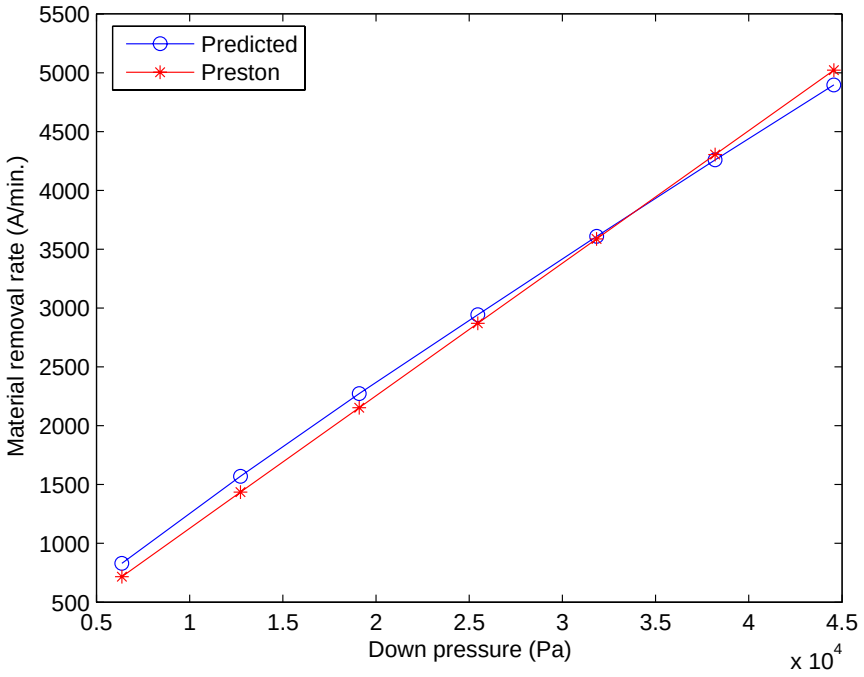

Figure 6.5: Predicted material removal rate versus down pressure for a pad linear velocity of 1.2 m/s

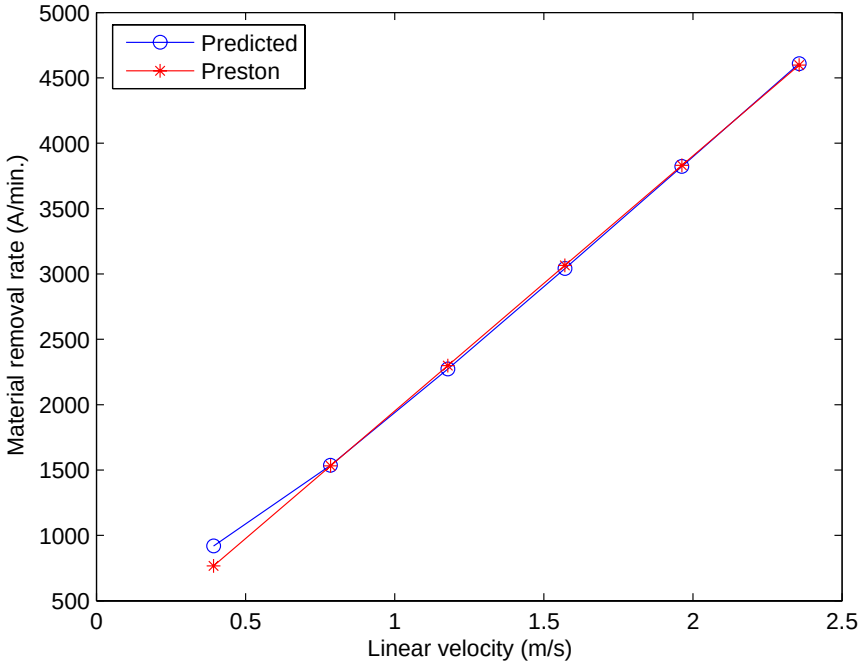

Figure 6.6: Predicted material removal rate versus pad linear velocity for a down pressure of 19 kPa

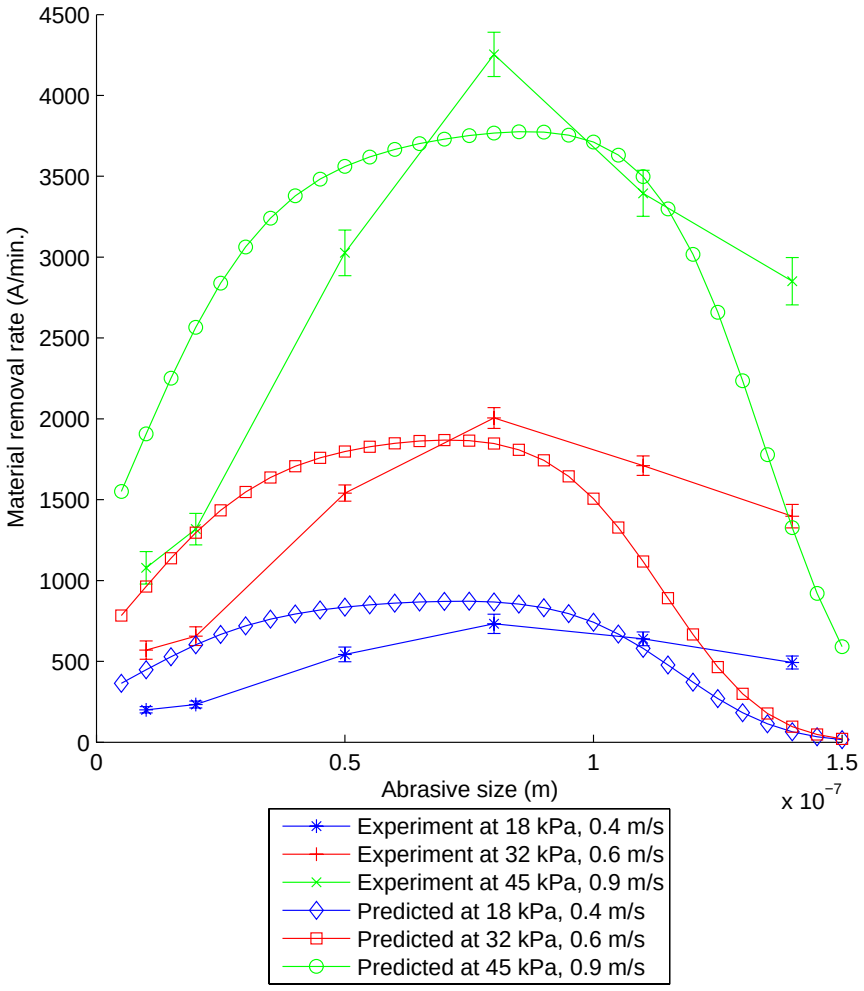

Figure 6.7: Experimental and predicted material removal rate versus abrasive size

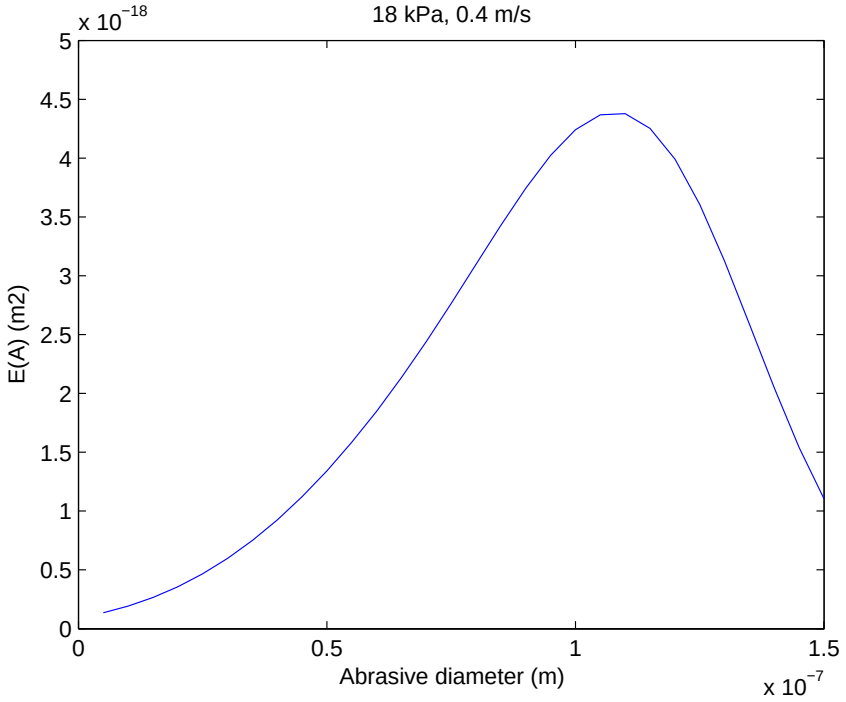

Figure 6.8: Expected abrasive-wafer cross-sectional area of interference versus abrasive size

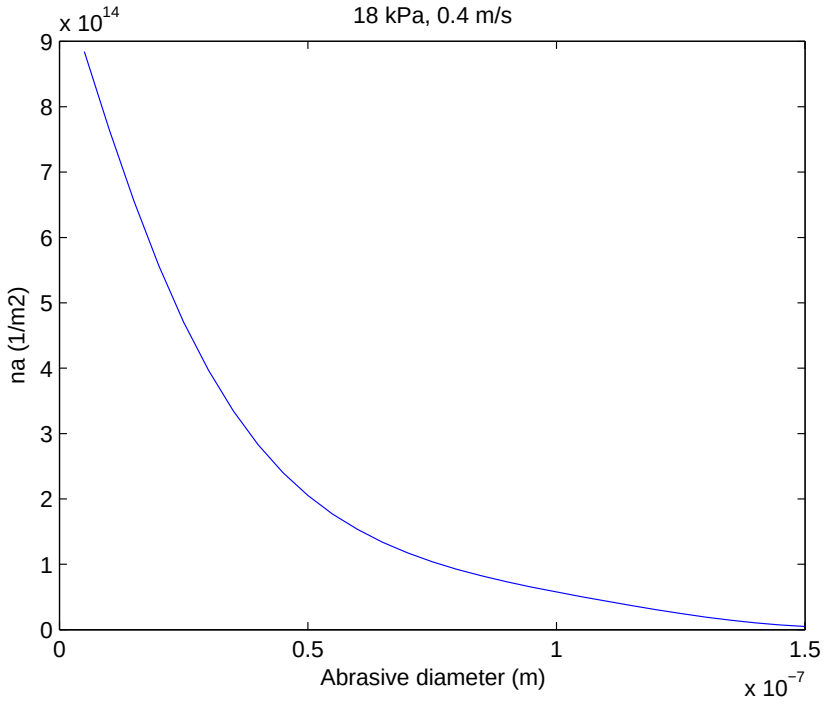

Figure 6.9: Area density of the number of abrading particles versus abrasive size

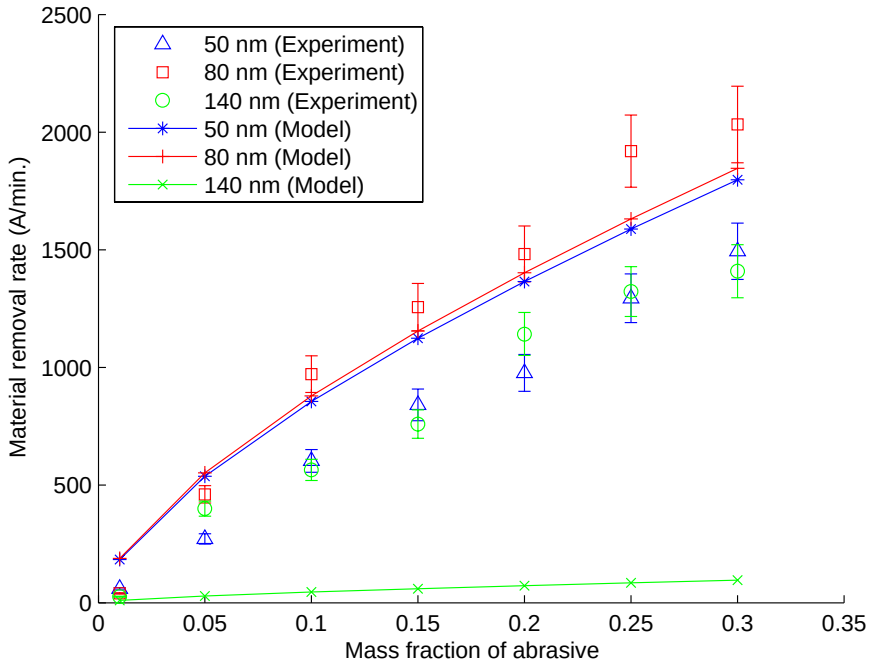

Figure 6.10: Predicted material removal rate versus mass fraction of abrasive for a down pressure of 32 kPa and a pad linear velocity of 0.6 m/s

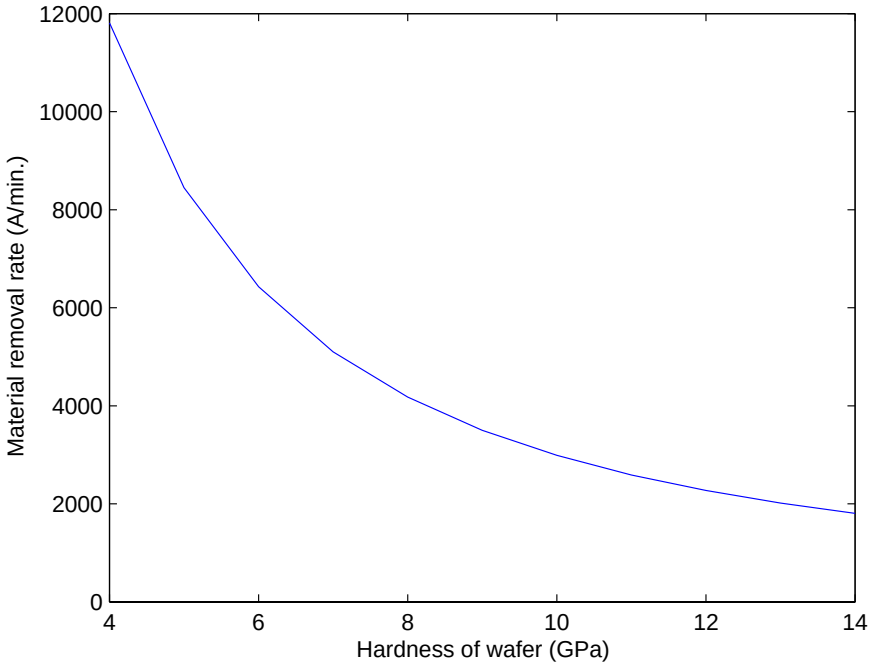

Figure 6.11: Predicted material removal rate versus hardness of the wafer

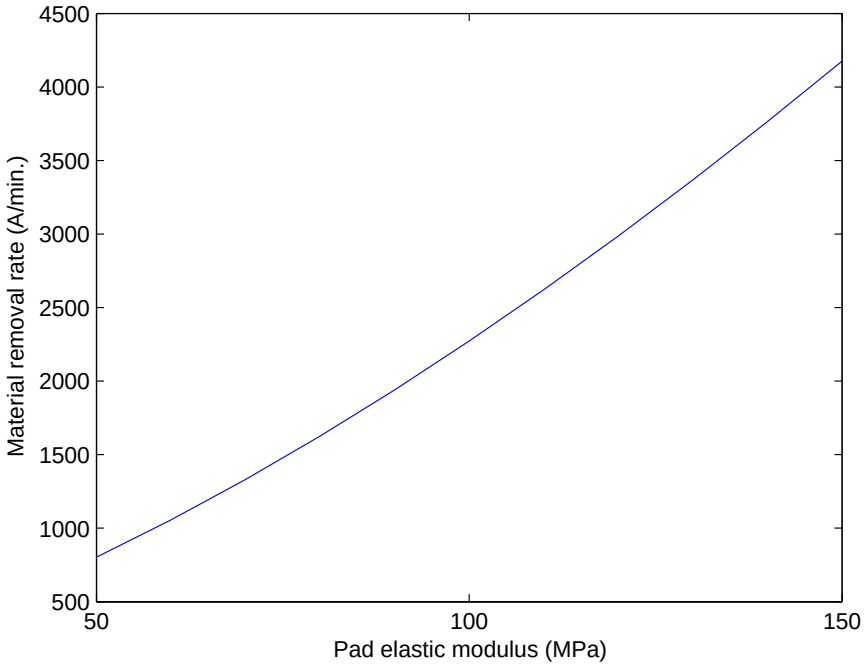

Figure 6.12: Predicted material removal rate versus elastic modulus of the pad

in the central region of the wafer is larger than at the edges. The material removal rate is about 50 percent higher with suction than without suction, at the central region of the wafer. The higher material removal rate with suction is due to the added contact pressure as a result of the suction pressure when the wafer is pulled into closer contact with the pad. As pad linear velocity is increased, this effect would be more pronounced as the gap between the two curves widen.

The prediction of material removal rate as a function of pad velocity is shown in Figure 6.14. The data takes into account suction pressure and uses the Pad 2 topography. In contrast to the result for grooved pad in Figure 6.6, the relation is nonlinear or non-Prestonian. As pad velocity increases, the data shows higher material removal rate than the Prestonian model. This is due to the increasing contribution of the suction pressure to the contact pressure as the pad velocity is

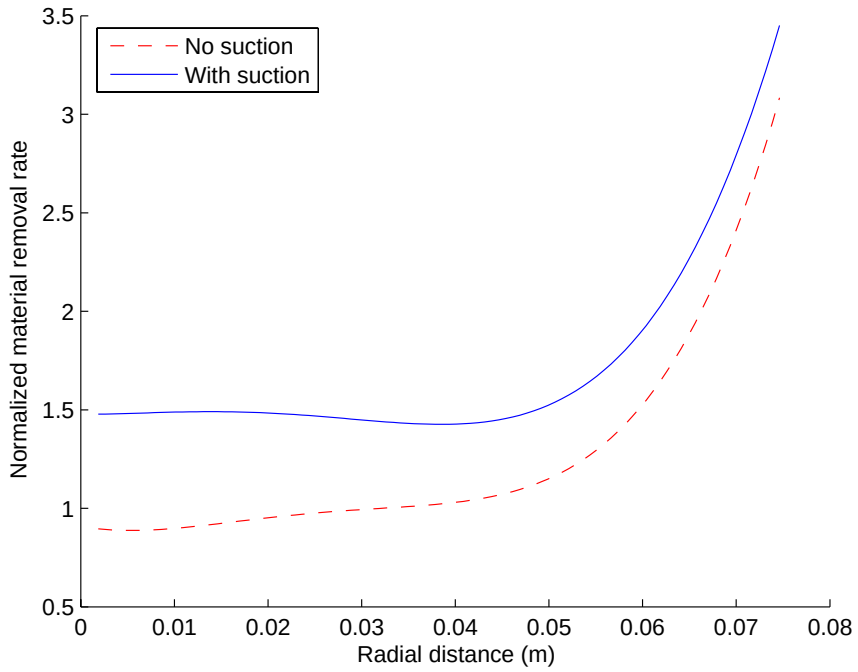

Figure 6.13: Normalized material removal rates with and without suction pressure

increased. Figure 6.15 shows oxide polishing data using plain IC1000 pad exhibiting similar trend.

6.6 Concluding Remarks

A material removal rate model based on mechanical abrasion has been developed. This model provides insight into the process by looking into the physics of the parameters inferred in the Preston's constant. Although thermal, chemical and other effects are not taken into account, the model can predict some of the results from the polishing experiments. Using the central film thickness from EHL-theory as a filter for large abrasives, the model is able to predict the peak in material removal rate as a function of abrasive size seen in the experiments. The load and speed dependence of the material removal rate are predicted by the model. The material

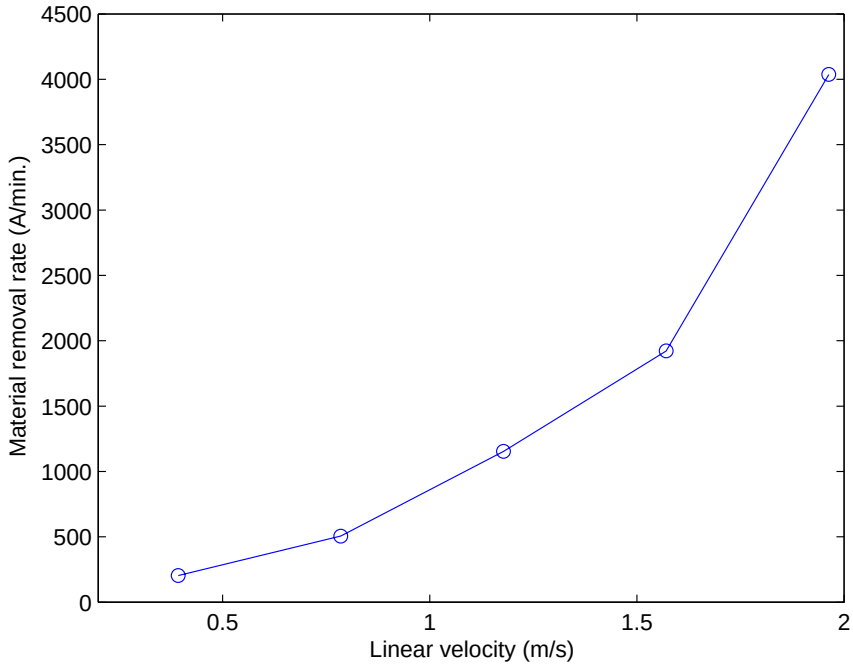

Figure 6.14: Predicted material removal rate versus pad linear velocity for a down pressure of 3 kPa (Pad 2, 150 mm wafer)

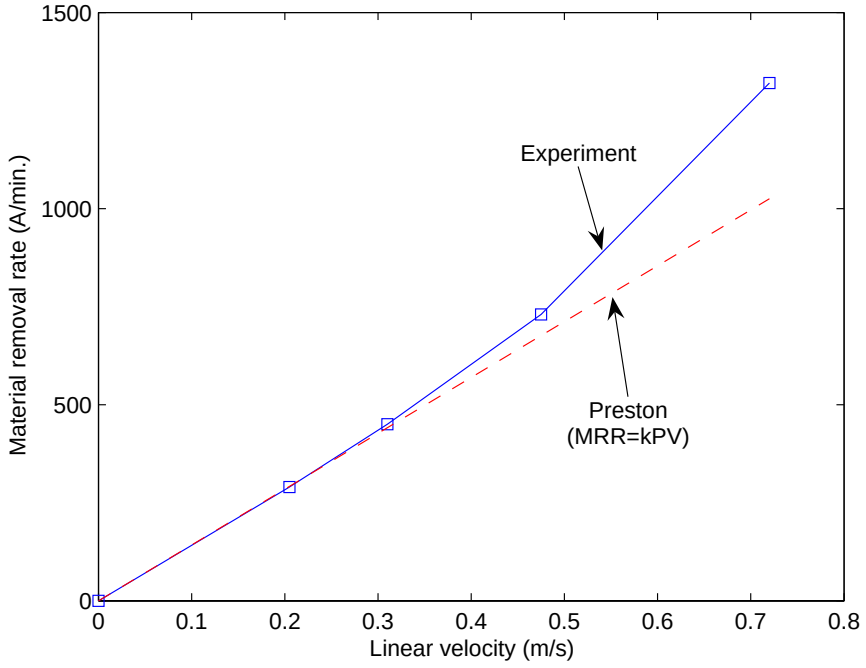

Figure 6.15: Material removal rate versus pad linear velocity from oxide polishing experiments using plain IC1000 pad

removal rate taking into account the negative fluid pressure is higher than if there is no negative fluid pressure. Hence, for a plain pad where negative pressures will form, it is required that fluid pressures are accounted for as it will affect the contact pressure distribution. Pad velocity dependence of the material removal rate taking into account suction pressure is nonlinear or non-Prestonian due to the additional contact pressure caused by the suction effect. Discrepancies in the predicted and measured data are due to other effects not incorporated into the model.

CHAPTER 7

CONCLUSIONS

The fluid pressure phenomenon seen in the sliding of a flat and smooth disk/wafer against a rough pad has been investigated experimentally and numerically. A model based on contact mechanics, fluid mechanics, and force and moment balance of the disk/wafer has been developed. Experimental and model results show agreement. In addition, a material removal rate model based on mechanical abrasion has been developed and compared to polishing results. The conclusions of this research are listed below.

- A finite element analysis on the static contact situation between a rigid, flat punch and an elastic flat showed that for the configuration seen in CMP where the contact area is many times larger than the thickness of the pad, the contact pressure distribution is essentially uniform throughout the contact area except for the 1-2 mm region at the periphery. In this region, there exists a peak in contact pressure due to the corner of the punch. Hence, this phenomenon alone would not cause a gradient in the film thickness across the disk/wafer. As the thickness of the pad approaches the size of the contact area, the contact pressure approaches the non-linear distribution seen in Figure 1.6.

- A finite element model for the static contact situation in a typical CMP configuration has been developed. The configuration is a structural layer consisting of the wafer carrier, carrier film, wafer and the pad. Contact pressure result

is similar to the situation involving the rigid, flat punch and the elastic flat: uniform contact pressure except at the periphery. In addition, wafer bowing is minimal ($\approx 0.14\ \mu m$) and occurs only at the wafer periphery. This is verified by experimental result from the static compression tests using the same configuration. The experimental result suggests that the amount of wafer bowing is not detected for the range of loads typically used in CMP. Although the peak contact pressure at the wafer periphery causes a bending moment, it is not sufficient to cause significant wafer bowing due to the large contact area involved. Hence, very minimal wafer bowing is seen and is localized at the wafer periphery. In addition, due to this localized wafer bowing, a ring of high von Mises stress is seen 4 mm from the wafer periphery. This is caused by the peak seen in the radial stress. The location of this peak in radial stress coincides with the peak in material removal seen in oxide polishing. The contact stress peak, on the other hand, happens at 100 μm from the wafer periphery and cannot be directly responsible for this peak in removal.

- Pad soaking experiments on the IC1000 pad have shown that the penetration of water is limited only to the surface of the pad. This is due to the closed-cell structure and impermeability of the pad material to water. The experiments show that the pad weight is rapidly increasing in the first few hours of soaking and reaches stability at about 100 hours. Most of the water fill up the voids in the first 2 void layers of the pad. A smaller amount of water is believed to have penetrated the pad material altering its properties. It can be concluded that there is no large scale mass flow of water into the pad.

- Fluid pressure mapping revealed that sub-ambient pressure occupies about

70 percent of the area under the disk, mainly in the leading edge and central regions. Positive pressure exists at the trailing edge. The most negative pressure is skewed towards the leading edge and slightly towards the center of the pad. The location of the most positive pressure is close to the trailing and skewed towards the center of the pad. Both negative and positive fluid pressures increase in magnitudes as pad speed is increased. For such patterns of pressure distribution to occur, there has to be a diverging film thickness gap at the leading edge and a converging film thickness gap at the trailing edge as fluid flows along the constant velocity lines. Disk tilt experiments revealed that the disk is leaning towards the leading edge and towards the center of the pad. The tilting occurs due to the shear of the pad on the bottom face of the disk; and the gimbaled joint of the disk allows it to do so. This direction of tilt creates the necessary condition for negative and positive pressures to form. Pad topography is found to have a huge effect on the film thickness since variation in pad profile is in the tens of microns, the same order of magnitude as the film thickness. Concentric ridges on the pad can affect the tilt of the disk with respect to the pad, altering the film thickness distribution. The ridges also cause positive and negative pressure concentrations due to the lower film thicknesses.

- The amount of wafer bowing in a typical dynamic CMP configuration is less than 2 μm. This shows that the wafer is much stiffer than thought. Wafer tilting with respect to the wafer carrier is also detected. Carrier film compression is higher at the leading edge and slightly towards the center of the pad. The difference in carrier film compression between the leading and trailing

edge is 5-7 μm. This phenomenon can be explained by the tilting of the wafer carrier towards the leading and inner edges resulting in the higher contact pressures there. The amount of wafer carrier tilt ranges from 20 to 40 μm and is dominating over the wafer bow and wafer tilt. Hence, the fluid pressure phenomenon should still exist in this configuration although the magnitudes might be different.

- A statistical material removal rate model based on mechanical abrasion has been developed. The model is able to compute the material removal rate distribution across the wafer based on the contact pressure distribution which can come from the fluid pressure model, and based on the relative velocity distribution. Down pressure dependence shows slight deviation from linearity. The increase in material removal rate with down pressure is mainly due to the increase in real contact area between the wafer and the pad, leading to an increase in the number of active abrasives. Pad velocity dependence of the material removal rate is linear for a grooved pad that does not generate sub-ambient pressure. The peak in material removal rate as a function of abrasive size seen in the polishing experiments is predicted by the model. There exists an optimal abrasive size whereby material removal rate is highest. For abrasive sizes smaller than this optimal size, decreasing the abrasive size would result in E(A) decreasing since the mean abrasive size is decreasing. This effect is dominant over the increase in the number of active abrasives, resulting in the lowering of material removal rate. At abrasive sizes larger than the optimal size, increasing the abrasive size would result in a decrease in E(A) and a decrease in the number of active particles due to the filtering effect that larger

abrasives could not get into the interface between the pad asperity tips and the wafer. For a fixed mass fraction of abrasive in the slurry, increasing abrasive size also leads to a decrease in the number of active particles. The effect of mass fraction of abrasive in the slurry on the material removal rate is also predicted by the model and is similar in trend with the experiments. Improvements to this model include a more rigorous modeling of the contact between the wafer, abrasive and the pad, incorporating chemical and thermal effects, and a more accurate method of determining the filter size for large abrasives.

REFERENCES

[1] T.K. Dot, T. Kasai, and H.K. Tonshoff. Lapping and polishing. In I.D. Marinescu, H.K. Tonshoff, and I. lnasaki, editors, *Handbook of Ceramic Grinding and Polishing*, pages 354–442. Noyes Publications/William Andrew Publishing, Norwich, 2000.

[2] P.S. Sreejith, G. Udupa, Y.B.M. Noor, and B.K.A. Ngoi. Recent advances in machining of silicon wafers for semiconductor applications. *Int. J. Adv. Manuf. Technol.*, 17:157–162, 2001.

[3] S.H. Li and R.O. Miller. *Chemical Mechanical Polishing in Silicon Processing*, volume 63 of *Semiconductors and Semimetals*. Academic Press, San Diego, CA, 2000.

[4] C.L. Borst, W.N. Gill, and R.J. Gutmann. *Chemical-Mechanical Polishing of Low Dielectric Constant Polymers and Organosilicate Glasses*. Kluwer Academic Publishers, Norwell, MA, 2002.

[5] K.L. Johnson. *Contact Mechanics*. Cambridge University Press, Cambridge, U.K., 1985.

[6] J.A. Greenwood and J.B.P. Williamson. Contact of nominally flat rough surfaces. *Proc. R. Soc. Lond.*, A295:300–319, 1966.

[7] S.R. Runnels and L.M. Eyman. Tribology analysis of chemical-mechanical polishing. *J. Electrochem. Soc.*, 141(6):1698–1701, 1994.

[8] L.M. Cook, J.F. Wang, D.B. James, and A.R. Sethuraman. Theoretical and practical aspects of dielectric and metal cmp. *Semiconductor International*, 18(13):141–143, 1995.

[9] L.M. Cook. Chemical processes in glass polishing. *J. of Non-Crystalline Solids*, 120:152–171, 1990.

[10] M. Tomozawa. Oxide cmp mechanisms. *Solid State Technology*, 40(7):169–175, 1997.

[11] M. Tomozawa and K. Hirao. Diffusion of water into oxides during microhardness indentation. *Journal of Materials Science Letters*, 6:867–868, 1987.

[12] M. Nogami and M. Tomozawa. Effect of stress on water diffusion in silica glass. *Journal of the American Ceramic Society*, 67(2):151–154, 1984.

[13] F.B. Kaufman, D.B. Thompson, R.E. Broadie, M.A. Jaso, W.L. Guthrie, D.J. Pearson, and M.B. Small. Chemical-mechanical polishing for fabricating patterned w metal features as chip interconnects. *J. Electrochem. Soc.*, 138(11):3460–3465, 1991.

[14] J.M. Steigerwald, S.P. Murarka, and R.J. Gutmann. *Chemical Mechanical Planarization of Microelectronic Materials*. John Wiley and Sons Inc., New York, 1997.

[15] C.W. Liu, B.T. Dai, and C.F. Yeh. Chemical mechanical polishing of psg and bpsg dielectric films: the effect of phosphorus and boron concentration. *Thin Solid Films*, 270:607–611, 1995.

[16] S.C. Kuiry, S. Deshpande, M. Klimov, Y. Obeng, and S. Seal. Chemical-mechanical planarization of copper: Role of oxidant and inhibitor. In *Proceedings of the 6th International Symposium on Chemical Mechanical Planarization*, volume 21, pages 52–60, Orlando, FL, 2003. The Electrochemical Society, Inc.

[17] R. Baker. The origin of edge effect in chemical mechanical planarization. In *ECS Fall Meeting*, San Antonio, TX, 1996.

[18] Y. Zhang, P. Parikh, B. Stephenson, M. Bonsaver, J. Ling, and M. Li. Effect of peteos film stress on chemical mechanical planarization. In *VMIC Conference*, 1996.

[19] W. Tseng, Y. Wang, and J. Chin. Effects of film stress on the chemical mechanical polishing process. *Journal of the Electrochemical Society*, 146(11):4273–4280, 1999.

[20] M.S. Haque, H.A. Naseem, and W.D. Brown. Correlation of stress behavior with hydrogen-related impurities in plasma-enhanced chemical vapor deposited silicon dioxide films. *Journal of Applied Physics*, 82(6):2922–2932, 1997.

[21] J. McGrath, C. Davis, and J. McGrath. The effect of thin film stress levels on cmp polish rates for peteos wafers. *Journal of Material Processing Technology*, 132:16–20, 2003.

[22] D. Wang, J. Lee, K. Holland, T. Bibby, S. Beaudoin, and T. Cale. Von mises stress in chemical-mechanical polishing processes. *J. Electrochem. Soc.*, 144(3):1121–1127, 1997.

[23] C.S. Murthy, D. Wang, S.P. Beaudoin, T. Bibby, K. Holland, and T.S. Cale. Stress distribution in chemical mechanical polishing. *Thin Solid Films*, 308-309:533–537, 1997.

[24] D.C. Mejia, A. Perlov, and S. Beaudoin. Qualitative prediction in sio2 removal rates during chemical mechanical polishing. *J. Electrochem. Soc.*, 147(12):4671–4675, 2000.

[25] T. Park, T. Tugbawa, J. Yoon, D. Boning, J. Chung, R. Muralidhar, S. Hymes, Y. Gotkis, S. Alamgir, R. Walesa, L. Shumway, G. Wu, F. Zhang, R. Kistler, and J. Hawkins. Pattern and process dependencies in copper damascene chemical mechanical polishing processes. In *VLSI Multilevel Interconnect Conference (VMIC)*, Santa Clara, CA, 1998.

[26] J. Warnock. A two-dimensional process model for chemimechanical polish planarization. *Journal of the Electrochemical Society*, 138(8):2398–2402, 1991.

[27] D. Boning, B. Lee, C. Oji, D. Ouma, T. Park, T. Smith, and T. Tugbawa. Pattern dependent modeling for cmp optimization and control. In *Mat. R. Soc. Symp. Proc.*, volume 566, pages 197–209, San Francisco, CA, 2000.

[28] D.O. Ouma, D.S. Boning, J.E. Chung, W.G. Easter, V. Saxena, S. Misra, and A. Crevasse. Characterization and modeling of oxide chemical-mechanical polishing using planarization length and pattern density concepts. *IEEE Trans. on Semiconductor Manufacturing*, 15(2):232–244, 2002.

[29] L. Yang. Modeling cmp for copper dual damascene interconnects. *Solid State Technology*, 43(6), 2000.

[30] F.W. Preston. The theory and design of plate glass polishing machines. *J. Soc. Glass Technol.*, 11:214–217, 1927.

[31] W.G. Sawyer. Surface shape and contact pressure evolution in two component surfaces: Applications to copper chemical mechanical polishing. *Tribology Letters*, 17(2):139–145, 2004.

[32] J.J. Vlassak. A contact-mechanics based model for dishing and erosion in chemical-mechanical polishing. *Mat. R. Soc. Symp. Proc.*, 671:M4.6.1–M4.6.6, 2001.

[33] J. Luo and D.A. Dornfeld. Material removal mechanism in chemical mechanical polishing: Theory and modeling. *IEEE Trans. on Semiconductor Manufacturing*, 14(2):112–133, 2001.

[34] J. Luo. Material removal regions in chemical mechanical planarization for submicron integrated circuit fabrication: Coupling effects of slurry chemicals, abrasive size distribution, and wafer-pad contact area. *IEEE Trans. on Semiconductor Manufacturing*, 16(1):45–56, 2003.

[35] J. Luo. Effects of abrasive size distribution in chemical mechanical planarization: Modeling and verification. *IEEE Trans. on Semiconductor Manufacturing*, 16(3):469–476, 2003.

[36] Y. Zhao and L. Chang. A micro-contact and wear model for chemical-mechanical polishing of silicon wafers. *Wear*, 252:220–226, 2002.

[37] C.M. Zettner and M. Yoda. Direct visualization of particle dynamics in model cmp geometries. *Mat. R. Soc. Symp. Proc.*, 671:M6.6.1–M6.6.6, 2001.

[38] W. Choi, S.M. Lee, and R.K. Singh. Effects of particle concentration in cmp. *Mat. R. Soc. Symp. Proc.*, 671:M5.1.1–M5.1.6, 2001.

[39] K. Achuthan, J. Curry, M. Lacy, D. Campbell, and S.V. Babu. Investigation of pad deformation and conditioning during the cmp of silicon dioxide films. *Journal of Electronic Materials*, 25(10):1628–1632, 1996.

[40] W. Li, D.W. Shin, M. Tomozawa, and S.P. Murarka. The effect of the polishing pad treatments on the chemical-mechanical polishing of sio2 films. *Thin Solid Films*, 270:601–606, 1995.

[41] Y. Xie and B. Bhushan. Effects of particle size, polishing pad and contact pressure in free abrasive polishing. *Wear*, 200:281–295, 1996.

[42] D.R. Evans and M.R. Oliver. Rotational averaging of material removal during cmp. In *Mat. R. Soc. Symp. Proc.*, volume 671, pages M1.4.1–M1.4.7, 2001.

[43] Y. Moon, I. Park, and D.A. Dornfeld. Mechanical properties and relationship to process performance of the polishing pad in chemical mechanical polishing (cmp) of silicon. In *ASPE 1998 Spring Topical Meeting on Silicon Machining*, volume 17, pages 78–82, Monterey, CA, 1998. American Society for Precision Engineering.

[44] Y. Moon and D.A. Dornfeld. Investigation of the relationship between preston's coefficient and friction coefficient in chemical mechanical polishing (cmp) of silicon. In *ASPE 1998 Spring Topical Meeting on Silicon Machining*, volume 17, pages 83–87, Monterey, CA, 1998. American Society for Precision Engineering.

[45] T.K. Yu, C.C. Yu, and M. Orlowski. Statistical polishing pad model for chemical-mechanical polishing. *Technical Digest - International Electron Devices Meeting*, pages 865–868, 1993.

[46] B. Zhao and F.G. Shi. Modeling of chemical-mechanical polishing with soft pads. *Applied Physics A*, 67:249–252, 1998.

[47] J. Coppeta, C. Rogers, A. Philipossian, and F. Kaufman. Technique for measuring slurry-flow dynamics during chemical-mechanical polishing. In *Materials Research Society Symposium 1996 Fall Meeting*, volume 447, pages 95–100, Boston, MA, 1996.

[48] J. Coppeta, C. Rogers, L. Racz, A. Philipossian, and F. Kaufman. Investigating slurry transport beneath a wafer during chemical mechanical polishing processes. *Journal of the Electrochemical Society*, 147(5):1903–1909, 2000.

[49] J.L. Levert, A. Baker, F. Mess, S. Danyluk, R. Salant, and L. Cook. Mechanisms of chemical-mechanical polishing of sio2 dielectric on integrated circuits. *Tribol. Trans.*, 41(4):593–599, 1998.

[50] J. Levert, S. Danyluk, and J. Tichy. Mechanism for subambient interfacial pressures while polishing with liquids. *ASME J. of Tribol.*, 122(2):450–457, 2000.

[51] J.L. Levert. *Interface Mechanics of Chemical Mechanical Polishing for Integrated-Circuit Planarization*. PhD thesis, Georgia Institute of Technology, 1997.

[52] J. Tichy, J.A. Levert, L. Shan, and S. Danyluk. Contact mechanics and lubrication hydrodynamics of chemical mechanical polishing. *J. Electrochem. Soc.*, 146(4):1523–1528, 1999.

[53] B. J. Hamrock. *Fundamentals of Fluid Film Lubrication*. McGraw-Hill, 1994.

[54] F. Mess, J. Levert, and S. Danyluk. Vertical differential displacements at a pad/sapphire interface during polishing. *Wear*, 211:311–315, 1997.

[55] L. Shan, J.L. Levert, and S. Danyluk. Pressure distribution at the silicon/polishing pad interface. In *Proc. ASPE Spring Topical Meeting on Silicon Machining*, pages 96–100, 1998.

[56] L. Shan, J.L. Levert, L. Meade, J.A. Tichy, and S. Danyluk. Interfacial fluid mechanics and pressure prediction in chemical mechanical polishing. *ASME J. of Tribol.*, 122(3):539–543, 2000.

[57] L. Shan, C. Zhou, and S. Danyluk. Mechanical interactions and their effects on chemical mechanical polishing. *IEEE Trans. on Semiconductor Manufacturing*, 14(3):207–213, 2001.

[58] C. Zhou, S. H. Ng, L. Shan, J.R. Hight, A.J. Paszkowski, and S. Danyluk. Effects of nano-scale colloidal abrasive particle size on sio2 by chemical mechanical polishing. In *Mat. R. Soc. Symp. Proc.*, volume 671, pages M1.6.1–M1.6.7, San Francisco, CA, 2001. Material Research Society.

[59] C. Zhou, L. Shan, J.R. Hight, S. H. Ng, and S. Danyluk. Fluid pressure and its effects on chemical mechanical polishing. *Wear*, 253:430–437, 2002.

[60] C. Zhou, L. Shan, J.R. Hight, and S. Danyluk. Influence of colloidal abrasive size on material removal rate and surface finish in sio2 chemical mechanical polishing. *Tribol. Trans.*, 45(2):232–238, 2002.

[61] L. Shan. *Mechanical Interactions at the Interface of Chemical Mechanical Polishing*. PhD thesis, Georgia Institute of Technology, 2000.

[62] A.T. Kim, J. Seok, C. Sukam, J.A. Tichy, and T.S. Cale. A multiscale model for chemical mechanical planarization. In *Advanced Metallization Conference*, pages 405–409, 2001.

[63] J. Seok, C.P. Sukam, A.T. Kim, J.A. Tichy, and T.S. Cale. Multiscale material removal modeling of chemical mechanical polishing. *Wear*, 254:307–320, 2003.

[64] R.S. Rivlin. *Rheology*, volume I. Academic Press, New York, 1956.

[65] R.W. Ogden. Large deformation isotropic elasticity - on the correlation of theory and experiment for incompressible rubberlike solids. *Proc. R. Soc. Lond. A*, 326:565–584, 1972.

[66] R.W. Ogden. Large deformation isotropic elasticity: on the correlation of theory and experiment for compressible rubberlike solids. *Proc. R. Soc. Lond. A*, 328:567–583, 1972.

[67] P.J. Blatz and W.L. Ko. Application of finite elastic theory to the deformation of rubbery materials. *Trans. Soc. Rheology*, VI:223–251, 1962.

[68] J.M. Gere. *Mechanics of Materials*. Brooks/Cole, Pacific Grove, CA, 2001.

[69] I.D. Vrinceanu. *Analysis of the Residual Stresses in Silicon Wafers Using Shadow Moire Technique*. Ph.d., Georgia Institute of Technology, 2002.

[70] S.P. Murarka and R.J. Gutmann. 1994 annual report of the new york state scoe. Technical report, Semiconductor Research Corporation, 1994.

[71] Y. Obeng, A. Dogariu, and K. Forsthoefel. Mechanical and chemical properties of pads for use in chemo-mechanical processing (cmp), from the internet http://www.creol.ucf.edu/people/faculty/kcr/cmp2.pdf.

[72] A.S. Lawing. The role of pad asperity structure and pad conditioning in cmp. In *8th Int'l Symp. on CMP*, Lake Placid, NY, 2003. Center for Advanced Materials Processing.

[73] L. Borucki, T. Witelski, C. Please, P Kramer, and D. Schwendeman. Theory of pad conditioning and wear. In *8th Int'l Symp. on CMP*, Lake Placid, NY, 2003. Center for Advanced Materials Processing.

[74] J. Peklenik. New developments in surface characterization and measurement by means of random process analysis. *Proc. Insts. Mech. Engrs.*, 182(3K):108, 1967.

[75] N. Chechik and D. James. Thermal analysis of polishing pad. In *8th International Symposium on Chemical-Mechanical Planarization*, Lake Placid, NY, 2003. Center for Advanced Materials Processing.

[76] H. Lu, Y. Obeng, and K.A. Richardson. Applicability of dynamic mechanical analysis for cmp polyurethane pad studies. *Materials Characterization*, 49:177–186, 2003.

[77] L.E. Meade. *Effective Elastic Modulus of Polyurethane Asperities*. PhD thesis, Georgia Institute of Technology, 2000.

[78] J.R. Hight. *Interfacial Fluid Pressure and Pad Viscoelasticity during Chemical Mechanical Polishing*. PhD thesis, Georgia Institute of Technology, 2002.

[79] N. Patir and H.S. Cheng. An average flow model for determining effects of three-dimensional roughness on partial hydrodynamic lubrication. *ASME J. Lubr. Technol.*, 100:12–17, 1978.

[80] N. Patir and H.S. Cheng. An average flow model for determining effects of three-dimensional roughness on partial hydrodynamic lubrication. *ASME J. Lubr. Technol.*, 101:12–17, 1979.

[81] R.A. Burthon. Effects of two-dimensional, sinusoidal roughness on the load support characteristics of a lubricant film. *ASME Journal of Basic Engineering*, 85:258–264, 1963.

[82] R.F. Salant. Numerical analysis of the flow field within lip seals containing microundulations. *ASME Journal of Tribology*, 114:485–492, 1992.

[83] S.T. Tzeng and E. Saibel. Surface roughness effect on slider bearing lubrication. *ASLE Transactions*, 10:334–338, 1967.

[84] H. Christensen. Stochastic models for hydrodynamic lubrication of rough surfaces. *Proceedings of the Institution of Mechanical Engineers*, 184(1):1013–1022, 1970.

[85] H. Christensen and K. Tonder. The hydrodynamic lubrication of rough bearing surfaces of finite width. *ASME Journal of Lubrication Technology*, 93:324–330, 1971.

[86] H. Christensen and K. Tonder. Waviness and roughness in hydrodynamic lubrication. *Proceedings of the Institution of Mechanical Engineers*, 186(72):807–812, 1972.

[87] H. Christensen. A theory of mixed lubrication. *Proceedings of the Institution of Mechanical Engineers*, 186(41):421–430, 1972.

[88] H.G. Elrod. A general theory for laminar lubrication with reynolds roughness. *ASME Journal of Lubrication Technology*, 101:8–14, 1979.

[89] J.H. Tripp. Surface roughness effects in hydrodynamic lubrication: the flow factor method. *ASME Journal of Lubrication Technology*, 105:458–465, 1983.

[90] J.A. Williams. *Engineering Tribology*. Oxford University Press Inc., New York, NY, 2000.

[91] N.J. Brown, P.C. Baker, and R.T. Maney. Contemporary methods of optical fabrication. *Proc. SPIE*, 306:42, 1981.

[92] H. Hocheng, H.Y. Tsai, and Y.T. Su. Modeling and experimental analysis of the material removal rate in the chemical mechanical planarization of dielectric films and bare silicon wafers. *Journal of the Electrochemical Society*, 148(10):581–586, 2001.

[93] Y. Zhao, L. Chang, and S.H. Kim. A mathematical model for chemical-mechanical polishing based on formation and removal of weakly bonded molecular species. *Wear*, 254:332–339, 2003.

[94] E. Rabinowicz. *Friction and Wear of Materials*. John Wiley and Sons, Inc., New York, NY, 2nd edition, 1995.

[95] M. Bielmann, U. Mahajan, and R.K. Singh. Effect of particle size during tungsten chemical mechanical polishing. *Electrochemical and Solid-State Letters*, 2(8):401–403, 1999.

VITA

Sum Huan Ng, son of Peng Phoi Ng and Kim Eng Yeo, was born in Singapore on January 22, 1972. He grew up and received his primary, secondary and junior college education there. He attended the National University of Singapore from 1993 to 1999, where he earned his Bachelor of Engineering (1997) and Master of Engineering (2000), both in Mechanical Engineering. His master's thesis was on the evaluation and development of a miniature contact pressure measurement sensor based on the piezoresistive property of the aluminum gallium arsenide semiconductor. In August of 1999, he joined Gintic Institute of Manufacturing Technology (now known as Singapore Institute of Manufacturing Technology), a national research and development institute of Singapore. He worked on electrodischarge machining, electrochemical machining and chemical mechanical polishing during his stay there. He received a scholarship from the institute to further his studies. He was admitted into the George W. Woodruff School of Mechanical Engineering at Georgia Institute of Technology in May 2001 to pursue a doctoral degree. At Georgia Institute of Technology, he conducted research in chemical mechanical polishing, under the guidance of Professor Steven Danyluk.